**UNIVERSITÀ DI PISA**

**Scuola di Dottorato in Ingegneria "Leonardo da Vinci"**

**Corso di Dottorato di Ricerca in
INGEGNERIA MECCANICA**

**Tesi di Dottorato di Ricerca**

# LASER BEAM WELDING OF STAINLESS STEELS

*Ing. Mohammad Muhshin Aziz Khan*

*Anno 2012*

**Università di Pisa**

Corso di Dottorato di Ricerca in
**Ingegneria Meccanica**

# Laser Beam Welding of Stainless Steels

*Tesi svolta per il conseguimento del titolo di dottore di ricerca*

Settore Scientifico Disciplinare: ING-IND/16 .

**Allievo:**

Ing. Mohammad Muhshin Aziz Khan

**Relatori:**

| | |
|---|---|
| Prof. Gino Dini | (DIMNP, Pisa) |
| Prof. Marco Beghini | (DIMNP, Pisa) |
| Ing. Marco Fiaschi | (Continental Automotive Italy SpA) |

**X Ciclo**

**Anno 2012**

**UNIVERSITÀ DI PISA**

**Scuola di Dottorato in Ingegneria "Leonardo da Vinci"**

**Corso di Dottorato di Ricerca in
Ingegneria Meccanica**

**Tesi di Dottorato di Ricerca**

# Laser Beam Welding of Stainless Steels

*Allievo:*

*Mohammad Muhshin Aziz Khan* _____

*Relatori:*

*Prof. Gino Dini* _____

*Prof. Marco Beghini* _____

*Ing. Marco Fiaschi* _____

*Anno 2012*

# ABSTRACT

The main objective of this research is to study the laser beam welding of stainless steels. During experimentation, a 1.1kW CW Nd:YAG laser is used to weld as-received similar martensitic and dissimilar austenitic/ferritic stainless steels in overlap and fillet joint configurations respectively. The influence of various operating parameters such as laser power, welding speed, fiber diameter, angle of incidence, and the defocus distance, and their interactions on the weld bead geometry and mechanical properties are examined. Effects of energy density and line energy, two key process parameters from energy perspective, on the weld bead characteristics are also investigated to understand certain energy dependent welding phenomena, and to show their consequent impact on the aforesaid factors. Moreover, formation of solidification microstructures and the distribution pattern of the segregated alloying elements in the weld with varied energy input are studied and correlated with the corresponding change in local microhardness.

In order to predict and optimize the laser welding of these economically important and technologically critical stainless steels in automotive industry, full factorial design (FFD) and response surface methodology (RSM) are respectively used as a design of experiment (DOE) approach to design the experiments, develop the mathematical models, and optimize the welding operation. In these studies, for each welded material, mathematical models are developed to predict the required responses. Furthermore, the developed models are optimized by determining the best combinations of input process parameters to produce an excellent weld quality.

Finally, considering the experiment-based evidences i.e. weld resistance length is energy-limited and weld penetration depth is the characteristic factor determining the resistance length, a simplified energy-based model is developed for laser welding of ferritic stainless steels in overlap joint configuration. The developed model is quite accurate in predicting the weld penetration depth directly from the welding input parameters provided that welding is conduction-limited.

## SOMMARIO

Obiettivo principale di questa tesi di dottorato è quello di studiare la saldatura laser degli acciai inossidabili. Durante gli esperimenti un laser Nd-YAG in onda continua da 1.1kW è stato utilizzato per saldare rispettivamente acciai martensitici in configurazione di piena penetrazione e combinazioni di acciai austenitici/ferritici in configurazione d'angolo. È stata studiata l'influenza di vari parametri di processo come potenza del laser, velocità di saldatura, diametro della fibra, angolo di incidenza e defocalizzazione nonché le loro interazioni sulla geometria del giunto e sulle sue proprietà meccaniche. Si sono analizzati, inoltre, gli effetti della densità di energia e dell'energia per unità di lunghezza sulle caratteristiche del giunto di saldatura in modo da evidenziare la dipendenza del processo dai fenomeni di scambio termico. Successivamente si è studiato la microstruttura della solidificazione del giunto e la relativa distribuzione degli elementi di lega per diversi valori della densità di energia correlandole con la variazione locale della microdurezza.

Durante il corso della ricerca, sono state utiliizzate tecniche di DOE come il FFD ed il RSM con l'obiettivo di modellare ed ottimizzare il processo di saldatura laser. In questa fase, per ogni materiale saldato sono stati elaborati dei modelli in grado di determinare i fattori chiave che governano il processo. Tali modelli, inoltre, sono stati ottimizzati prendendo in considerazione la combinazione dei parametri di processo che consente di avere giunti di qualità superiore in termin di geometria e caratteristiche meccaniche.

È stato, infine, elaborato un modello teorico per la determinazione della geometria di un giunto ottenibile dalla saldatura in piena penetrazione di acciai ferritici. Tale modello si basa sul concetto che la geometria risultante è funzione del tipo di scambio termico che si genera durante il processo e che a sua volta tale scmbio termico vari in funzione della densità di energia fornita dla laser. Il modello ha dimostrato una corrispondenza con i dati sperimentali con una maggior accuratezza nel caso di saldatura per conduzione.

## ACKNOWLEDGMENTS

**INDEX**

## NOMENCLATURE

| | | |
|---|---|---|
| **P** | Laser power | [W] |
| **S or $v$** | Welding speed | [m/min] |
| **F** | Optical fiber diameter | [µm] |
| $\boldsymbol{\Phi_{spot}}$ | Focal spot diamter | [µm] |
| **A** | Angle of incidence | [deg] |
| **D** | Defocus distance | [mm] |
| **$ED$** | Energy density | [J/mm$^2$] |
| **$ED_{th}$** | Threshold energy density | [J/mm$^2$] |
| **$LE$** | Line energy | [kJ/m] |
| **W** | Weld width | [mm] |
| **$D_p$** | Weld penetration depth | [mm] |
| **$S_L$** | Weld resistance length | [mm] |
| **$P_r$** | Weld radial penetration | [mm] |
| **$F_s$** | Weld shearing force | [N] |
| **m** | Mass of the welded material | [kg] |
| **$Q_{ab}$** | Absorbed energy | [J] |
| **$Q_{th}$** | Threshold energy | [J] |
| **$K$** | Reciprocal of specific energy | [kg/J] |
| **$T_{amb}$** | Ambient temperature | [K] |
| **$T_m$** | Melting temperature | [K] |
| **$T_{max}$** | Maximum temperature | [K] |
| **$C_{ps}$** | Specific heat in solid state | [J/kg.K] |
| **$H_m$** | Latent heat at melting point | [J/kg] |
| **$C_{pl}$** | Specific heat at liquid state | [J/kg.K] |
| **$P_A$** | Fraction of absorbed power | [W] |
| **$A_c$** | Absorption coefficient | |
| **$P_{in}$** | Incident laser power | [W] |
| **Δt** | Irradiation time | [min] |
| **$L$** | Extension of irradiated area along welding direction | [m] |

# CHAPTER 1

INTRODUCTION

## 1.1 PREFACE

Welding is a process of joining the surfaces of two work-pieces (usually metals) through localized coalescence. It is a precise, reliable, cost-effective, and high-tech method for joining materials. No other technique is as widely used by manufacturers to join metals and alloys efficiently and to add value to their products. Most of the familiar objects in modern society, from buildings and bridges, to vehicles, computers, and medical devices, could not be produced without the use of welding.

Nowadays, welding goes well beyond the bounds of its simple description. This technique is applied to a wide variety of materials and products, using advanced technologies, such as lasers and plasma arcs. The future of welding holds even greater promise as methods are devised for joining dissimilar and non-metallic materials, and for creating products of innovative shapes and designs.

This chapter tries to clarify the various background issues concerning the laser beam welding of stainless steels.

## 1.2 LASER BEAM WELDING

Laser welding is a fusion joining process that produces coalescence of materials with the heat obtained from a concentrated beam of coherent, monochromatic light impinging on the joint to be welded and hence, belongs to the group of liquid-phase joining. The necessary energy is obtained from a focused laser beam which locally creates a melt pool that is moved along a joint resulting in a weld seam. These laser weld seams are typically narrower than can be produced by conventional welding techniques. The capability of laser welding to produce precise, repeatable joints at high process speeds offers a unique alternative to TIG welding, electron beam welding (EBW) and resistance welding.

The focused laser beam is one of the highest power density sources available to industry today. It is similar in power density to an electron beam as shown in the Fig. 1.1. Together these two processes represent part of the new technology of high energy density processing. However, vacuum and x-ray shielding are not required in LBW as laser can travel through air or vacuum with minimal loss of energy. These technological aspects provide competitive advantages to LBW over the EB welding from operation and cost standpoints. Moreover, unlike EBW, a wide range of dissimilar materials can be laser welded.
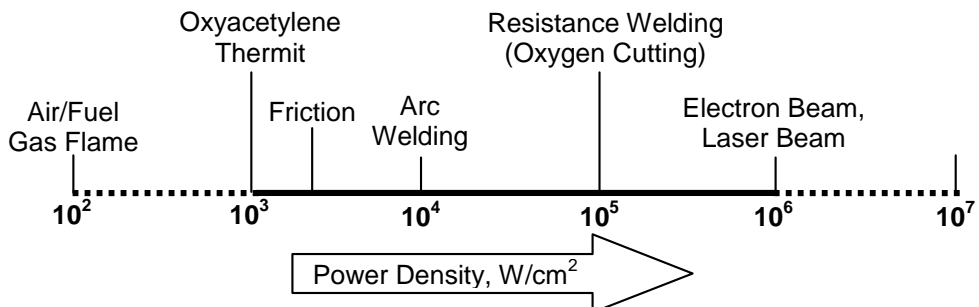


Fig. 1.1: Relative power densities of different heat sources [1]

Because laser welding is a high-energy density process, the material exposed to a sharply focused laser beam can melt or even vaporize to form a deep keyhole instantaneously, and welding is completed before much heat is conducted away into the bulk of the workpiece. The laser welding, therefore, results in better weld quality, deeper penetration depth, and less damage or distortion to the welded part as indicated in Fig. 1.2. Moreover, this low heat input to the welded joint has beneficial metallurgical consequences.
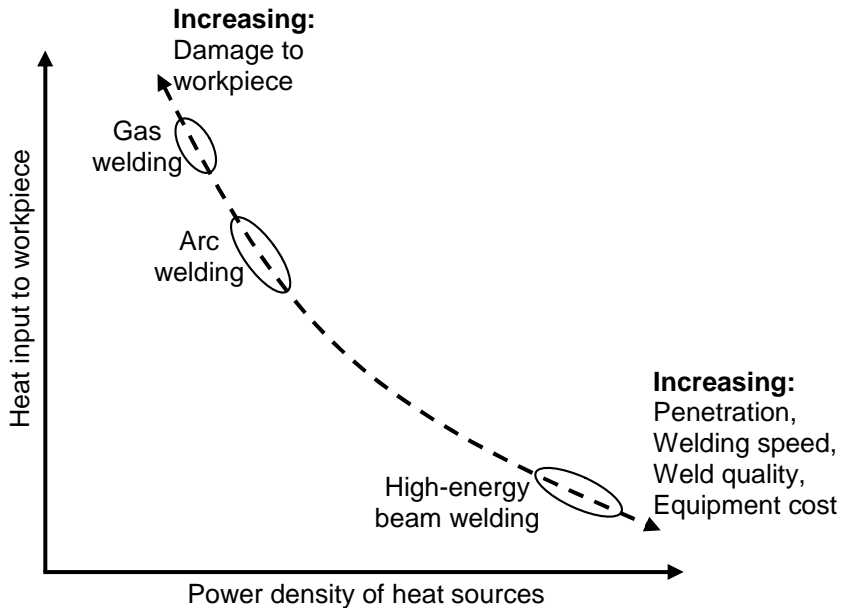


Fig. 1.2: Variation in heat input with the power density of heat source [2]

The main characteristics of the laser beam welding are listed in Table 1.1. From the aforesaid table, it can be seen that the laser has something special to offer as a high-speed, high-quality welding tool. It also has advantages in areas requiring the welding of heat-sensitive components such as heart pacemakers, pistons assembled with washers in place, valve seat rest on a thin lower screen, and thin diaphragms on larger frames.

Table 1.1: Main characteristics of the laser beam welding [3]

|   | Characteristics | Comments |
|---|---|---|
| 1 | High energy density | Less distortion |
| 2 | High processing speed | Cost-effective (if fully employed) |
| 3 | Rapid start/stop | Unlike arc processes |
| 4 | Welds at atmospheric pressure | Unlike electron beam welding |
| 5 | No X-rays generated | Unlike electron beam welding |
| 6 | No filler required (Autogenous weld) | No flux cleaning |
| 7 | Narrow weld | Less distortion |
| 8 | Relatively little HAZ | Can weld near heat-sensitive materials |

| 9 | Very accurate welding possible | Can weld thin to thick material |
|---|---|---|
| 10 | Good weld bead profile | No clean up necessary |
| 11 | No beam wander in magnetic field | Unlike electron beam welding |
| 12 | Little or no contamination | Depends only on gas shrouding |
| 13 | Relatively little evaporation loss of volatile components | Advantages with Mg and Li alloys |
| 14 | Difficult materials can sometimes be welded | General advantage |
| 15 | Relatively easy to automate | General feature of laser processing |
| 16 | Laser can be time-shared | General feature of laser processing |

### 1.2.1 Laser material interaction

An important mechanism in laser beam welding is the interaction of the laser beam with the material. This interaction mechanism is influenced by many parameters, such as the laser power, the intensity distribution of this power at the surface, the welding speed, the material properties, the protection gas supply and the wavelength of the laser radiation. The latter is constant in this thesis, since only a Nd:YAG ($\lambda$ =1.06 µm) laser is considered. As illustrated in the Fig. 1.3 (a)-(b), there are two modes of welding with the laser: conduction welding and keyhole or deep penetration welding. Each mode is characterized by different laser material interaction phenomena [4-5].
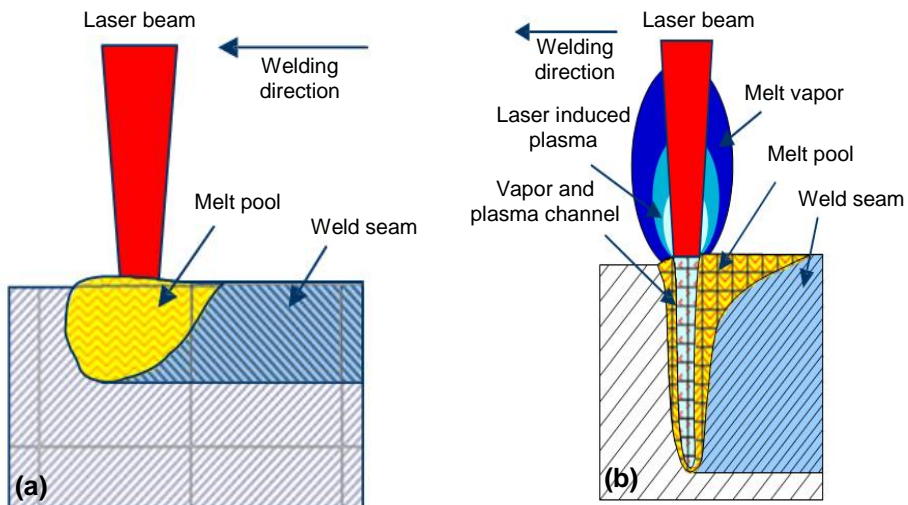


Fig. 1.3: Modes of welding with laser: (a) conduction and (b) keyhole welding

### 1.2.1.1 Conduction mode welding

This type of welding occurs at relatively low laser beam intensity ($I < 10^{10}$ W/m$^2$). The laser energy is absorbed by Fresnel absorption at the surface of the workpiece and can be described by an absorption coefficient A, indicating the fraction of absorbed laser power $P_A = A \cdot P$. For steel at the melting temperature ($T_m$ = 1800

K) the absorption coefficient is of the order of A = 0.4 for Nd:YAG laser radiation. The rest of the laser energy is reflected. For metal the laser energy is absorbed in a thin layer (~ 40 nm) at the surface of the workpiece where it is converted into heat. The absorbed energy is transported into the depths of the material solely through heat conduction, and the size of the weld pool is limited by the conduction of the heat away from the point that the beam impinges on the workpiece surface as shown in 1.4. For this reason, the weld depth ranges from only a few tenths of a millimeter to 1 millimeter. The heat conductivity of the material limits the maximum weld depth. If the heat is not able to dissipate quickly enough, the processing temperature rises above the vaporization temperature. Metal vapor forms, the welding depth increases sharply, and the process turn into deep penetration welding. In conduction welding, the laser produces a smooth, rounded seam that does not require any extra grinding or finishing. Pulsed or continuous-wave solid-state lasers are employed in such application.
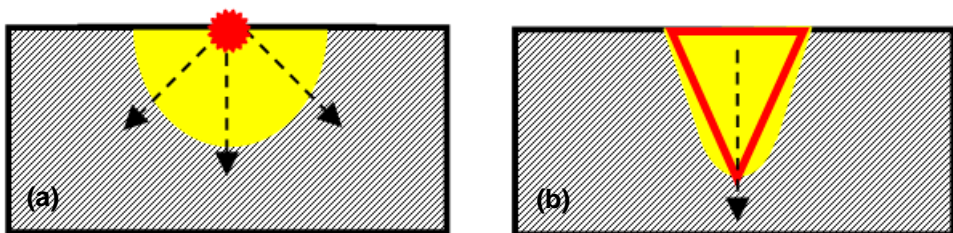


Fig 1.4: Energy coupling into the material through (a) isotropic and (b) preferential z conduction depending on energy density input.
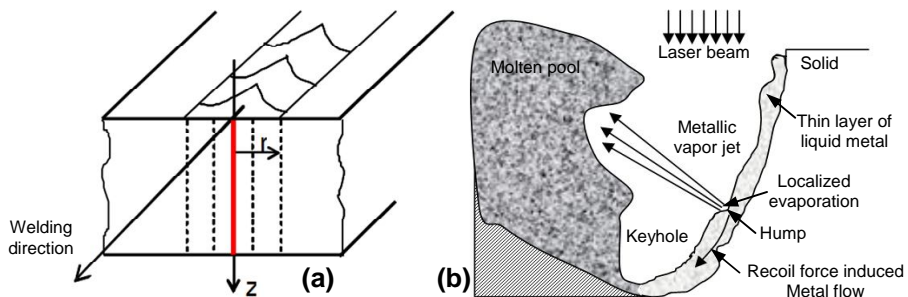


Fig. 1.5: (a) Energy coupling into the material, and (b) keyhole shape and energy absorption during keyhole welding [6].

## 1.2.1.2 Keyhole mode welding

As the intensity of the laser beam is increased (I ≥ $10^{10}$ W/m$^2$), the molten metal in the focus of the laser beam starts to evaporate. The recoil pressure of the vapor pushes the melt aside, creating a capillary filled with hot metal gas or plasma. This capillary is known as the keyhole and can extend over the complete depth of the workpiece. The hot gas escaping from the keyhole forms plasma or plume above the workpiece as can be seen in Fig. 1.3(b). The laser beam energy is absorbed on the walls of the keyhole. The laser beam is exposed to the keyhole wall repeatedly due to the reflections down the keyhole as shown in Fig. 1.5 (b). At every reflection a fraction of the laser energy is absorbed. Because of this multiple reflections

mechanism, keyhole mode welding has a high total absorption (> 80%). Furthermore, the gas inside and above the keyhole absorbs laser radiation by inverse Bremsstrahlung. For Nd:YAG laser radiation this absorption mechanism is very weak compared with the Fresnel absorption at the keyhole walls [7-8]. Due to the keyhole the energy is absorbed throughout the whole depth of the workpiece. This allows for high welding speeds in keyhole or deep penetration welding and results in welds with a high depth to width ratio and a small heat affected zone (HAZ).

## 1.2.2 Selection of laser welding

Laser welding, nowadays, is increasingly being used in industrial production ranging from microelectronics to shipbuilding. Automotive manufacturing, however, is among the industrial sectors which have proven to be most outstanding at developing applications that take advantage of the many benefits of this technology [9]:

- Low heat input;
- Small heat affected zone (HAZ);
- Low distortion rate; and
- High welding speed.

These characteristics have made laser welding the process of choice for many applications that used conventional welding in the past. By adding the benefits of single-sided access, laser welding is given another strategic advantage, allowing it to open the door for a multitude of new applications.

Modern CNC multi-axis laser welding workstations can provide precise and repeatable welding. A successful laser weld, however, requires a combination of appropriate weld joint design, motion control, fixture design, metallurgy, production control, and quality systems.

All three of the most common joint configurations can be used: lap, butt, or fillet, but intimate contact between the materials at the joint is preferred. Under these conditions, high quality, low porosity, and controlled grain size welds with consistent weld depth and width can be achieved [10].

Weldable materials range from normal and high-strength constructional steels through to high-alloyed stainless steels. Titanium, aluminum, and nickel base materials can also be problem-free welded. Besides, high heating and cooling rates produce fine microstructures, which improve mechanical properties of the weld. Since the heat source is the energy of light, the workpiece is welded purely resulting in excellent fatigue strength of the welded joint as well.

The laser welds can be cost competitive based on minimum set-up time, low fixturing costs, high feed rates, and high-energy efficiency. Resultant welds generally have minimum part distortion with reduced rectification and decreased post-weld costs.

### 1.2.3 Selection of Nd:YAG laser as heat source

About 11 percent of industrial solid-state and $CO_2$ lasers are integrated into welding systems that are used in industries ranging from the manufacture of dental/surgical instruments on a micro scale to the macro scale, on-line assembly of automotive body-in-white. In between are a wide variety of industries, all with unique joining requirement, that make up general field of laser welding. And this diverse market, heavily product and metallurgy oriented, is one reason that laser welding has historically made up only 10-15 percent of the total laser market.

Nowadays, the multi-kilowatt laser application and processing market is dominated by $CO_2$ and Nd:YAG lasers, which combine to a total of more than 90% of all installed laser systems. Since the late 1980's when more than 80% of all installed multi-kilowatt lasers were $CO_2$ lasers. The Nd:YAG lasers have constantly grown their market share, which is now more than 50% [11]. Today with both systems being equally reliable, the focus shifts to the end user to pick the right system to address all of their customer requirements in respect to part quality and manufacturing cost. Recent breakthroughs in the field of laser diodes and fiber lasers present new opportunities for solving manufacturing tasks. However, these require thorough application-focused investigations in order to convert them into reliable manufacturing processes.

The main differences between Nd:YAG and $CO_2$ laser sources are beam quality, brightness, and wavelength [12]. Beam quality refers to the focusabiltiy of the laser, and brightness refers to the power density contained within the focused beam. Because the Nd:YAG laser is 1/10th the wavelength of the $CO_2$ laser, it can be focused to a spot size that is ten times smaller, and hence, the Nd:YAG laser has higher beam quality and brightness.

In laser welding, deep penetration and high speeds are directly related to high beam quality and brightness. However, weldability and tolerance accommodation tend to favor lesser beam quality and brightness. A balance, therefore, needs to be found between the welding performance and the quality of weld and size of the process window. It should be noted that there is always room to reduce the quality of the beam to match the application, but it is not possible to make a poor quality beam better.

This difference in wavelengths has also process and integration implications. The main process effect is that $CO_2$ laser creates a stronger welding plume above the weld, which diffuses the beam power density, reducing penetration and enlarging the weld width at the surface. However, during high-power Nd:YAG laser welding, the effect of plasma formation is only of secondary importance [12]. This is due to the shorter wavelength of Nd:YAG laser radiation, which is absorbed less in the plasma cloud compared to $CO_2$ laser radiation, and the lower beam intensity.

Regarding integration, at 10.6 µm, the $CO_2$ laser must be directed from the laser to the focus head by mirrors. These can be orthogonal mirrors on a gantry type system or through articulated arms to enable 6-axis motion, but the alignment through the system must be maintained as must the mirror integrity. Besides, exiting the $CO_2$ laser the beam is not perfectly collimated i.e. it expands and/or contracts slightly while in the pipe system. If the weld head is moved during the

welding process, the beam diameter on the focusing lens varies and this affects the spot size on the workpiece. As a result, the weld bead dimension and part quality will be notably different when longer parts are welded or a gantry style system is used with multiple workstations. The Nd:YAG laser, on the other hand, can be delivered by flexible fiber optic cable thus providing plug-and-play beam delivery [12]. The length of the fiber can be anywhere from 5m to 200m, which allows the laser to be positioned anywhere around the work cell and offers the option of remote laser location if needed.

### 1.2.3.1 Shielding gases for Nd:YAG laser welding

Laser beam absorption and scattering due to plasma formation is of secondary importance in Nd:YAG laser welding in contrast to $CO_2$ laser welding. As a result, helium and helium mixtures are not particularly useful as shielding gases in Nd:YAG laser welding of stainless steels.

The selection of shielding gases for Nd:YAG laser welding of stainless steels is largely determined by the need to provide protection against oxidation. Argon has been used as a welding gas for low-power Nd:YAG laser welding (less than 1000 W) of small stainless steel components for many years. Argon may also be applied in high-power welding (1–5 kW) [13]. When welding austenitic steels, argon/6–10% hydrogen may be used to reduce surface oxides in order to obtain shiny weld surfaces. The selection of argon as shielding gas in turn reduces the production cost.

### 1.3 SELECTION OF STAINLESS STEELS

Stainless steels constitute a group of high-alloy steels based on Fe-Cr, Fe-Cr-C, and Fe-Cr-Ni systems. To be stainless, these steels must contain a minimum of 10.5 wt% chromium. This level of chromium allows formation of a passive surface oxide that prevents oxidation and corrosion of the underlying metal under ambient, noncorrosive conditions. Also, these steels have good resistance to oxidation, even at high temperatures, and they are often referred to as high-resisting alloys. Resistance to elevated temperature oxidation is primarily a function of chromium content, and some high chromium alloys (25 to 30 wt%) can be used at temperatures as high as 1000 °C. Another form of heat resistance is resistance to carburization, for which stainless steel alloys of modest chromium content (about 16 wt%) but high nickel content (about 35 wt%) have been developed.

Corrosive media that attack and remove the passive oxide cause corrosion of stainless steels. Corrosion can take many forms, including pitting, crevice corrosion, and intergranular attack. These forms of corrosion are influenced by the corrosive environment, the metallurgical condition of the material, and the local stresses that are present. Austenitic steels are more or less resistant to general corrosion, crevice corrosion and pitting, depending on the quantity of alloying elements. Resistance to pitting and crevice corrosion is very important if the steel is to be used in chloride-containing environments. Resistance to pitting and crevice corrosion increases with increasing contents of chromium, molybdenum and nitrogen. Modern molybdenum-alloyed ferritic steels have largely the same corrosion resistance as AISI 316 but are superior to most austenitic steels in terms of their resistance to stress corrosion cracking. In general, corrosion resistance of

the martensitic stainless steels is not as good as that of the other grades, due to the relatively low chromium content and high carbon content (compared to more corrosion resistant stainless steels). Owing to their high strength in combination with some corrosion resistance, martensitic steels are suitable for applications which subject to both corrosion and wear. Engineers and designers must be very aware of the service environments and impact of fabrication practice on metallurgical behavior when selecting stainless steels for use in corrosive conditions.

Traditionally, stainless steels are categorized based on the metallurgical phase (or phases), which is predominant. The three phases possible in stainless steels are martensite, ferrite, and austenite. Duplex stainless steels contain approximately 50% austenite and 50% ferrite, taking advantage of the desirable properties of each phase. Precipitation hardenable (PH) grades are termed such because they form strengthening precipitates and are hardenable by an aging heat treatment. PH stainless steels are further grouped by the phase or matrix in which the precipitates are formed: martensitic, semi-austenitic, or austenitic types. However, in this thesis, experimental investigation will be focused on the three basic categories of stainless steels. The area of use for these stainless steels is very vast and comprises mainly applications taking advantage of properties such as resistance against corrosion and/or very high or low temperatures, hygienic surfaces, and aesthetic appearance. Increasingly, stainless steels are being used also for their mechanical properties such as the combination of very high strength and excellent formability together with high energy absorption capability in finished components [14].

### 1.3.1 Metallurgical aspects of laser welding

Laser welding is a process where the workpiece material experience heating, melting, and solidification and forms the fusion zone with modified grain structure. Solidification is a very complex procedure, as it depends on the material compositions, solidification modes (planer, cellular, or dendritic), cooling rate, etc. It is the grain structure developed in the fusion zone that has the most influence to the quality and performance of the laser welded parts, and usually the formation of fine equiaxed grains in the fusion zone are favorable since the fine grains can help reduce the susceptibility of the weld metal to solidification cracking during welding, and also fine grains can improve the mechanical properties of the weld, such as the ductility and fracture toughness.

Fusion area can be considered as mini-casting region [15]. Therefore, parameters important in determining microstructures in casting, such as growth rate, temperature gradient, under cooling, and alloy composition determine the development of microstructures in welds as well. But unlike in casting, during welding, where the molten pool is moved through the material, the growth rate and temperature gradient vary considerably across the weld pool. In welds, weld pool solidification often occurs without a nucleation barrier. Therefore, no significant under-cooling of the liquid is required for nucleation of the solid. Solidification occurs instinctively by epitaxial growth (the growth of one layer of crystals on another such that they have the same structure) on the partially melted grains during autogenous welding.

Much effort has been made to try for the refined grain of the weld fusion zone. Almost all laser-welding is performed on metal, and all the rules of metallurgy continue to apply on laser-welding. The metallurgical differences between laser beam welding and conventional processes are related to the small size and high intensity of the focused laser beam as a heat source. The fusion zone is small, and the part is heated (and cool down) rapidly. This is generally an advantage, as problems such as grain growth in high strength low alloy steels or the sensitization of austenitic stainless steels do not have time to appear. In addition, the relatively small volume of the fusion zone in comparison to conventional welding reduces the stresses associated with solidification shrinkage. Rapid solidification rates, however, can produce atypical microstructures and constituents in many common alloys [16].

## 1.4 QUALITY ISSUES FOR LASER WELDING

Defining and measuring the weld quality continue to be major issues for many manufacturing companies utilizing laser beam welding. In these contexts, ISO 13919-1:1996 standard specifying the level of laser weld quality suitable for process control or level of imperfection allowed for a particular application is used as a reference. However, the necessary weld quality should be defined by the application standard or the responsible designer in conjunction with the manufacturer, user and/or other parties concerned. In this thesis, weld quality definition includes the design requirements for the weld bead geometry and mechanical properties, and the acceptance level of weld imperfections.

### 1.4.1 Weld bead geometry

The weld width, penetration depth, radial penetration, and resistance length etc. are the weld bead characteristic lengths that determine the weld cross section and, with it, the strength (shearing force) of the weld joint. For this reason, attaining the proper weld characteristic lengths is crucial. For a particular application, the design criteria (mechanical requirements, dimension and tolerance, surface finish etc.) of welded joint are specified basing on ISO 15614-11:2002 and RT 1040 standards. The geometric parameters of the fabricated weld must meet these design requirements and remain constant along the entire seam in order to obtain the desired performance from the weld joint in service.

### 1.4.2 Weld defects

Weld defects are of two types: external and internal weld defects. Below is a list of external weld defects and their effects [17]:

- Shape imperfections such as undercutting produce weak points where cracking can occur.
- Expelled molten material: holes form if molten material is expelled from the seam. The holes reduce strength and make the weld porous.
- Bead sagging or root concavity reduces the weld cross section and, thus, the weld strength.
- Misalignment of the parts in a butt joint also reduces the weld cross section.
- Craters at the end of the weld reduce the weld cross section as well. They result if the laser beam is switched off too quickly.

- Spatter on the workpiece or on the surface of the weld can cause assembly problems and may require reworking.
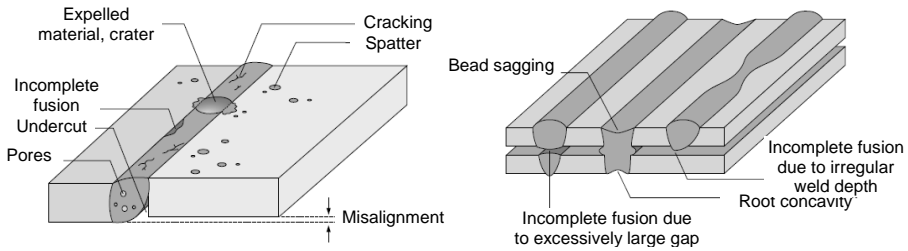


Fig. 1.6: External and internal weld defects that can occur in laser welding of (a) a butt joint and (b) a lap joint.

Quality defects in the material and incorrectly set process parameters can cause the following problems:

- Incomplete fusion: the joint gap is incompletely filled.
- Porosity: small air or gas bubbles are trapped in the weld.
- Cracks in the weld surface or in the workpiece: causes can include stresses or material shrinkage during cooling.

From the viewpoints of design considerations; subsequent processing (e.g. surfacing); mode of stressing (e.g. static, dynamic); service conditions (e.g. temperature, environment); and consequence of failure, stringent quality level defined by ISO 13919-1:1996 standard has been used in this thesis as reference data for controlling the welding process; ensuring the dimensional requirements for the weld geometry; and limiting weld defects [18]. Table 1.2 shows the defects that occur during welding and their limits used for weld quality assurance. However, only those, which are relevant to the particular weld joint design, are considered for process and quality control.

Table 1.2: Weld defects and their limits used for weld quality assurance

| Imperfection, designation | Limits for imperfection |
|---|---|
| Cracks | Not permitted |
| Shrinkage cavity and crater pipe | Not permitted |
| Lack of fusion | Not permitted |
| Incomplete penetration | Not permitted |
| Weld spatter | D < 0.1mm and d < 1 mm |
| Excess weld metal | h < 0.2 mm |

ISO 15614-11:2002 standard also provides the conditions for welding procedure qualification test in accordance with the specified acceptance level. Qualification of welding procedure serves to demonstrate that production operations fully comply with the agreed welding procedure including preliminary and subsequent treatment. In this thesis, the examination and testing including the non-destructive examination (NDE) and destructive testing are conducted in accordance with the requirements of Table 1.3.

Table 1.3: Examination and tests for welds

| Type of weld joint | Type of examination and test | Extent of examination and test |
|---|---|---|
| Lap Joint and Fillet Joint | Visual examination | 100% |
| | Surface crack detection | 100% |
| | Mechanical characterization | 100% |
| | Metallographic examination | 1 sections (minimum) |
| | Hardness test | 2 sections (minimum) |
| | Leak test | 100% |
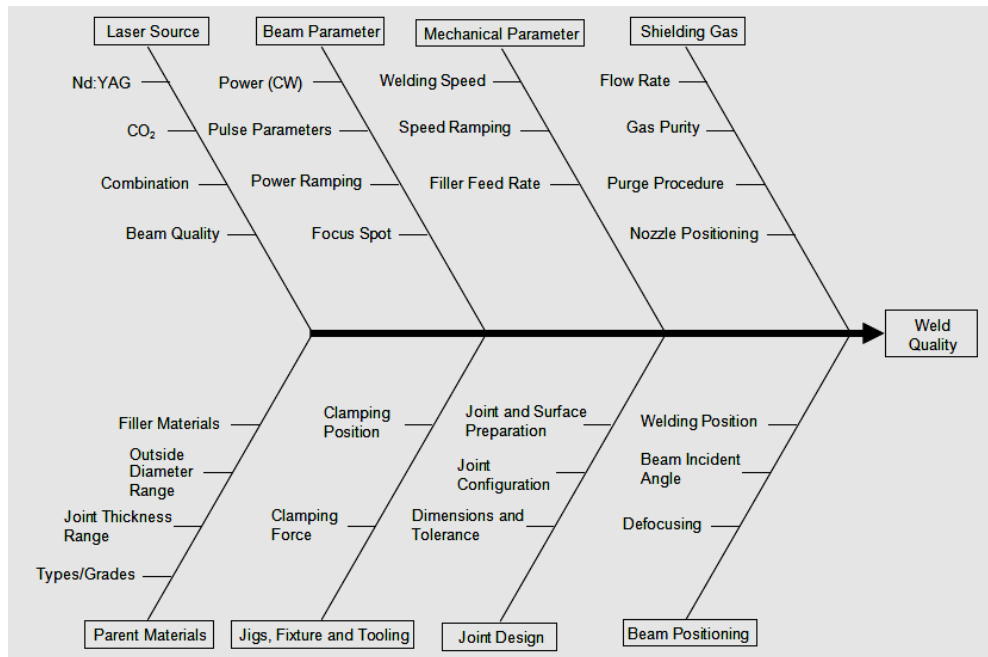


Fig. 1.7: Ishikawa diagram showing the factors affecting the laser weld quality

### 1.4.3 Factors affecting the weld quality

A structured analysis of a production process is necessary to understand the process itself and develop it further. Every production process is associated with a number of parameters that affect the result of the process. The result in this particular case is the weld seam. The parameters are of various kinds, and the extent to which they impact the result also varies.

The Ishikawa diagram is a useful tool for the structuring and analysis of a complex production process in terms of its parameters. As illustrated in Fig. 1.7, the main branch of the diagram represents the entire process of laser-welding of stainless steel, the result being the required quality of the joint.

As shown in Ishikawa diagram, the factors influencing the welding with laser can be summarized under the following heads:

12

- Laser source
- Parent materials
- Beam parameter
- Jigs, fixture and tooling
- Mechanical parameters
- Joint design
- Shielding gas
- Beam positioning (welding position, beam incident angle, defocusing etc.)

The main branches are further divided functionally to depict all the parameters directly affecting the result of the laser welding, each of which may have the significant effect on formation of microstructures, and geometry of the weld. These weld characteristics in turn determine the mechanical properties of the welded joints. The selection of the welding process parameters is therefore essential for obtaining the welded joint ensuring desired weld-bead geometry, excellent mechanical properties with minimum distortion [19-21].

### 1.4.4 Welding process optimization

The quality of a weld joint is directly influenced by the welding input parameters during the welding process and hence, welding can be considered as a multi-input multi-output process. A common problem that the manufacturer faces is the control of the process input parameters for obtaining optimal weld geometry with minimal detrimental residual stresses and distortion. Usually, the desired welding process parameters are determined based on the information obtained from experience and from handbooks. However, this does not ensure that the selected welding process parameters can produce the optimal or near optimal weld pool geometry for that particular welding machine and environment.

Table 1.4: Comparison among the most commonly used optimization techniques

| Comparison | Techniques | | | |
|---|---|---|---|---|
| | Genetic Algorithm | Response Surface Method | Taguchi Method | Factorial Design |
| Computational Time | Very long | Short | Medium | Short |
| Experimental Domain | Regular or Irregular | Regular only | Regular or Irregular | Regular only |
| Model Developing | No | Yes | No | Yes |
| Optimization | Straight | Through model | Straight | Through model |
| Understanding | Difficult | Easy | Normal | Easy |
| Optimization Accuracy Level | High | Very High | Normal | Very High |
| Application | Rarely | Frequently | Rarely | Frequently |

The important problem to be solved in welding engineering is, therefore, to develop a model for determining the optimal process parameters. In this context, as shown in Table 1.4, various optimization methods can be applied to define the desired output variables through developing mathematical models to specify the relationship between the input parameters and output variables. In this thesis, design of experiment (DOE) techniques, such as full factorial design (FFD) and response surface methodology (RSM) in particular, have been used to carry out such optimization [22].

Design of Experiments (DOE) refers to the process of planning, designing and analyzing the experiment so that valid and objective conclusions can be drawn effectively and efficiently. In order to draw statistically sound conclusions from the experiment, it is necessary to integrate simple and powerful statistical methods into the experimental design methodology. Though experimental design approach is a powerful technique used for exploring new processes, gaining increased knowledge of the existing processes, and optimizing these processes for achieving world class performance, the success of any industrially designed experiment depends on sound planning, appropriate choice of design, and statistical analysis of data and teamwork skills[ 23].

The three principles of experimental design such as randomization, replication and blocking can be utilized in industrial experiments to improve the efficiency of experimentation. These principles of experimental design are applied to reduce or even remove experimental bias. It is important to note that large experimental bias could result in wrong optimal settings or in some cases it could mask the effect of the really significant factors.

## 1.5 ANALYTICAL MODEL DEVELOPMENT

The computerized simulation and modeling of laser beam welding are of great practical importance [24]. In comparison with experimental studies, a modeling study can give detailed information concerning the characteristics of weld pool and their relationship with the welding process parameters and can be used to reduce the costs of experiments. For these reasons, researchers have been working towards a model for the laser beam welding process for roughly twenty years. These models range from simple moving line heat-source models [25-27] to complex models which account for fluid dynamics and laser–plasma interaction [28-30]. Besides, a semi-quantitative description of the keyhole mechanism and the conditions of energy and material transport were reported by Klemens [31]. A 3D model with a moving Gaussian heat source, using finite-difference numerical techniques, was also investigated by Chande and Mazumder [32]. However, each of these models is associated with a number of different complicated factors, such as weld pool dynamics, metal evaporation, plasma formation, absorption mechanism in the keyhole, and interaction between laser beam and plasma plume. These factors, in fact, make the developed models very difficult for the technician working in the production line to understand and hence to use them directly for estimating the weld geometry. A simple easy-to-use model is, therefore, needed to estimate the weld penetration depth directly from the selected welding parameters. In this context, a simplified energy based model has been developed for laser welding of ferritic stainless steels in overlap joint configuration.

## 1.6 RESEARCH MOTIVATION

Laser beam welding has become a significant industrial process because of its outstanding advantages as a bonding process over other widely used joining techniques. As an alternative to common adhesive or solders used for joining process, laser beam welding offers a number of attractive features such as elimination of filler material; narrow width and deep penetration; higher mechanical strength; greater resistance to vibration and shock; and minimum degradation of heat sensitive components during assembly; and increased reliability [33]. This technique also provides the low heat distortion, a non-contact process, repeatability, ability to automate, and high throughput, which, in turn, have led the industrial community to recognize, accept and value the laser's ability for precision welding. Besides, laser's versatility has also permitted the replacement of welding systems based on resistance (spot and seam), tungsten-inert-gas, ultrasonic and electron-beam welding [34]. Laser welding being precise, low cost, highly reliable and automated technique is now widespread in various industrial sectors ranging from microelectronics to shipbuilding [35]. In automotive industries, in particular, it is being increasingly used to weld the prefabricated small and heat sensitive complex parts of the fuel injector to automotive body with a view to organize several levels of sub-assemblies as the final part can not be made of a single piece.

Traditionally, stainless steels are classified mainly by their microstructure. The major basic groups are martensitic, ferritic, austenitic and duplex (austenitic & ferritic) materials. These stainless steels have good resistance to oxidation, even at high temperatures, and they are often referred to as high-resisting alloys. They are widely used in automotive sectors to manufacture different parts of an automotive vehicle also for their mechanical properties such as the combination of high strength and excellent formability together with an acceptable toughness and impact resistance in the finished components for most engineering applications.

In fabrication of stainless steel products, components, or equipment, manufacturers employ welding as the principal joining method. Most stainless steels are weldable, and a welded joint can provide optimum corrosion resistance, strength, and fabrication economy. Again, these mechanical properties together with the bead geometry of welded joint are the major factors deciding the welding quality. It is, therefore, utmost important to acquire the knowledge of how laser welding process parameters affect these weld bead characteristics, and how to optimize these parameters in order to produce excellent welded joints.

## 1.7 OBJECTIVES OF THE PRESENT RESEARCH

As stated in the previous sections, laser beam welding uses a moving and very high-density coherent optical source. The coherent nature of the laser beam allows it to be focused to a very small spot, leading to high energy densities. This possibility is a primary factor in establishing its potential for welding. The high joint completion rate achievable with laser welding is attractive for many applications, and this process can join virtually all grades of stainless steels.

Stainless steels may be grouped into five families, which differ from each other for the basic microstructure and the specific characteristics. The metallurgical features

of each group generally determine the weldability characteristics of the steel in that group. However, the weld or the HAZ can be different from the base metal in terms of hardness, strength, impact resistance, creep strength, and wear resistance as welding causes a significant alteration of the weld metal and heat-affected zone microstructures relative to the base metal. This can constitute a change in the desired phase balance, formation of intermetallic constituents, grain growth, segregation of alloys and impurity elements, and other reactions. In general, these lead to some level of degradation in properties and performance, and must be factored into the design and the manufacture.

Weld penetration depth, shape and final solidification structure of both fusion and heat-affected zones are determined by the manner in which the welding energy is applied to the joint. For laser welding, the energy input is controlled by the combination of the following parameters: laser power, welding speed, shielding gas, defocus distance, beam incident angle, and focal spot size. These being correct, the repetition of welding performance then depends on the material preparation, joint fit-up, and beam position accuracy. Thus, all the above mentioned parameters should be selected and optimized accurately in order to obtain a weld ensuring the required joint properties, and the equality of the exterior surface.

Besides, modeling study can be useful to know the detailed information of the weld pool geometry and eliminate the time- and cost-consuming activities currently practised in the fuel injector production line. In this context, development of a simplified model can be a solution to the concerning technicians to use the welding process parameters directly in order to estimate the weld penetration depth, a characteristic factor, that determine the desired weld resistance length and, with it, the shearing force of the welded joint.

Thus, the main objective of this PhD research is to conduct a set of scientific and systematic studies on laser welding of stainless steels with a view to acquire knowledge regarding various consequences of laser-material interactions and apply these directly as the solutions to the problems associated with laser welding in the production line. In these studies, continuous wave Nd:YAG laser is used to weld both the similar and the dissimilar stainless steels in constrained overlap and fillet joint configurations respectively. The research activities during the three years of doctoral degree can, therefore, be grouped into following three categories:

- Studying Nd:YAG laser welding of martensitic stainless steels in a constrained and circular overlap configuration. These studies include:

  - ✓ examining the effects of welding process parameters and energy density, an important process parameter in energy term, on the weld bead geometry and the mechanical properties;

  - ✓ investigating the effects of energy density input on weld microstructure evolution and the consequent changes in local microhardness at various weld zones, and

  - ✓ applying the experimental design approach to process parameter optimization for laser welding of the selected martensitic stainless steels.

- Studying Nd:YAG laser welding of dissimilar ferritic and austenitic stainless steels in a constrained and circular fillet joint configuration. These studies include:

  - ✓ examining the process parameters and line energy, another important process parameters from energy perspective, on the weld bead geometry and the mechanical properties,

  - ✓ performing metallurgical study to demonstrate the microstructures that typically form at different zones and the consequent changes in local microhardness,

  - ✓ applying the response surface methodology to process parameters optimization for laser welding of the selected dissimilar stainless steels,

- Developing a simplified energy-based model for Nd:YAG laser welding of ferritic stainless steels in overlap joint configuration.

The various activities performed to reach towards the aforesaid research goals are also illustrated schematically in the Fig. 1.8.
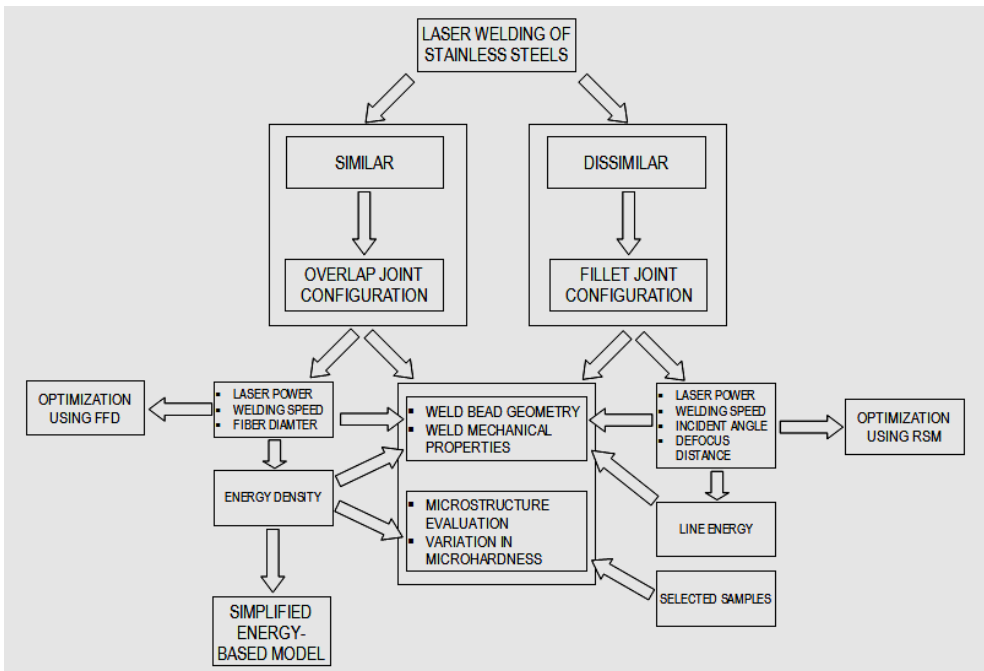


Fig. 1.8: Action plan showing the activities performed during the three years of PhD research.

## 1.8 THESIS STRUCTURE

The thesis outline is as follows; chapter one provides an introduction to the work with a brief description on why the laser welding of stainless steels is considered as the research topic. Chapter one also includes the weld quality, process optimization and analytical model development issues, research motivation, thesis

objectives, and thesis structure. Chapter two presents the experimental investigation of laser beam welding of martensitic stainless steels in a constrained and circular overlap joint configuration. Chapter three investigates the effects of energy density on development of microstructures and the consequent changes in local microhardness at various weld zones. This chapter also shows the correlation among the change in local microhardness, the evolution of microstructures, and redistribution of segregated ferrite- and austenite-promoting elements. Chapter four describes the application of experimental design approach to process parameter optimization for the laser welding of martensitic stainless steels discussed in chapter two. Chapter five examines the laser beam welding of dissimilar ferritic and austenitic stainless steels in fillet joint configuration. It also includes the metallurgical analysis on a selected weld showing only the solidification microstructure typically form at different location of the weld and the consequent variations in local microhardness. Chapter six details the application of response surface methodology to optimize the laser welding process described in the chapter five. Chapter seven presents a simplified energy based theoretical model for predicting the weld shape produced by a continuous wave Nd:YAG laser in a constrained overlap configuration on ferritic stainless steels.

## REFERENCES

1. Lancaster, J. F., 1984, The physics of welding, Physics in Technology, 15:73-79.
2. Kou, S., 2003, Fusion welding processes, In: Welding Technology, 2nd Ed., John Willey & Sons Inc., NJ, USA, pp.3-36.
3. Steen, W.M., Mazumder, J., 2010, Laser welding: laser material processing, 4th Ed., Springer-Verlag London Limited, UK, pp. 199-250.
4. Merchant, V., Laser beam welding, In: Ahmed, N., editor, New developments in advanced welding, 1st Ed., Woodhead Publishing Limited, Cambridge, UK, pp. 83-84.
5. Kugler, T.R., 2001, Fusion front penetration: Conduction Welding, In: Ready, J.F., editor, LIA handbook of laser materials processing, 1st Ed., Magnolia Publishing Inc., FL, USA, pp. 310-312.
6. Matsunawa, A., 2002, Science of laser welding-mechanisms of keyhole and pool dynamics. In: ICALEO 2002 proceedings, Phoenix, LIA, Orlando, paper: 101.
7. Lacroix, D., Jeandel, G., Boudot, C., 1996, Spectroscopic studies of laser-induced plume during welding with a Nd:YAG laser, In: Proceedings of SPIE, 2789, pp. 221–227.
8. Dumord, E., Jouvard, J.M., Grevey, D., 1996, Keyhole modeling during CW Nd:YAG laser welding, In: Proceedings of SPIE, 2789, pp. 213–220.
9. Berkmanns, J., Faerber, M., 2005, Facts about laser technology: laser welding, http://www.laserdeal.com/, access date: January 20, 2012.
10. Coherent Inc., 2004, High speed welding of metals with diamond $CO_2$ laser - stainless steels, Technical Note, http://www.coherent.de/, access date: November 15, 2011.
11. LWS, 2006, A technical report on the LWS flexcell cladding system, http://www.laserweldingsolutions.com/, access date: April 01, 2009.

12. Shannon, G., 2009, Source selection for laser welding, http://www.industrial-lasers.com/, access date: April 01, 2009.
13. Faerber, M., Berkmanns, J., 1996, Gases for increased laser welding productivity, In: Proceedings of the ISATA Conference, pp. 791–798.
14. Schuberth S, Schedin E, Fröhlich T, Ratte E., 2008, Next generation vehicle – engineering guidelines for stainless steel in automotive applications, In: Proceedings of the 6th stainless steel science and market conference, Helsinki, Finland.
15. Kou, S., 2003, Weld metal solidification, In: Welding Technology, 2$^{nd}$ Ed., John Willey & Sons Inc., NJ, USA, pp.199-207.
16. Han, W., 2004, Computational and experimental investigations of laser drilling and welding for microelectronic packaging, Ph.D. Dissertation, Worcester Polytechnic Institute, Worcester, MA, USA, pp. 85-87.
17. Buchfink, G., 2007, A world of possibilities – joining, In: Kammüller, N.L., editor, The laser as a tool, 1$^{st}$ Ed., Vogel Buchverlag, Würzburg, Germany, pp. 166-167.
18. ISO13919-1:1996, Welding - Electrons and laser beam welded joints – guidance on quality levels for imperfections - Part I: Steel, pp. 4-13.
19. Zhang, Y.M., Kovacevic, R., Li, L., 1996, Characterization and real time measurement of geometrical appearance of the weld pool. International Journal of Machine Tools and Manufacture, 36(7):799–816.
20. Bull, C.E., Stacey, K.A., Calcraft, R., 1993, Online weld monitoring using ultrasonic. Journal of Non-destructive Test, 35(2):57–64.
21. Tarng, Y.S., Yang, W.H., 1998, Optimization of the weld bead geometry in gas Tungsten Arc welding by the Taguchi Method. Journal of Advanced Manufacturing Technology, 14:549–54.
22. Benyounis, K.Y.,Olabi, A.G.,Hasmi, M.S.J., 2008, Multi-response optimization of $CO_2$ laser welding process of austenitic stainless steel, Optics & Laser Technology, 40:76–87.
23. Antony, J., 2003, Introduction to industrial experimentation, In: Design of Experiments for Engineers and Scientists, Elsevier Publishing Solutions, USA, pp. 1-4.
24. Sudnik, W., Radaj, D., Erofeev, W., 1996, Computerized simulation of laser beam welding, modeling and verification, Journal of Physics D: Applied Physics, 29:2811-2817.
25. Arata, Y., Miyamoto, I., 1972, Heat processing by $CO_2$ laser, Journal of Japan Welding Society, 41:81.
26. Swift-Hook, D.T., Gick, A.E.F., 1973, Penetration welding with lasers, Welding Journal Research Supplement,  52:492s–9s.
27. Steen, W.M., Dowden, J., Davis, M., Kapadia, P., 1988, A point and line source model of laser keyhole welding, Journal of Physics D, 21:1255–60.
28. Dowden, J., Davis, M., Kapadia, P., 1983, Some aspects of the fluid-dynamics of laser-welding. Journal of Fluid Mechanics, 126:123–46.
29. Ducharme, R., Kapadia, P., Dowden, J., 1993, A mathematical model of the defocusing of laser light above a workpiece in laser material processing. In: Farson, D., Steen, W., Miyamoto, I., editors, Proceedings of ICALEO'92, LIA, Orlando: Laser Institution of America, 75:187–97.

30. Kaplan, A., 1994, A model of deep penetration laser welding based on calculation of the keyhole profile, Journal of Physics D: Applied Physics, 27(9):1805–1814.
31. Klemens, P.G., 1976, Heat balance and flow conditions for electron beam and laser welding, Journal of Applied Physics, 47(5):2165–2174.
32. Chande, T., Mazumder, J., 1984, Estimating effects of processing conditions and variable properties upon pool shape, cooling rates, and absorption coefficient in laser welding, Journal of Applied Physics, 56:1981–6.
33. Borland, J.C., 1960, Generalized theory of super-solidus cracking in welds (and castings), British Welding Journal, 7: 508–512.
34. Hemsworth, B., Boniszewski, T., Eaton, N.F., 1969, Classification and definition of high temperature welding cracks in alloys, Metal Construction and British Welding Journal, 2:5–16.
35. Hoffmann, P., Geiger, M., 1995, Recent developments in laser system technology for welding applications, Annals of the CIRP, 44(1):151-156.

# CHAPTER 2

## LASER BEAM WELDING OF MARTENSITIC STAINLESS STEELS IN AN OVERLAP JOINT CONFIGURATION

*This chapter examines laser beam welding of martensitic stainless steels in a constrained overlap configuration. Experimental investigations are focused on the effects process parameters such as laser power, welding speed, fiber diameter and energy density on the bead geometry and the mechanical properties of the weld.*

*Laser power and welding speed are found to be the most significant factors affecting the weld bead geometry and shearing force. Except on the weld width, fiber diameter has little effect on the aforestated response factors. Nonetheless, combining with other parameters, fiber diameter is found to have significant effect on them. The contour plots showing constant response lines indicate the evidence of two-factor interaction effects of laser power-welding speed, welding speed-fiber diameter, and fiber diameter-laser power on all the response factors except the weld width.*

*Energy density plots illustrate its linear relationship with penetration depth and limited nonlinear effects on the others. Weld shearing force varies almost linearly with weld resistance length. Both weld resistance length and shearing force are energy-limited. These factors vary positively with energy density input up to a certain limit. After that limit, any additional increase in energy input only increases the weld penetration depth and no longer affects the weld resistance length. As a result, bead profile changes its shape from conical to cylindrical.*

*Both shrinkage and deformation occur during laser welding. However, amount of shrinkage and behavior of deformation were found unequal and non-uniform respectively for the repeated experiments.*

## 2.1 INTRODUCTION

Laser welding is a high-energy-density welding process and well known for its deep penetration, high speed, small heat-affected zone, fine welding seam quality, low heat input per unit volume, and fiber optic beam delivery as mentioned by Weichiat et al. [1]. As a result, it has been increasingly utilized in all industrial sectors like automobile, ship building, electronic industry, etc. Nowadays, in automotive industries, fabrication of modern fuel injectors for gasoline, diesel, and gaseous fuels incorporates laser welding to improve quality and maximize production throughput. Of the lasers used in automotive industries to weld small and heat sensitive complex parts of a fuel injector, continuous wave (CW) Nd:YAG laser performs best for welding because of its short time cycles and metallurgy of the stainless steels used. These stainless steels may be grouped into five families, which differ from each other for the basic characteristics of the steel in that group. Among various groups of stainless steels, martensitic stainless steels are seldom welded because of their high hardenability and susceptibility to hydrogen induced or cold cracking. However, martensitic AISI 416 and AISI 440FSe stainless steels with their chromium and carbon contents are resistant to various environments such as fresh water, steam, crude oil, gasoline, perspiration, and alcohol and have a good machinablilty characteristics as well. Their molybdenum content also provides the elevated-temperature strength through the formation of stable carbide as stated by Lippold and Kotecki [2]. Besides, the low-chromium and low-alloy element content of these martensitic stainless steels make them less costly than the other types. Because of their good creep, tensile and fatigue strength properties in combination with moderate corrosion & heat resistance, and low-cost benefit, these steels are prominently used in automotive sector to fabricate gears, shafts, seats for oil pumps, valve parts and fuel injectors etc.

Besides, the laser beam welding involves many variables; laser power, welding speed, defocusing distance, beam incidence angle and type of shielding gas, any of which has a considerable effect on heat flow and fluid flow in the weld pool and hence, significantly affects penetration depth, shape and final solidification structures of both fusion and heat affected zones. Both the shape and microstructure of the fusion zone determine the properties of the joint and the equality of the exterior surface. As a high energy density and low heat input process, Nd:YAG laser beam welding causes a small heat-affected zone (HAZ), which cools very rapidly with very little distortion and a high depth-to-width ratio for the fusion zone.

On account of the widespread use of stainless steels and their importance in critical industrial technologies, it is, therefore, justified to show the wide interest of researchers and technicians on weldability and service integrity of such materials. There are many reports, which deal with the weld bead profile, mechanical properties, and solidification structure of the fusion zone of Nd:YAG laser beam welds in relation to different laser parameters and materials. Brooks and Garrison [3] studied the weld microstructural evolution, mechanical properties and solidification cracking susceptibility of three precipitation-strengthened martensitic stainless steels such as PH 13-8 Mo, Custom 450 and 15-5 PH. Liquid tin quenching of gas tungsten arc welds revealed that all three welds solidified as single-phase ferrite with a high degree of microsegregation. However, during

further solidification and cooling almost complete homogenization occurred as a result of solid-state diffusion. The welds in all three alloys exhibited good resistance to solidification cracking and generally exhibited tensile and impact properties similar to those of the base metal. However, in almost all cases, the weld Charpy impact energies were somewhat less than those of the base metals. The cracking behavior and mechanical properties were also discussed in terms of microstructural evolution. Tzeng [4] presented a parametric analysis of the pulsed Nd:YAG laser seam welding (PLSW) process. It also included the descriptions of overlap theory and welding mechanism, and the formulation of relevant mathematical equations. Seam welds were produced in 0.75 mm thick bare steel sheets in lap joint configuration to investigate systematically the effects of laser parameters such as mean laser power, average peak power density (APPD), pulse energy, and traversing speed on heat flow. It was concluded that heating effect increased with an increase in pulse duration for a given mean power, travel speed and APPD, and enhanced by APPD, when mean power and traverse speed were kept constant. Hector et al. [5] characterized the texture of Nd:YAG laser welds of AA5182-O and AA6111-T4 alloys. Autogenously bead-on-plate welds were produced with a flash lamp-pumped, 3 kW CW Nd:YAG laser on 2-mm thick sheets with mill finishes and sheets were not exposed to any cleaning processes prior to the welding test. Laser was delivered by an optic of 200 mm focal length and the weld speed was held fixed at 100 mm/s for all tests.  Electron back scattering diffraction (EBSD) in the scanning electron microscope was used to determine the texture. The determination was made as a function of thickness through the sample. The results showed that the welds could develop significant texture. In particular, the columnar grains that grew from the base metal into the weld had a strong 001 texture along the direction of growth. Al-Kazzaz et al. [6] studied experimentally the effects of welding speed on Nd:YAG laser weldability of  ZE41A-T5 magnesium sand casting. During experimentation, the 2-mm butt joints were welded using 1.6 mm EZ33A-T5 filler wire and a continuous wave Nd:YAG system at a power of 4 KW, surface defocusing, and various welding speeds. Compared with the base metal, the fusion zone showed significant grain refinement and no grain coarsening was observed in heat affected zone (HAZ).The porosity area percentage, total solidification crack length and HAZ width were found to decrease with the increased welding speed. However, fusion zone area, total penetration depth, and weld width also decreased with increase in welding speed. Huang et al. [7] investigated the effects of multipass hybrid welding of austenitic stainless steel structure by using low power pulsed Nd:YAG laser- metal active gas (MAG) arc on the microstructure, phase composition, weld post heat influence, and weld bead (WB) precipitated phase. The results demonstrated that sound welded joints without any solidification and shrinkage defects could be obtained after welding. The top and the bottom portions of the work pieces were joined completely. At room temperature, the microstructures of different regions in WB were different and the WB microstructures were composed of columnar γ-austenite and δ-ferrite phases. The fraction of δ-ferrite decreased from 20% to 10%, and its morphology changed orderly from lath, skeleton, vermicular to reticular with an increase in the number of welding cycles. Because of the influence of post weld heat, the weld metal phase chemistry at 3 mm distance from the top of the WB surface underwent a notable modification that corresponded to an evolution of the partition coefficients toward the parent metal values. Liu et al. [8] showed the effect of temperature

variation and clamping force on Nd:YAG laser butt welding of steel work piece of various thicknesses. In this study, experiments were conducted under different preset clamping forces. Variation on the clamping force and temperature were measured simultaneously and the strength of the welded samples was tested. It was found that there was an optimal preset clamping force that improved the weld joint strength significantly and the welding temperature during steady welding process remained unchanged for any preset clamping force.

### 2.1.1 Research objectives

As seen from the literature review, the effect of influencing parameters of laser welding depends largely on several factors such as alloy type, bead-geometry requirements, degree of confinement as well as joint type, and has to be researched separately for each new component and alloy. This chapter will, therefore, examine Nd:YAG laser welding of martensitic AISI 416 and AISI 440FSe stainless steels in a constrained and circular overlap configuration. Experimental studies are focused on:

- effects of laser parameters such as laser power, welding speed and fiber diameter and their interactions on
  - ✓ the weld bead geometry such as weld width, penetration depth and resistance width,
  - ✓ the mechanical properties of the weld such as shearing force i.e. resisting force to shear across the weld.
- effects of energy density input, an important parameter that correlate all the aforestated welding parameters, on
  - ✓ the weld bead geometry such as weld penetration depth, and resistance width to understand the energy dependent welding phenomena, and
  - ✓ the mechanical properties of the weld such as weld shearing force and shrinkage to show consequence of these energy dependent phenomena, and
- finally, selection of allowable working range of process parameter in energy term based on the results obtained from the above-mentioned studies.

### 2.2 MATERIALS AND EXPERIMENTAL PROCEDURES

### 2.2.1 Materials

The martensitic AISI 440FSe and AISI 416 stainless steels normally used in automotive industries for making respectively inner and outer shells of a fuel injector are selected as base metals for the constrained overlap weld fabrication. The chemical compositions of the base metals and weld bead characteristics are shown in Table 2.1 and Fig 2.1 respectively. The inside diameter of outer shell and the outside diameter of inner shell are machined to Ø7.5±0.025mm and Ø7.458±0.015mm respectively. These two parts are first assembled together so that there is a clearance between them and then crimped applying a uniform force of 12kN around the tip of outer shell, which is a replication of actual fabrication process
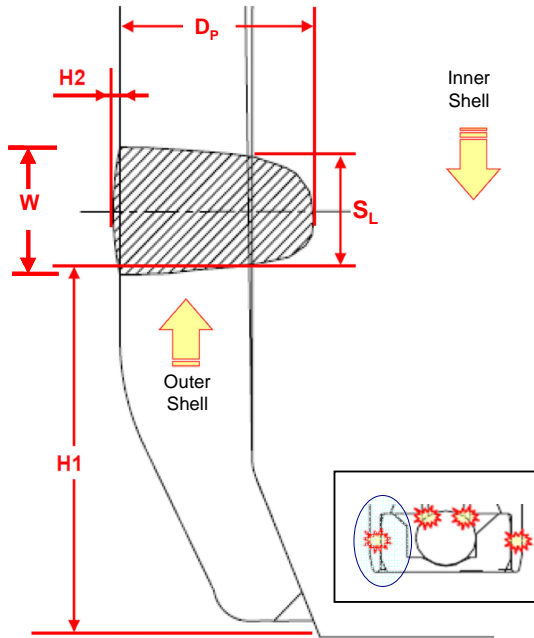
Fig 2.1: Characterization of welding cross-section (W: Weld width, $D_P$: Weld penetration depth, $S_L$: Weld resistance length)

Table 2.1: Chemical compositions of base metals of the weld

| Base Metals | Chemical Compositions (%Wt) | | | | | |
|---|---|---|---|---|---|---|
| | C | Cr | Mn | Mo | Si | S |
| AISI 440FSe | 0.60 | 17.0 | 1.00 | 0.75 | 1.0 | - |
| AISI 416 | 0.15 | 13.0 | 1.25 | 0.60 | 1.0 | 0.15 (min) |

### 2.2.2 Laser welding experimental procedures

Welding tests are planned based on statistical factorial experimental design with replication. Laser power, (P), welding speed (S), and fiber diameter (F) are considered as the laser welding input factors. Each factor and its working range were selected based on experts' opinions and industrially recommended laser welding parameters used in automotive industries. In this study, specimens are welded circularly in an overlap joint configuration using Nd:YAG continuous wave laser (Rofin DY011). During experimentation, laser power and welding speed are varied in the range 800-1100W and 4.5-7.5 m/min respectively. The optical system consisted of 300μm and 400μm fibers along with two lenses of 200 mm focal length and collimating length are used to deliver the laser with a focal spot diameter of 300μm and 400μm respectively.

Besides, energy density is often used in various laser-processing techniques and termed as a key-parameter when continuous-wave laser is used. It correlates the process parameters stated above and expresses them from the energy perspective

as described by Berzins et al. [9]. As a matter of fact, this single factor provides the effects of three-factor interactions on geometry and mechanical properties of the weld. This term is calculated using the same equation as Childs et al., [10] derived:

$$ED = \frac{P \times \phi_{spot}}{S} \tag{1}$$

where, ED is energy density, P is laser power describing the thermal source, S is welding speed determining the interaction time, and $\phi_{spot}$ is focal spot diameter defining the area through which energy flows into the material. It has already been described that this focal spot diameter is the same as fiber diameter for the optical system used to focus the laser during welding. Deriving from equation (1), energy density input corresponding to the above-mentioned ranges of process parameters is found in the range of 16.0-48.9 J/mm$^2$.

Table 2.2: Experimental conditions and response Factors

| Process Factors | Symbols | Levels of Each Factor | | |
|---|---|---|---|---|
| | | 1 | 2 | 3 |
| Laser power (W) | P | 800 | 950 | 1100 |
| Welding speed (m/min) | S | 4.5 | 6.0 | 7.5 |
| Fiber Diameter (µm) | F | 300 | - | 400 |
| Constant Factors | | | | |
| Base material | : | Outer Shell : AISI 416<br>Inner Shell : AISI 440 FSe | | |
| Laser source | : | Nd:YAG Laser | | |
| Angle of Incidence (deg) | : | 90° (onto the surface) | | |
| Shielding gas | : | Type : Argon<br>Flow rate : 29 l/min | | |
| Response Factors | | | | |
| Weld bead characteristics | : | Weld Width (W), Resistance Length ($S_L$), and Penetration Depth ($D_p$) | | |
| Mechanical properties | : | Weld Shearing Force ($F_s$) and Shrinkage | | |
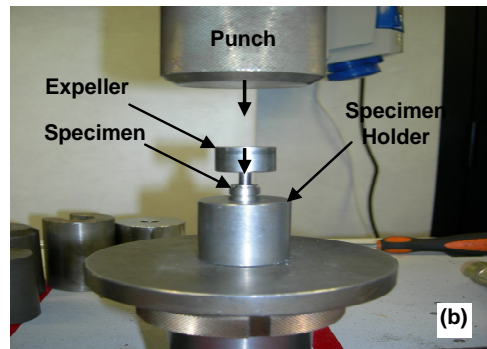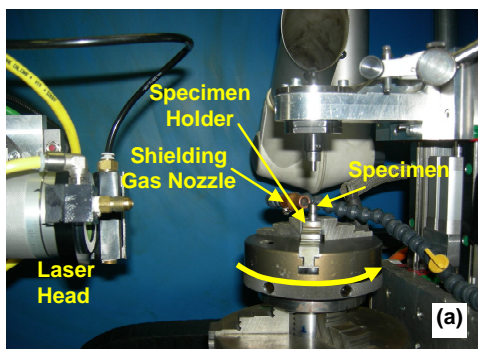


Fig 2.2: Photographic views of the experimental set-up for (a) laser welding and (b) shearing test

Experimental conditions and response factors considered have been shown in Table 2.2. During welding operation, the laser is focused normally onto the specimen surface and argon is supplied as a shielding gas at a constant flow rate of 29 l/min to protect heated surface from oxidation. A standard washing procedure practised in the automotive industries is followed to clean, cool and dry the specimens. No special heat treatment is carried out after welding. Photographic views of the experimental set-up for laser welding and push out test have been shown in Figs 2.2(a) and (b) respectively.

### 2.2.3 Mechanical characterization

The constrained overlap welding experiments are carried out according to the design matrix in a random order to avoid any systematic error in the experiment. After welding, specimens are first visually inspected, then sectioned axially to obtain transverse sections of the weld bead under various welding conditions. The sectioned specimens are finally prepared for metallographic analyses following the standard procedure recommended for martensitic stainless steel.

Table 2.3: Design matrix with actual factors and measured mean responses

| Process Factors | | | Response Factors | | | |
|---|---|---|---|---|---|---|
| P (W) | S (m/min) | F (mm) | W ($\mu$m) | $D_p$ ($\mu$m) | $S_L$ ($\mu$m) | $F_s$ (N) |
| 800 | 4.50 | 300 | 490 | 960 | 440 | 5910 |
| 950 | 4.50 | 300 | 490 | 1290 | 480 | 6022 |
| 1100 | 4.50 | 300 | 580 | 1610 | 500 | 6775 |
| 800 | 6.00 | 300 | 530 | 710 | 370 | 6233 |
| 950 | 6.00 | 300 | 520 | 950 | 470 | 6129 |
| 1100 | 6.00 | 300 | 510 | 1180 | 450 | 6355 |
| 800 | 7.50 | 300 | 530 | 560 | 210 | 2999 |
| 950 | 7.50 | 300 | 590 | 730 | 390 | 5886 |
| 1100 | 7.50 | 300 | 590 | 880 | 510 | 6861 |
| 800 | 4.50 | 400 | 572 | 790 | 529 | 5722 |
| 950 | 4.50 | 400 | 612 | 1043 | 586 | 5809 |
| 1100 | 4.50 | 400 | 638 | 1307 | 613 | 6730 |
| 800 | 6.00 | 400 | 622 | 577 | 266 | 4457 |
| 950 | 6.00 | 400 | 699 | 727 | 481 | 6154 |
| 1100 | 6.00 | 400 | 771 | 920 | 588 | 5942 |
| 800 | 7.50 | 400 | 600 | 492 | 33 | 1897 |
| 950 | 7.50 | 400 | 721 | 580 | 273 | 2602 |
| 1100 | 7.50 | 400 | 732 | 749 | 442 | 5044 |

Software, Leica IM500, incorporated with an optical microscope (Leica MZ125) is used to measure various characteristics of the weld bead. The average value of each of the measured response parameters of the weld bead is determined and recorded for further analysis. Main and interaction effects of process parameters on the weld bead characteristics (e.g. weld width, penetration depth, and resistance length) and shearing force (one of the mechanical properties of the weld bead) are analyzed using perturbation and contour plots respectively. Again, push out or

shearing tests are accomplished at room temperature (22 °C) using Instron push out press (model: 3367) to determine shearing load to failure of the welds fabricated under various conditions. During shearing test, specimens are set on a specimen holder or vice and pushed axially by a specially designed expeller so that the specimen fails due to shear across the weld. The design matrix with actual factors and measured responses has been shown in Table 2.3. Besides, as a measure of deformation that takes place in inner shell, the amount of shrinkage due to laser welding are assessed by measuring its internal diameter before and after welding with 'Quickscope' system. In this experiment, twelve specimens are welded circularly in an overlap joint configuration under the following condition: laser power and welding speed are kept fixed to 950W and 6.0 m/min respectively and the laser is focused normally onto the outer shell surface at a spot diameter of 300µm.

## 2.3 RESULTS AND DISCUSSION

### 2.3.1 Effects on weld bead characteristics

Weld bead profiles are measured using the axial sectioned specimens and optical microscope as mentioned in section 2.2.3 and recorded for further analysis as described in succeeding sections.

Perturbation curve is used to demonstrate the effects of individual process parameter such as laser power, welding speed and fiber diameter on weld width, penetration depth, resistance length and shearing force.

The effects of two-factor interactions such as laser power-welding speed, welding speed-fiber diameter and fiber diameter-laser power on the aforestated weld geometry and mechanical properties are described using the contour plots.

Moreover, energy density correlating the abovementioned process parameters and expressing them from energy perspective is plotted with the weld penetration depth, resistance length, and shearing force to show the effects of energy density input on the aforestated response factors.

### 2.3.1.1 Weld profile aspects

Fig 2.3 is the composite photograph showing the effect of energy density, a function of laser power and welding speed, on keyhole profiles for the 300µm fiber. As shown in Fig 2.4, the keyhole profiles were also drawn by measuring the position of the front keyhole walls up to weld bead tip from the photos given in Fig 2.3(a) where energy density was varied in the range 21-36 J/mm$^2$. It can be pointed out from Figs 2.3 and 2.4 that the keyhole shape is nearly cone-shaped and its vertex angle decreases as the keyhole depth increases with increasing energy density (ED) input. When the keyhole is deep enough, keyhole diameter at different depth varies a little and the shape of keyhole is found quite similar to a cylinder. From these figures, it is also found that curvature of the keyhole profile is closely related to welding speed. The higher the welding speed the larger the curvature of the keyhole.

4.5 m/min     6.0 m/min     7.5 m/min        4.5 m/min     6.0 m/min     7.5 m/min

**(a)**   ED: 21~36 J/mm$^2$        **(b)**   ED: 29~49 J/mm$^2$
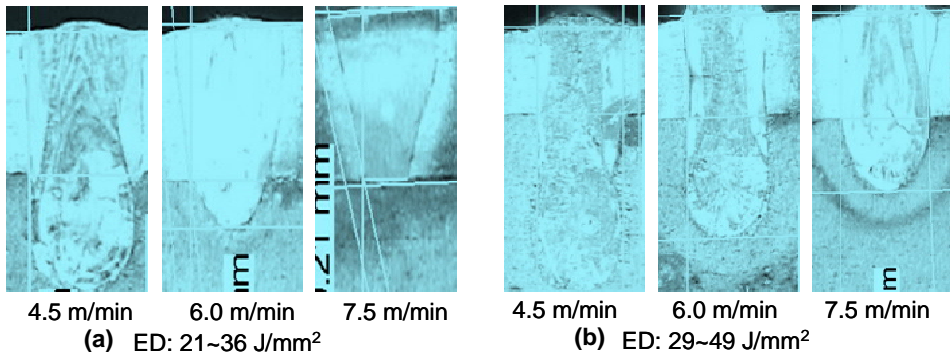
Fig 2.3: Composite photograph of keyhole profile at different welding speed and power
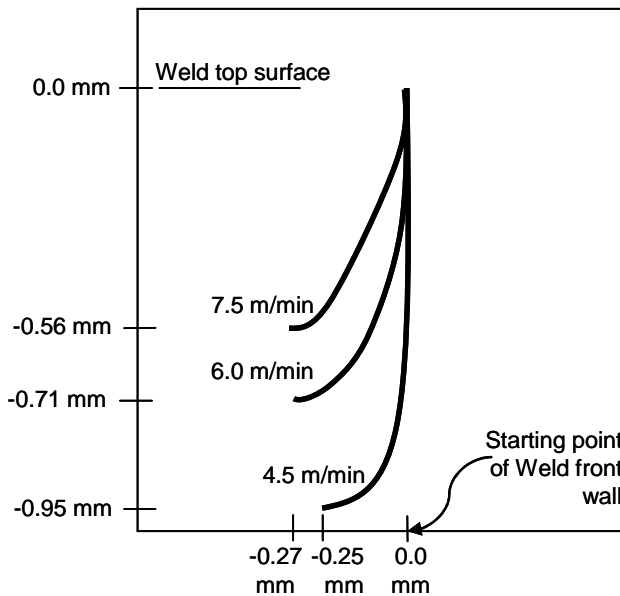


Fig 2.4: Relationship between curve of the keyhole and welding speed for P=800W

**2.3.1.2 Weld width**

Fig. 2.5(a) is a perturbation plot illustrating the effect of individual laser welding parameter, whereas Figs 2.5 (b)-(d) are the contour graphs showing the effects of two-factor interactions on weld width. From perturbation plot, it is clear that fiber diameter is the most significant factor affecting the weld width. The fiber with larger diameter provides the larger focal spot for this particular optical system and as consequence; heat energy is distributed over a larger area. As a result, with an increase in fiber diameter, wide area of the base metal melts and results in a wider weld width or vice versa. Moreover, the results show that laser power contributes a secondary effect on weld width. An increase in laser power results in increased weld width due to increased energy density input over the focused area. Though the variation is not significant, it varies positively with the increasing welding speed,

which is quite similar to the result obtained from an experimental study conducted by Jin and Li [11]. This result may be due to combined effect of welding speed and fiber diameter resulting in less energy density input over a wide area for a short period of time. Moreover, the increased welding speed increases the contribution of conductive and translatory heat transport and results in increased weld convexity as described by Sudnik et al [12].
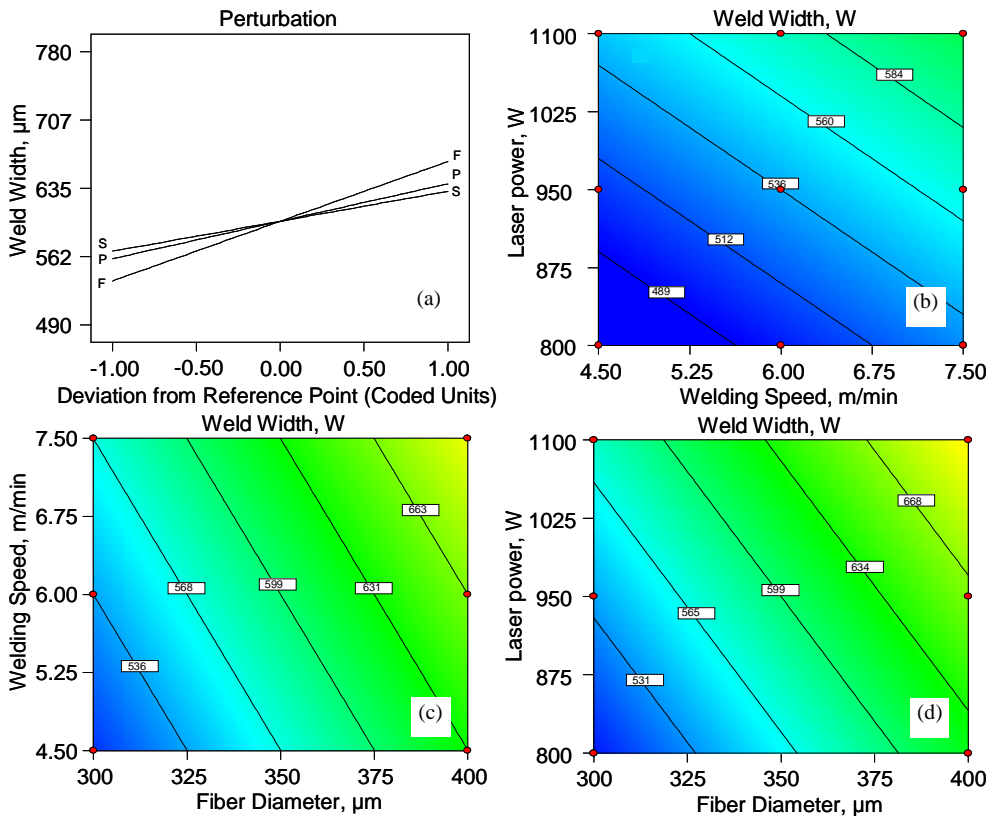


Fig 2.5 (a) Perturbation plot showing the effects of all factors, and contour graphs illustrating the interaction effects of (b) P and S for F = 300µm; (c) S and F for P = 950W; and (d) P and F for S= 6 m/min on weld width

Again, the aforestated contour plots indicate no interaction effects of laser power-welding speed, welding speed-fiber diameter and fiber diameter-laser power on weld width as the resulting constant weld width lines are straight as stated by Antony [13].

### 2.3.1.3 Weld penetration depth

From perturbation plot, as shown in Fig 2.6(a), it is evident that weld penetration depth increases and decreases significantly with increase in laser power and welding speed respectively, whereas a slight decrease in weld penetration depth is observed with the increase in fiber diameter. The increasing laser power leads to increased energy density input causing more metal to melt and consequently, more

penetration is achieved. However, the opposite phenomenon is observed for welding speed, as increased welding speed lessens the interaction time and hence, provides less time for the heat energy to flow deep into the material. Again, the use of a fiber with a smaller diameter results in smaller focal spot and hence, increased energy density. Consequently, heat energy localizes in a small portion of metal and results in deeper weld penetration. This phenomenon can be attributed to linear positive relationship existing between penetration depth and energy density input as shown in Fig 2.6(b).
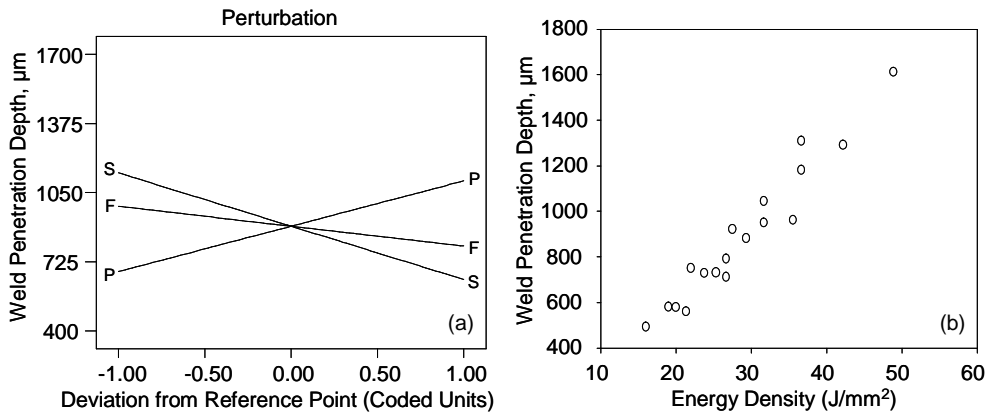


Fig 2.6: (a) perturbation plot showing the effect of all factors on weld penetration depth, and (b) variation in weld penetration depth with energy density input
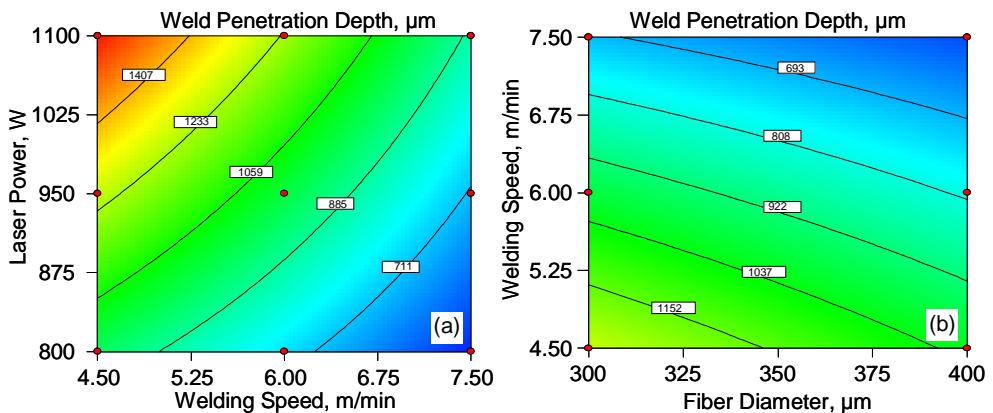


Fig 2.7: Contour graphs to show effects of (a) P and S for F= 300μm, and (b) S and F depth for P = 950W on weld penetration depth.

Again, from the contour plots illustrated in Figs 2.7(a)-(c), the effects of the afore-mentioned two-factor interactions are apparent as the constant weld penetration depth lines obtained from the experimental results are curved as described in [13]. Of the three two-factor interactions, the interaction effect of laser power-welding speed is the most significant. Moreover, it is evident that various combinations of these parameters are possible to obtain the desired penetration depth. It can, therefore, be concluded that a combination of higher laser power, lower welding

speed, and smaller fiber diameter needs to be selected within the specified range to obtain a weld with deeper penetration.
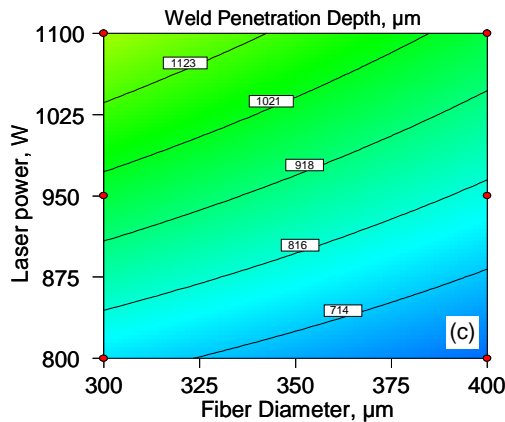


Fig 2.7 (c): Contour graph to show effects of P and F on penetration depth for S = 6 m/min

### 2.3.1.4 Weld resistance length

Perturbation plot shown in Fig 2.8 reveals that weld resistance length increases and decreases significantly with increase in laser power and welding speed respectively. However, change in fiber diameter has no or a little effect on weld resistance length. As mentioned in the preceding sections, increase in laser power increases energy density input and consequently, weld resistance length becomes larger. On the other hand, higher welding speed lessens the interaction time causing less interaction of energy input with material. As a result, weld resistance length decreases as a consequence of increased welding speed.
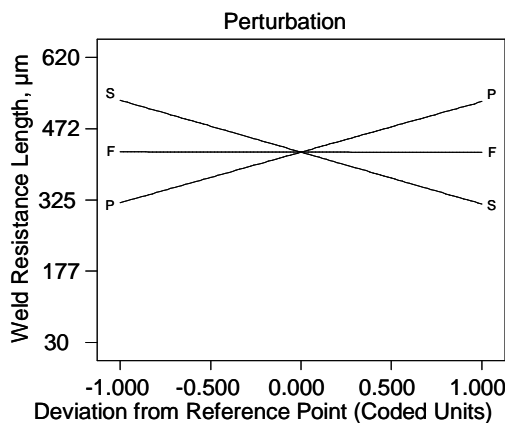


Fig 2.8: Perturbation plot showing the effect of all factors on weld resistance length.

Again, the contour plots shown in Figs 2.9(a)-(c) indicate that the effects of aforestated two-factor interactions on weld resistance length are evident as the resulting constant resistance length lines are curved.
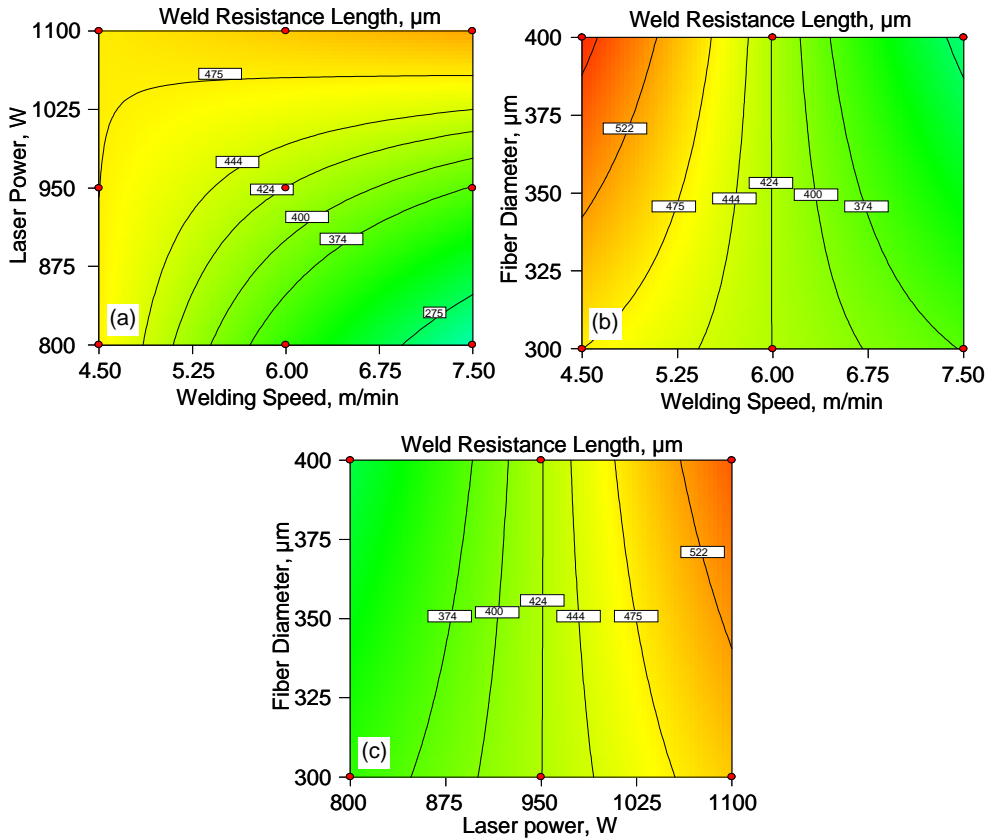
Fig 2.9: Contour graphs illustrating the interaction effects of (b) P and S for F = 300μm, (c) S and F for P = 950W, and (d) P and F for S= 6 m/min on weld resistance length.
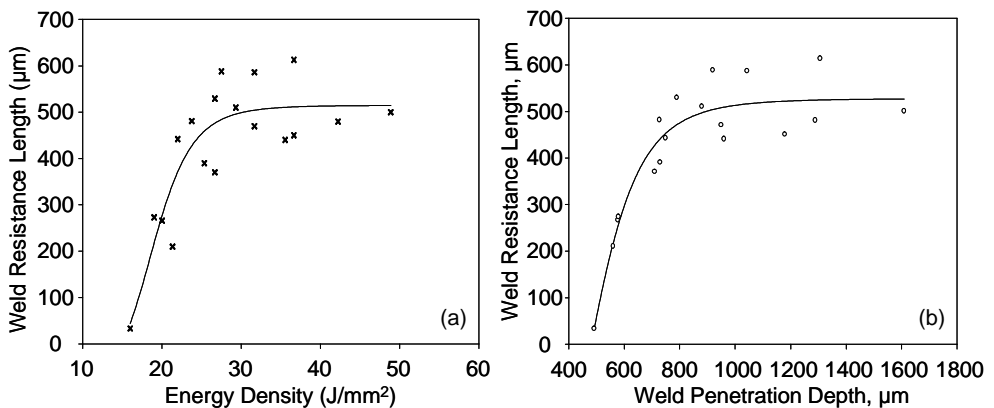


Fig 2.10: Variation in weld resistance length with energy density input, (b) relationship between weld resistance length and penetration depth.

However, from the relationship between weld resistance length and energy density as illustrated in Fig 2.10(a), it is found that the weld resistance length increases

with an increase in energy density input up to a certain level. After that level, as shown in Figs 2.6(b), 2.10(a) and (b), any additional increase in energy density input only increases penetration depth and no longer affects weld resistance length. Consequently, bead profile changes its shape from conical to cylindrical, which has also been reported by Jin and Li [11]. It can, therefore, be concluded that various combinations are possible to obtain the desired weld resistance length. However, the maximum obtainable weld resistance length is restricted to a certain limit for the specified welding conditions and weld configuration.

## 2.3.2 Effects on mechanical properties

### 2.3.2.1 Weld shearing force

Fig 2.11 is a perturbation plot that shows the main effect of process parameters considered on the shearing force. From the perturbation plot, it is apparent that shearing force increases and decreases significantly with increase in laser power and welding speed respectively. However, variation in fiber diameter has less effect on shearing force compared to other two factors. With an increase in laser power, weld resistance width increases and consequently, shearing force becomes larger in magnitude. Again, higher welding speed and larger fiber diameter result in reduction in weld resistance length, which, in turn, cause reduction in shearing force of the weld.
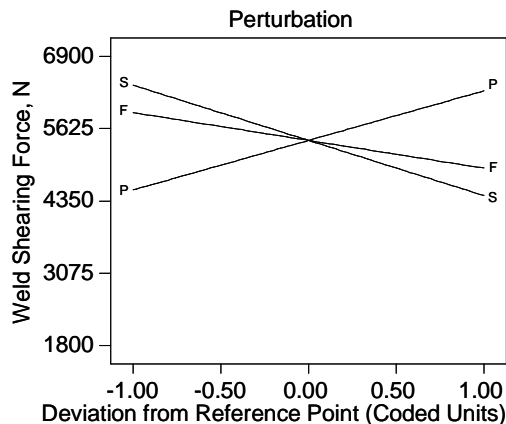


Fig 2.11: Perturbation plot showing the effect of all factors on weld shearing force.

Figs 2.12(a)-(c) are the contour graphs that describe the aforementioned two-factor interaction effects on weld shearing force. The aforestated figures show that interaction effects of laser power-welding speed and welding speed-fiber diameter on shearing force are evident. However, maximum achievable shearing force from these interactions is limited. Besides, there is no interaction effect of fiber diameter-laser power on shearing force as the resulting constant shearing force lines are straight.

34
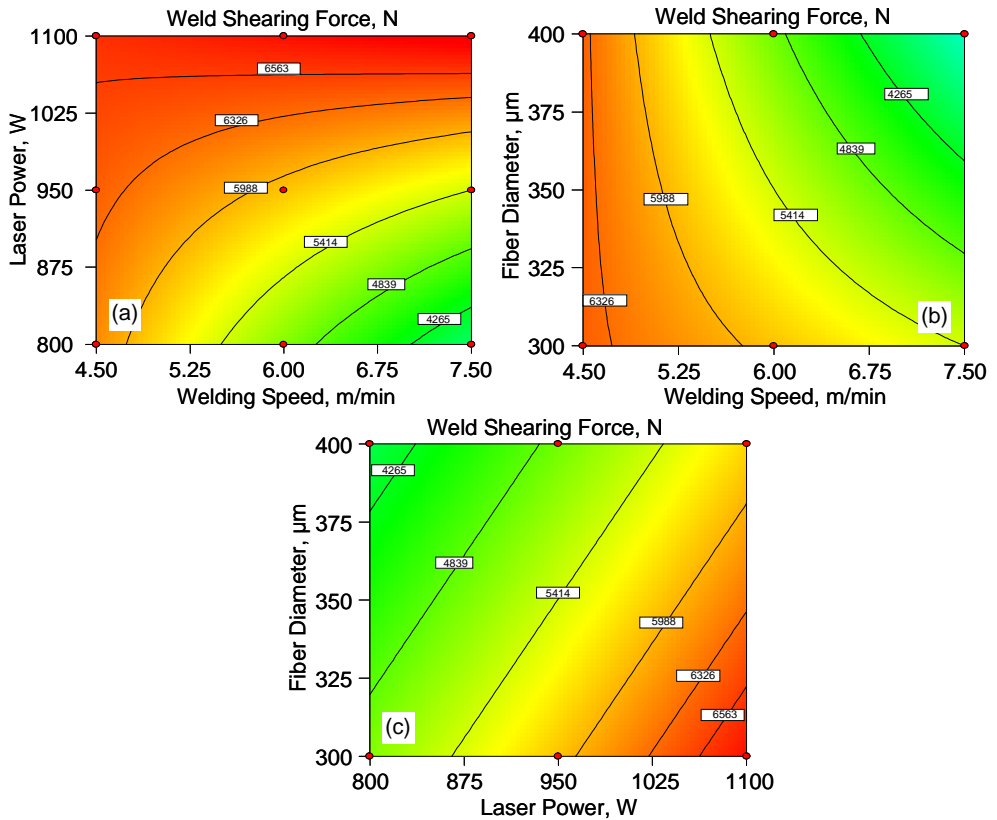
Fig 2.12: Contour graphs illustrating the interaction effects of (b) P and S for F = 300μm, (c) S and F for P = 950W, and (d) P and F for S= 6 m/min on weld shearing force.
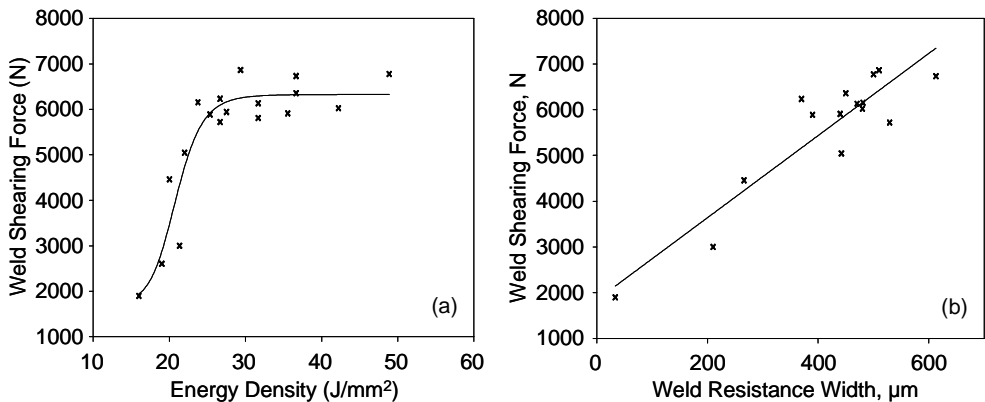


Fig 2.13: Variation in weld shearing force with (a) energy density, and (b) weld resistance length

In addition, from the plot showing the relationship between weld shearing force and energy density, it is observed that the weld shearing force increases with an

increase in energy density input up to a certain level. After that level, any additional increase in energy input has no or little contribution to weld shearing force as illustrated in Fig 2.13(a). This phenomenon can be attributed to the linear positive relationship existing between weld shearing force and resistance length as shown in Fig 2.13(b). These energy limiting criteria is used to select allowable working range of the energy density input and hence, to choose various combinations of process parameters to obtain a weld with desired quality.

### 2.3.2.2 Shrinkage

During shrinkage test, twelve specimens were welded in overlap configuration under the same welding condition described in section 2.2.3. Table 2.4 shows internal diameter and roundness of each specimen, which are measured before and after welding using 'Quickscope' system. The deviations in internal diameter and roundness are then determined from the measured data and recorded. As shown in Table 2.4, shrinkage in the laser welded joint is evident as internal diameter of inner shell reduces by an amount in the range of 0.34~0.91 µm due to laser welding under the set condition. Moreover, variation in roundness indicates that deformation occurs in the inner shell during welding. However, the extent of shrinkage and the behavior of deformation are found respectively unequal and nonuniform for the same energy density input.

Table 2.4: Shrinkage test results for inner shell

| Internal Diameter (mm) | | | Roundness (mm) | | |
|---|---|---|---|---|---|
| Before | After | ΔØ | Before | After | ΔO |
| 3.8434 | 3.84 | 0.0034 | 0.0025 | 0.0053 | -0.0028 |
| 3.8453 | 3.8387 | 0.0066 | 0.0030 | 0.0013 | 0.0017 |
| 3.8542 | 3.8469 | 0.0073 | 0.0053 | 0.0054 | -0.0001 |
| 3.8445 | 3.8374 | 0.0071 | 0.0031 | 0.0041 | -0.0010 |
| 3.842 | 3.8357 | 0.0063 | 0.0026 | 0.0011 | 0.0015 |
| 3.8428 | 3.838 | 0.0048 | 0.0006 | 0.0009 | -0.0003 |
| 3.8422 | 3.8367 | 0.0055 | 0.0042 | 0.0015 | 0.0027 |
| 3.8583 | 3.8492 | 0.0091 | 0.0023 | 0.0024 | -0.0001 |
| 3.8444 | 3.8398 | 0.0046 | 0.0033 | 0.0040 | -0.0007 |
| 3.8424 | 3.8363 | 0.0061 | 0.0039 | 0.0016 | 0.0023 |
| 3.8427 | 3.8357 | 0.0070 | 0.0037 | 0.0076 | -0.0039 |
| 3.8519 | 3.8482 | 0.0037 | 0.0017 | 0.0025 | -0.0008 |

### 2.3.3 Selection of allowable range of energy density input

From the discussion given in the preceding sections, it can be concluded that selecting the allowable range of energy density input is particularly important from various aspects:

i.  energy density correlates such welding parameters as laser power, welding speed and fiber diameter and express them from energy perspective;

ii.   energy density limits the maximum achievable weld resistance length and shearing force. Once the weld resistance length and shearing force reach their maximum limits, any additional energy input only increases the weld penetration depth; and

iii.   the lower limit of energy density determines the minimum weld resistance length and hence, provides the weld with minimum resisting force to shear across it. In fact, this is the minimum shearing force that would ensure proper functioning of the weld when it is subjected to real-life environment.
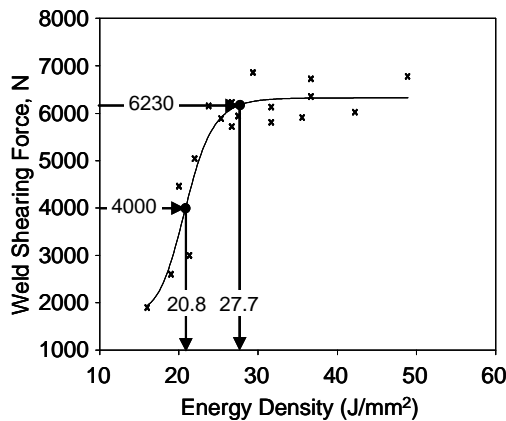


Fig 2.14: Relationship between weld shearing force and energy density input

Fig 2.14 recalls the concept shown in Fig 2.13(a) and underlines that the upper limit for shearing force and its corresponding energy density input can be selected as 6230N and 27.7 J/mm$^2$ respectively because any additional energy density input after this aforestated value has little contribution to increase in weld resistance length and hence, to shearing force of the weld. Moreover, any energy density input exceeding the upper limit will increase the loss of energy and cause problems associated with excessive energy input. Again, the lower limit is selected based on the minimum shearing force required for the weld to withstand the working load as mentioned in previous paragraph. This minimum resisting force required for this particular overlap joint to withstand internal pressure of the fuel injector is about 4000N and as shown in Fig 2.14; its corresponding energy density input is found 20.8 J/mm$^2$.   Therefore, the allowable range of energy density input for this particular overlap joint is 20.8-27.7 J/mm$^2$. More precisely, referring from equation (1), any combination of laser power, welding speed and fiber diameter producing the energy density within this range is to be chosen to fabricate a weld with desired quality and also to avoid the problems associated with an unreasonable energy density input.

## 2.4 CONCLUSIONS

For the laser system and the limits of laser parameters considered in this study, the following points can be concluded:

▪  Laser power and welding speed are the most significant factors affecting the weld bead geometry and weld shearing force. Except on the weld width, fiber diameter has little effect on weld bead parameters and shearing force.

37

However, combined with other parameters, it affects significantly on weld bead profile and shearing force.

- Weld resistance length increases with the increase in energy density input up to certain limit. After that limit, any additional increase in energy input only increases penetration depth and no longer affects weld resistance width. As a result, bead profile changes its shape from conical to cylindrical.
- Shearing force varies almost linearly with weld resistance and hence, shearing force up to a certain limit can be achieved for these operating conditions and weld configuration.
- Any combination of laser power, welding speed and fiber diameter producing the energy density within the range of 20.8-27.7 $J/mm^2$ is to be chosen to fabricate a weld with desired quality and also to avoid problems associated with an unreasonable energy density input.
- Both shrinkage and deformation occur during laser welding. However, amount of shrinkage and behavior of deformation are found unequal and nonuniform respectively for the repeated experiments.

## REFERENCES

1. Weichiat, C., Paul, A., Pal, M., 2009, CO2 laser welding of galvanized steel sheets using vent holes, Materials and Design, 30:245–251.
2. Lippold, J.C., Kotecki, D.J., 2005, Welding metallurgy and weldability of stainless steel, 1st ed., John Willey & Sons, NJ, USA, pp. 63-70.
3. Brooks, J.A., Garrison, W.M., 1999, Weld microstructure development and properties of precipitation-strengthened martensitic stainless steels, Welding Journal, 78(8): 280s -291s
4. Tzeng, Y.F., 2000, Parametric analysis of the pulsed Nd:YAG laser seam-welding process, Journal of Materials Processing Technology, 102: 40-47.
5. Hector Jr., L.G., Chen, Y.-L., Agarwal, S., Briant. C.L., 2004, Texture characterization of autogenous Nd: YAG laser welds in AA5182-O and AA6111-T4 aluminum alloys, Metall. and Mater. Trans A, 35A:3032-3038.
6. Al-kazzaz, H., Medraj, M., Cao, X., Jahazi, M., Xiao, M., 2005, Effects of welding speed on Nd:YAG laser weldability of ZE41A-T5 magnesium sand castings, Proceeding of 44th annual conference of metallurgists of CIM, Light Metals:137-149.
7. Huang, R. S., Kang, L., Ma, X., 2008, Microstructure and phase composition of a low-power YAG laser-MAG welded stainless steel joint, Journal of Materials Engineering and Performance, 17:928–935.
8. Liu, Q.S., Mahdavian, S.M., Aswin, D., Ding, S., 2009, Experimental study of temperature and clamping force during Nd:YAG laser butt welding, Optics & Laser Technology,41(6):794-799
9. Berzins, M., Childs, T.H.C., Ryder, G.R., 1996, The selective laser sintering of polycarbonate, Annals of the CIRP, 45(1):187–190.
10. Childs, T.H.C., Berzins, M., Ryder, G.R., Tontowi, A.E., 1999, Selective laser sintering of an amorphous polymer: simulations and experiments. Proc. IMechE, Part B: J. Engineering Manufacture, 213:333-349.
11. Jin, X., Li, L., 2004, An experimental study on the keyhole shapes in laser deep penetration welding, Optics and Lasers in Engineering, 41: 779–790.

12. Sudnik, W., Radaj, D., Breitschwerdt, S., Erofeew, W., 2000, Numerical simulation of weld pool geometry in laser beam welding, J. Phys. D: Appl. Phys. 33: 662–671.

13. Antony, J., 2003, Systematic Methodology for design of experiment: Design of Experiment for Engineers and Scientists, 1st Ed., Butterworth-Heinemann Publication, MA, USA, pp. 38-39.

# CHAPTER 3

## EXPERIMENTAL STUDY ON MICROSTRUCTURE EVOLUTION IN LASER WELDED MARTENSITIC STAINLESS STEELS

*This chapter investigates the effects of energy density input on development of microstructures at various weld zones. Energy-based local microhardness profiles are made and linked with the formation of the microstructures.*

*Microstructures in the fusion zone changes from cellular to columnar dendritic and equiaxed dendritic with increasing energy input. Variation in morphology of microstructures across the fusion zone is evident within the weld. A distinct region exists in between fusion and heat affected zones due to retention of the primary ferrite.*

*Heat-affected zone (HAZ) microstructures are different in inner and outer shells. In the inner shell zone, microstructures consist of both primary and secondary Cr-rich carbides in tempered martensite matrix, whereas microstructures are δ-ferrite stringers, tempered martensite, and sulfides in the outer shell zone.*

*Mean dendrite width decreases with increased energy density as the higher the energy density input the slower the cooling and the solidification rates.*

*Both the dendrite size and the partitioning trend of the ferrite- and austenite-promoting elements are correlated to energy density input and, with it, to the microhardness profile of the fusion zone.*

*Besides, local microhardness reaches its peak in the fusion zone and decreases gradually from fusion zone to base metal of the outer shell. In the inner shell, peak microhardness occurs in HAZ and the local softening relative to fusion zone and HAZ is visible at the fusion boundary.*

## 3.1 INTRODUCTION

Martensitic stainless steels are based on Fe-Cr-C ternary system, undergo an allotropic transformation, and form martensite from austenite under most thermo-mechanical processing situations and air-cooling, which is sufficiently rapid to cause substantial martensite. Normal weld cooling rates are also sufficiently rapid to grow weld metal and HAZ microstructures that are predominantly martensitic as described in [1]. Under normal welding conditions, the austenite present at elevated temperatures will transform to martensite. Many martensite stainless steels retain some high-temperature ferrite in the martensitic matrix, and its existence is a function of the balance of ferrite-promoting to austenite-promoting elements. At higher carbon contents, the austenite phase field expands, promoting fully martensitic structures. A high carbon contents result in a harder and more brittle martensite that is more susceptible to hydrogen-induced cracking and possible brittle fracture. Martensitic stainless steels are, therefore, considered being the most difficult of the five stainless steel families to weld as stated in [2]. However, martensitic AISI416 and AISI440FSe stainless steels with their chromium and carbon contents are resistant to different environments such as fresh water, steam, crude oil, gasoline, perspiration, and alcohol and have also considerable machinablilty characteristics. Their molybdenum content also provides the elevated-temperature strength through the formation of stable carbide as stated by [1]. Besides, the low-chromium and low-alloy element content make these martensitic stainless steels cheaper than the other types.

Because of their good creep; tensile and fatigue strength properties in combination with moderate corrosion and heat resistance; and low-cost benefit compared to austenitic stainless steels, both the use and welding of martensitic stainless steels have received considerable interest for engineering application. However, limited investigations have been carried out on weldability and service integrity of such materials. Ping et al. [3] investigated the microstructural evolution of 13Cr–8Ni–2.5Mo–2Al martensitic precipitation-hardened (PH) stainless steel. As the annealing temperature increased, the size and concentration of the precipitates increased concurrently while the number density decreased. The Mo and Cr segregation to the precipitate–matrix interface was detected. The decrease in the strength at higher temperature was due to the formation of larger carbides and reversion of austenite. Berretta et al. [4] studied pulsed Nd: YAG laser welding of AISI304 and AISI420 stainless steels in a butt joint configuration. The fillet geometry was not affected by variations in beam position. The weld zone revealed that a fine microstructure was formed, which was dendritic. When the laser beam was shifted in the direction of AISI420 steel, the structure contained martensite. The HAZ of AISI420 had the highest microhardness value for any incident laser beam position. Srinivasan [5] examined the effect of the laser beam mode on the microstructural evolution in AISI410 martensitic stainless steel welds. The weld metals consisted of ferrite and martensite in all the welds produced. The hardness variation within the Donut weld metal was much lower than that in the weld metals obtained with the Gaussian mode due to differences in the ferrite fraction. Kurt et al. [2] investigated the effect of austenitic interface layer on microstructure of AISI420 martensitic stainless steel joined by keyhole plasma transfer arc (PTA) welding process. The weld metal and HAZ were free of cracks. Austenitic interlayer caused to austenite phase and fine needle martensite in the fusion zone.

Moreover, austenitic interface layer increased the impact strength of the keyhole welding of the martensitic stainless steel. Rajeskhar et al. [6] studied the relative effects of various austenitizing temperatures on microstructure and mechanical properties of electron beam welds of AISI431 martensitic stainless steel. In the as-welded condition, the microstructure contained dendritic structure with ferrite network and retained austenite in a matrix of un-tempered martensite. Retained austenite content increased with the increase in the austenitizing temperature. Optimum mechanical properties, i.e., strength, hardness and toughness were observed when austenitized between 1050 °C and 1100 °C followed by tempering. Sharifitabar and Halvaee [7] conducted the resistance upset butt welding of austenitic (AISI304) to martensitic (AISI420) stainless steels to explore the effect of welding power on microstructure and mechanical properties of the joint. The results showed that an interlayer composed of 80% ferrite and 20% martensite formed at the joint interface. Different forms of austenite phase and chromium carbide ($Cr_{23}C_6$) were formed in the HAZ of austenitic stainless steel. The strength and hardness of the joint increased, and HAZ length decreased with the increase in welding power. Gualco et al. [8] investigated the effects of shielding gas, heat input, and post-weld heat treatment on the microstructural evolution of a modified AISI H13 martensitic tool steel. Welding with high heat input resulted in larger carbides precipitation, and a reduction in the retained austenite content and lower hardness.

### 3.1.1 Research objectives

As seen from the literatures, fusion zone (FZ) microstructures often contain martensitic dendritic structures with ferrite network, and development of carbides resulting in the highest local microhardness is common in HAZ. Change in weld macrostructures and corresponding mechanical properties under different applied conditions and combination of materials are marked. The size and shape of the weld microstructures seem to be sensitive to variation in materials and joining techniques, joint types, laser beam modes, selected process parameters, and heat input. However, comprehensive examination covering the change in microhardness via the development of microstructures and scientific contribution to laser welding making use of energy density, a process variable in the energy term, are rarely available in the literatures. This variable alone enables to provide the same effects as all the selected welding parameters like laser power, welding speed, and spot diameter together do. More work is required for better understanding its influence on the development of weld microstructure; the distribution of principal alloying elements; and hence, the change in local microhardness across the weld. This paper will, therefore, investigate the effects of energy density input on weld microstructure evolution, and change in local microhardness at various weld zones. Experimental studies will be focused on:

- examining the formation of and variation in weld microstructures with energy density input,
- illustrating the effects of process parameters and energy density input on mean dendritic width, and
- profiling the local microhardness at the inner and the outer shells of the overlap joint to show their variations with energy density input, and to relate this

change in local microhardness with the formation of microstructures and distribution of ferrite- and austenite-promoting elements.

## 3.2 EXPERIMENTAL

The martensitic AISI440FSe and AISI416 stainless steels used in automotive industries for making respectively inner and outer shells of a fuel injector are selected as base materials. Chemical composition of the base metals is reported in Table 3.1. The inside diameter of the outer shell and the outside diameter of inner shell are machined to 7.5±0.025 mm and 7.458±0.015 mm respectively to obtain a clearance between the parts when assembled. The assembled parts are then crimped applying a uniform force of 45 kN around the tip of the outer shell as a replication of the actual fabrication process. In order to remove the dirt from machining, a standard washing procedure stated in EN 1011-6:2005 is followed to clean, cool, and dry the specimens.

Table 3.1: Chemical composition of the base metals used

| Base Metal | Composition (in weight percent) | | | | | | |
|---|---|---|---|---|---|---|---|
| | C | Cr | Mn | Si | Mo | S | Se |
| AISI416 | 0.15 | 13.3 | 1.25 | 1.00 | 0.60 | 0.15 | - |
| AISI440FSe | 0.60-0.75 | 17.2 | 1.00 | 1.00 | 0.75 | - | 0.20 |

Specimens are welded circularly in an overlap joint configuration using a 1.1kW continuous wave Nd:YAG laser (Rofin DY011). Three controlled parameters are considered in this experiment: laser power (800-1100W), welding speed (4.5-7.5 m/min), and focus diameter (300-400 µm). The optical system consisted of 300µm and 400µm fibers along with two lenses of 200 mm focal length and collimating length are used to deliver the laser with a focal spot diameter of 300µm and 400µm respectively.
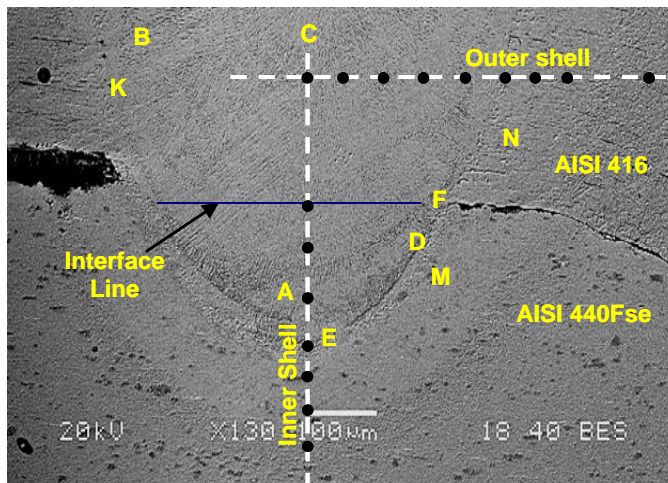


Fig. 3.1: SEM micrograph of the weld cross-section showing hardness profile and the selected points for microstructure evaluation

During the welding operation, the laser beam is focused normally onto the specimen surface. Argon is used as shielding gas with a constant flow rate of 29 l/min to protect weld surface from oxidation, and to suppress the generation of plasma during welding. Experimental conditions for microstructure evaluation and local microhardness profile are given in Table 3.2. After laser welding, no specific heat treatment is carried out. SEM micrograph indicating the points selected for microhardness profile and microstructure evaluations are shown in Fig. 3.1.

Table 3.2: Experimental conditions for microstructure evaluation and local microhardness profile

| Sample No # | Laser Power (W) | Welding Speed (m/min) | Fiber Diameter (µm) | Energy Density (J/mm$^2$) |
|---|---|---|---|---|
| 1 | 1100 | 6.0 | 300 | 36.7 |
| 2 | 800 | 4.5 | 300 | 35.6 |
| 3 | 800 | 6.0 | 300 | 26.7 |
| 4 | 950 | 6.0 | 400 | 23.8 |
| 5 | 800 | 6.0 | 400 | 20.0 |
| 6 | 950 | 7.5 | 400 | 19.0 |

| Constant Factors | | | | |
|---|---|---|---|---|
| Base material | : | Outer Shell<br>Inner Shell | : AISI 416<br>: AISI 440FSe | |
| Laser source | : | Nd:YAG Laser | | |
| Angle of Incidence (deg) | : | 90° (onto the surface) | | |
| Shielding gas | : | Type<br>Flow rate | : Argon<br>: 29 l/min | |

For the microstructural characterization, the six samples are selected, prepared, and etched with vilella's reagent (1g picric acid, 5 ml HCl, and 100 ml ethanol). The microstructure is characterized by optical microscope (Reichert MF-2) and scanning electron microscopy (SEM) (JEOL-JSM-5600 LV). Chemical composition of the weld material at different regions of the fusion area is determined through energy dispersive spectrometer (EDS) analysis. EDS spectra are also used to verify the development of primary and secondary carbides in HAZ of the inner shell. In addition, as shown in the Fig. 3.1, Vicker's microhardness profiles (50–100 g loading force) are carried out in both the vertical and the horizontal directions to characterize local hardness properties of the weld at inner and outer shells respectively.

## 3.3 RESULTS AND DISCUSSION

### 3.3.1 Weld microstructures and microhardness profiles

The results obtained from the investigation on microstructure evolution at various locations of the weld are described in the succeeding subsections.

### 3.3.1.1 Fusion zone

Microstructure evaluation in the FZ depends on the solidification behavior of the weld pool which resembles a minicast. The parameters determining the solidification microstructures in castings such as growth rate (R), temperature gradient (G), and undercooling (ΔT) can, therefore, be applied to welds. Fig. 3.2 represents a schematic view of the evolution of weld microstructure as a function of these three parameters [10].
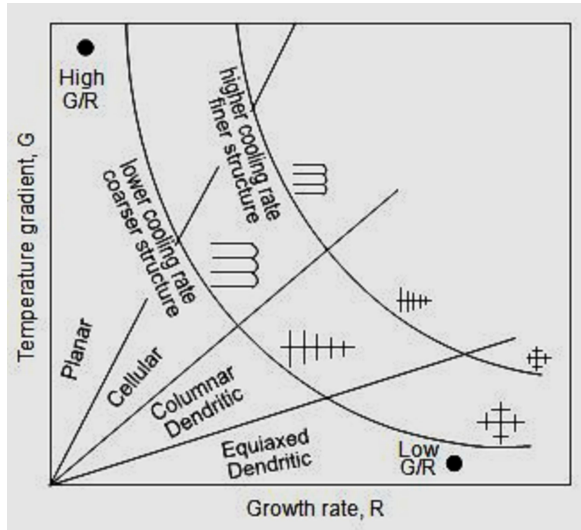


Fig. 3.2: Schematic view illustrating the effects of temperature gradient G and growth rate R on the morphology of solidification microstructure [10].



23.8 J/mm²          26.7 J/mm²          36.7 J/mm²

Energy density input
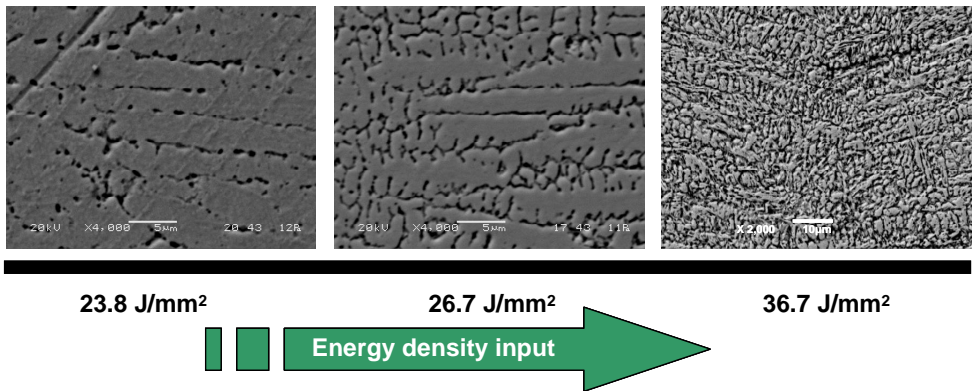
Fig. 3.3: SEM views illustrating the change in morphology of the solidification microstructure with energy density input in the fusion zone for S = 6.0 m/min

Fig. 3.3 shows the variation in solidification microstructures with increased energy density input in the fusion zone (point C in Fig. 3.1). The solidification structure is found to change from cellular to columnar and equiaxed dendrites. This phenomenon can be explained by the combined effect of temperature gradient (G)

and growth rate (R). The higher the energy density input under the same welding speed, the lower the temperature gradient [10]. This fact in turn reduces the ratio of temperature gradient to growth rate ($G/R$) and causes the formation of dendritic microstructure. Conversely, cellular solidification prevails at the lower energy density input.
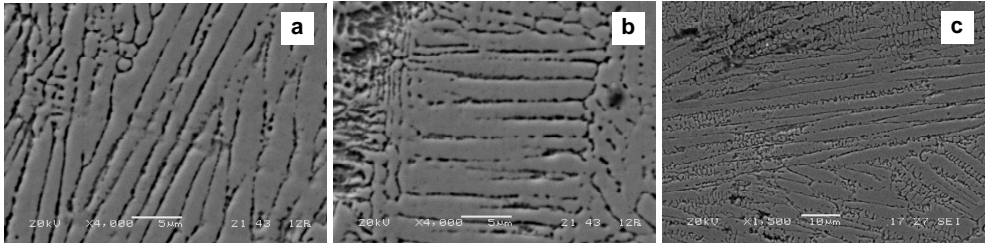


Fig. 3.4: SEM micrographs showing the variation in solidification mode across the fusion zone from fusion boundary at (a) inner shell and (b) outer shell to (c) near maximum pool temperature zone for energy density input of 26.7 J/mm$^2$.
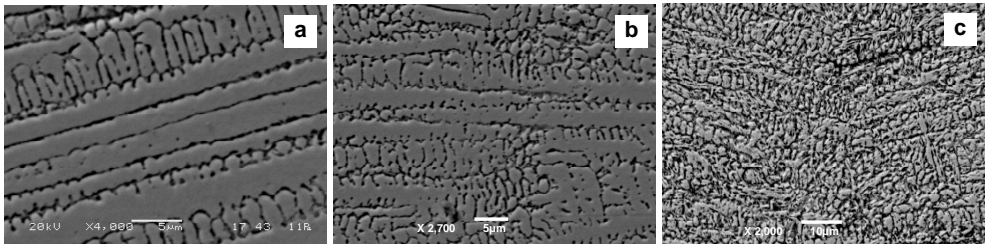


Fig. 3.5: Variation in solidification mode across the fusion zone from near fusion boundary at (a) inner shell and (b) outer shell to (c) near the maximum pool temperature zone for energy density input of 36.7 J/mm$^2$.

For a constant energy input, it is also found that the solidification microstructure changes across the same weld from the fusion boundary (points A and B in Fig. 3.1) toward the weld centerline (point C in Fig. 3.1). According to Nakagawa et al. [11], the growth rate R and the temperature gradient G are respectively minimum and maximum at the fusion boundary. As a result, the temperature gradient to growth ratio, $G/R$ decreases from fusion boundary line to the region of the maximum pool temperature on the centerline and causes the change in solidification modes from cellular to columnar dendritic (Fig. 3.4) or columnar to equiaxed dendritic (Fig. 3.5) across the fusion zone of the weld depending on the energy density input.

The effects of laser power and welding speed on the weld microstructure are also studied focusing on the dendrite arm width under different weld energy input and speed. Fig. 3.6 illustrates the variation in average dendrite width near the fusion zone boundary of the inner and the outer shells with energy density input. The dendritic structures widen as energy density input increases. This is because the higher the energy density input, the slower the solidification and cooling rates and thus the longer the time available for broadening of the dendrite structures. It can

also be noticed that the microstructures are relatively narrow in the outer shell than in the inner shell for the same energy density input. This is because the outer portion of welded structure solidifies comparatively at a faster rate than the inner portion.
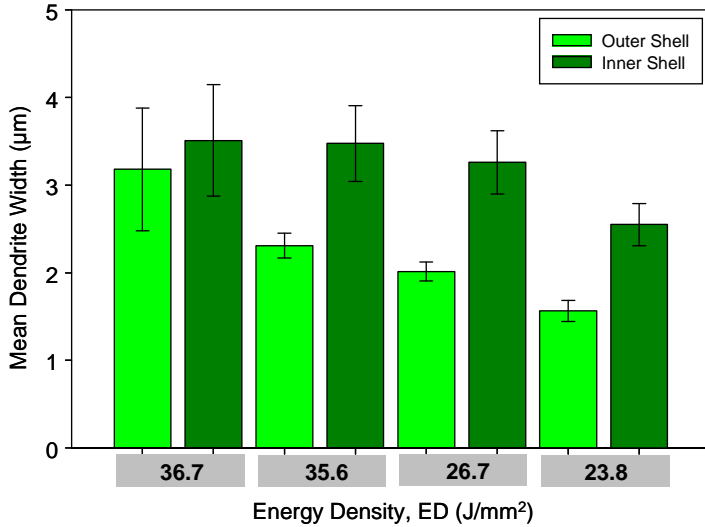


Fig. 3.6: Variation in mean dendrite width with energy density input near fusion zone boundary.
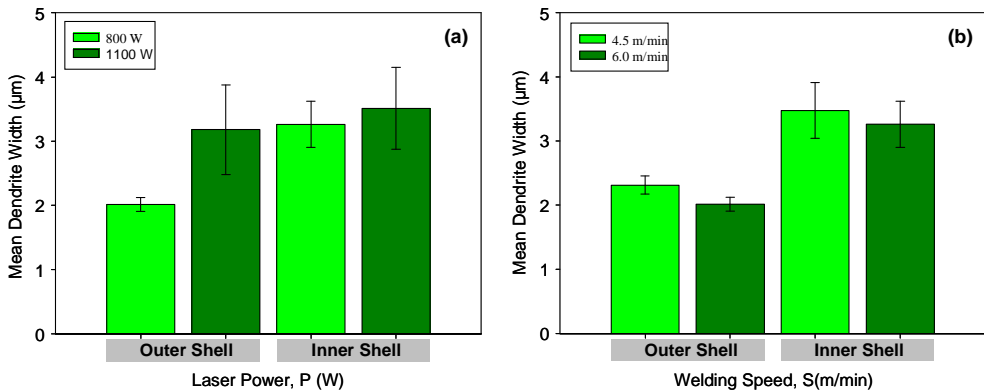


Fig. 3.7: Variation in mean dendrite width with (a) laser power for S= 6.0 m/min & F= 300 μm and (b) welding speed for P= 800 W & F= 300 μm

Besides, increase in the laser power under the same welding speed or decrease in the welding speed under the same laser power results in an increase in the energy density input to the weld. Hence, the dendrite structures become wider as a consequence of decreased cooling rate. These figures also reveal that variation in dendrite width between inner and outer shell is more pronounced for a welding speed than for a laser power.

The microstructure and phase composition across the weld has been studied using SEM. The fusion zone has the heterogeneous structure of martensite and delta

48

ferrite as shown in Figs 3.3, 3.11 and 3.15. The final weld microstructure is particularly influenced by the composition profile and elements partitioning along the weld. Table 3.3 summarizes the measured concentrations of ferrite-promoting elements (Cr, Mo) and austenite-promoting elements (Mn) across the weld. The fusion zone of the inner shell contains a higher percentage of Cr and Mo than the outer shell, which is in agreement with the presence of more delta ferrite in the inner portion of the weld. Furthermore, higher concentrations of austenite-promoting elements (Mn) are observed in the fusion zone of the outer shell for all samples. Partitioning trend is also correlated to the energy density input: for higher inputs, austenite-promoting element (Mn) has decreased while ferrite-promoting elements have increased.

Table 3.3: distribution of ferrite- and austenite-promoting elements over the weld fusion zone

| Energy Input (J/mm$^2$) | Weight percentage of alloying elements | | | | | | | |
| | Fusion zone | | | | | | Fusion zone boundary | |
| | Inner shell | | | Outer shell | | | Inner shell | |
| | Cr | Mo | Mn | Cr | Mo | Mn | Cr | Mo |
|---|---|---|---|---|---|---|---|---|
| 36.7 | 15.97 | 0.29 | 0.92 | 15.05 | 0.19 | 1.02 | 19.59 | 0.67 |
| 35.6 | 15.78 | 0.86 | 0.84 | 14.31 | 0.64 | 1.00 | 18.71 | 0.61 |
| 26.7 | 15.90 | 0.57 | - | 13.57 | 0.43 | 1.06 | 19.14 | 0.51 |
| 23.8 | 14.32 | 0.59 | 1.02 | 13.40 | 0.45 | 1.09 | 17.35 | 0.53 |
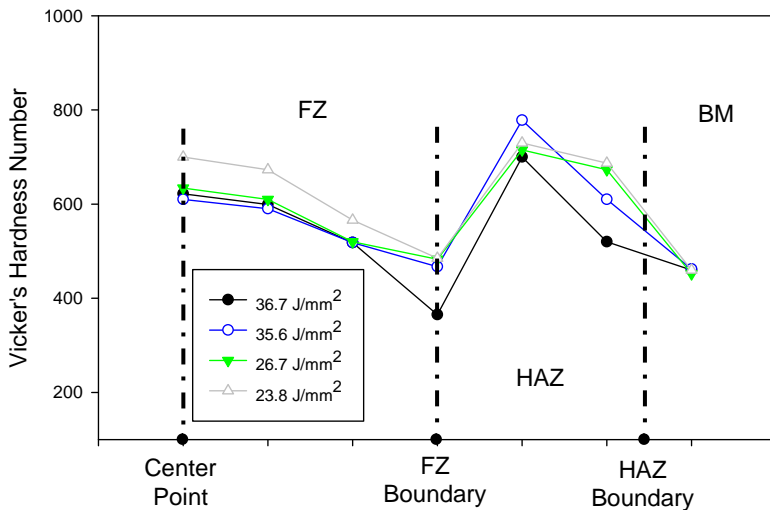


Fig. 3.8: Vicker's microhardness profile at the inner shell of the overlap joint for different energy density input.

Consequently, the microhardness profiles illustrated in Figs 3.8 and 3.9 show that vicker's local microhardness of the weld measured in the inner shell is lower than that in the outer shell for all the welds. The microhardness in both inner and outer shell fusion zones tends to decrease with increased energy density input. These

phenomena may result from the effect of energy input on both the cooling and the solidification rates, and are correlated to the redistribution patterns of segregated alloying elements.
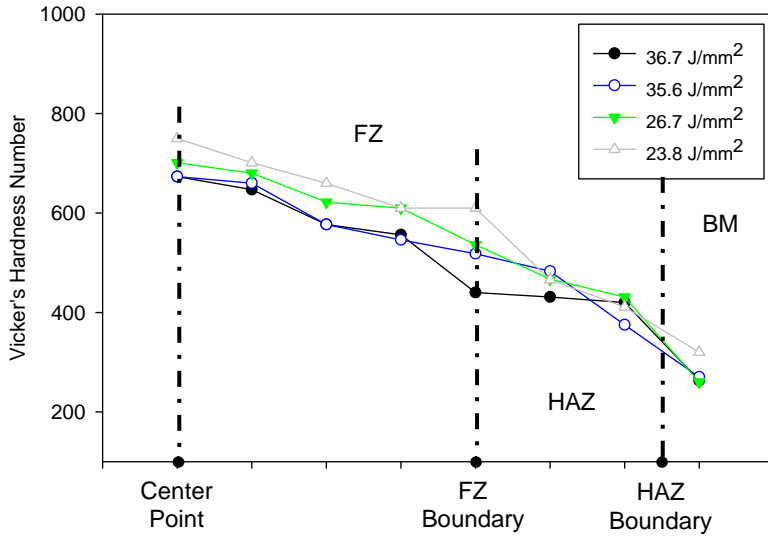


Fig. 3.9: Vicker's microhardness profile at the outer shell of the overlap joint at various energy density inputs.
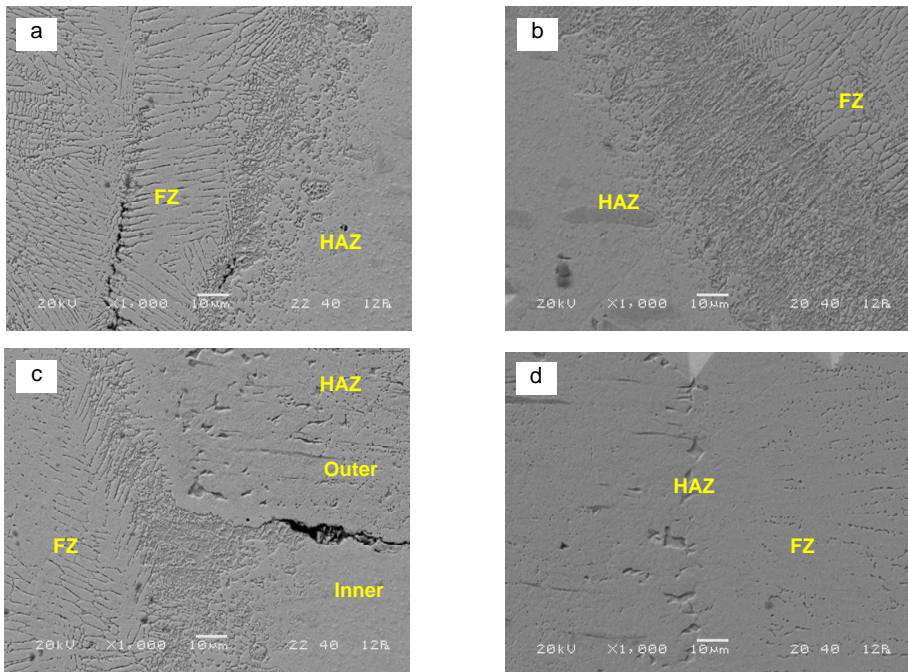


Fig. 3.10: Fusion boundary microstructure (a) at bottom and (b) at upper side of the inner part of the weld, (c) near the weld resistance section, and (d) at the outer portion of the weld for energy density input of 35.6 J/mm$^2$.

Besides, as shown in Fig. 3.10, a distinct boundary region exists between fusion and heat affected zones particularly in the inner shell. This is due to retention of primary ferrite that occurs during solidification of the weld and distribution of these retained primary ferrites in the martensitic structure. Wt% of the ferrite-promoting elements (particularly Cr and Mo) given in Table 3.3 also point out the presence of the larger amount of primary ferrite and the lower rate of dissolution of this ferrite at the fusion boundary as it cools through the austenite phase field on rapid cooling to room temperature. Distribution trend also shows a good agreement with energy density input and the associated change in microhardness. As illustrated in Fig 3.8, the presence of this retained primary ferrite promotes local softening relative to fusion zone and HAZ.

### 3.3.1.2 Heat-affected zone (HAZ)

Figs 3.11 (a)-(c) show the microstructures of base metal and HAZ (point M in Fig. 3.1) of the inner shell, which is pre-hardened and –tempered. Both microstructures contain partly spherodized primary carbide particles (indicated as X) in a tempered martensitic matrix. However, microstructures formed in HAZ are finer and contain secondary carbide particles (indicated as Y) too. Formation of these microstructures can be attributed to combined effects of dissolution of base metal carbide into the solution in the austenite due to sufficiently high temperature that prevails in HAZ and repeated hardening due to self-quenching, which occurs inherently during laser welding. As a result, inner shell HAZ becomes fully martensitic on cooling, and peak weld hardness occurs in this region as shown in Fig 3.8. The carbides formed in this HAZ are normally of $M_{23}C_6$ types, where the 'M' is predominantly of Cr and Fe. This fact is also verified using the EDS spectrums illustrated in Fig. 3.12.
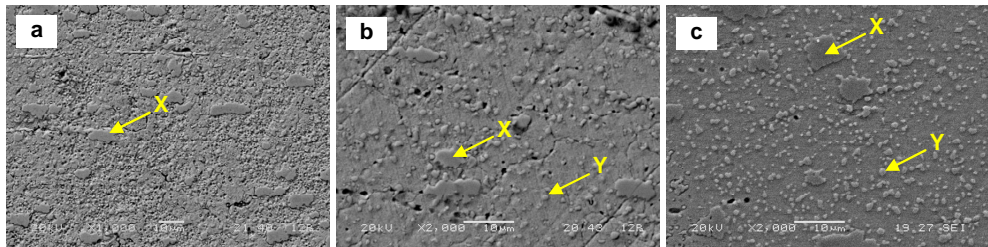


Fig. 3.11: Microstructure at (a) base metal in as-received condition, and HAZ of the inner shell for (b) ED = 26.7 J/mm$^2$ and (c) ED = 35.6 J/mm$^2$. [X: Primary Carbide, Y: Secondary Carbide]

Since the base metal of the outer shell contains the sufficient manganese, which combines much more readily with sulfur than does iron, stable manganese sulfide is present in both the base metal and the HAZ of the outer shell (indicated as Z in Fig. 3.13). Though manganese effect on mechanical properties is minimal and provides some solid solution strengthening, formation of this stable manganese sulfide effectively eliminates the hot shortness problem associated with the formation of low melting iron-sulfide eutectic constituents. From Figs 3.13(a)-(c), it can also be observed that base metal microstructures are predominantly untempered martensite with primary ferrite and carbides, whereas HAZ microstructures consist of δ-ferrite stringers (indicated as Z in Fig. 3.13), tempered

martensite and sulfides (point W in Fig. 3.1). The formation of these microstructures makes the heat affected zone locally harder than the base metal as shown in Fig 3.9.
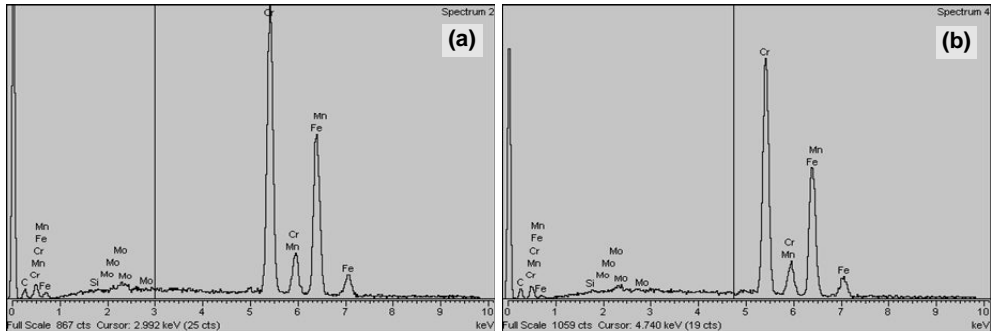


Fig. 3.12: EDS spectrum taken from spherodized particles of carbides indicated as (a) X and (b) Y in the Fig. 3.11.
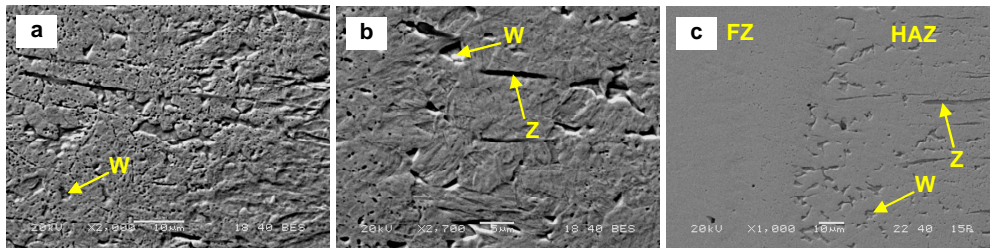


Fig. 3.13: Microstructure at (a) base metal in as-received condition, and HAZ of the outer shell for (b) ED = 23.8 J/mm$^2$ and (c) ED = 26.7 J/mm$^2$. [Z: Manganese Sulfide, W: δ-Ferrite]
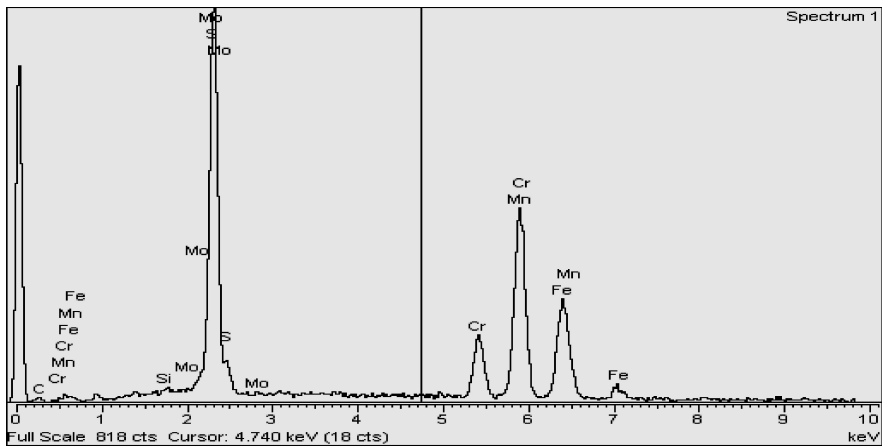


Fig. 3.14: EDS spectrum taken from manganese sulfide indicated as W in the Fig. 3.15.

## 3.4. CONCLUSIONS

In this study, martensitic AISI416 and AISI440FSe stainless steels are laser welded using different energy input in the range of 21.3 J/mm$^2$ to 48.9 J/mm$^2$. The effects of energy density input on the geometry of the weld seams and development of microstructures are examined. Following conclusions can be drawn from this work:

- The morphological change of the solidification microstructures in the fusion zone from cellular to columnar, and to equiaxed are marked with an increase in energy density input.
- The solidification mode varies from cellular to columnar dendritic or columnar to equiaxed dendritic across the fusion zone for the same energy density input.
- Mean dendrite width decreases with increased energy density as the higher the energy input slower down cooling and solidification rates.
- Microstructure forming across the fusion zone is a mixture of martensitic and delta ferrite. A distinct boundary region exists in between fusion and heat affected zone especially at the inner shell due to retention of the primary ferrite distributed in the martensitic structure. The presence of these ferrites promotes local softening relative to the adjacent fusion zone and HAZ.
- Both the dendrite size and the partitioning trend of the ferrite- and austenite-promoting elements are correlated to energy density input and, with it, to the microhardness profile of the fusion zone.
- HAZ microstructures are different in inner and outer shells. In the inner shell zone, microstructures consist of both primary and secondary Cr-rich carbides in tempered martensite matrix, whereas microstructures are δ-ferrite stringers, tempered martensite, and sulfides in the outer shell zone.
- In the outer shell, the microhardness reaches its peak in the fusion zone and decreases gradually from fusion zone to base metal. However, peak hardness occurs in HAZ and the primary ferrite promoting local softening relative to fusion zone and HAZ is evident at the fusion periphery of inner shell.

## REFERENCES

1. Lippold, J.C., Kotecki, D.J., 2005, Welding metallurgy and weldability of stainless steel, 1st ed. John Willey & Sons, NJ, USA, pp. 63–70.
2. Kurt, B., Orhan, N., Somunkiran, I., Kaya, M., 2009, The effect of austenitic interface layer on microstructure of AISI 420 martensitic stainless steel joined by keyhole PTA welding process, Materials and Design, 30:661–664.
3. Ping, D.H., Ohnuma, M., Hirakawa, Y., Kadoya, Y., Hono, K., 2005, Microstructural evolution in 13Cr–8Ni–2.5Mo–2Al martensitic precipitation-hardened stainless steel, Materials Science and Engineering A, 394:285–295
4. Berretta, J.R., de Rossi, W., Neves, M.D.M., de Almeida, I.A., Junior, N.D.V., 2007, Pulsed Nd:YAG laser welding of AISI 304 to AISI 420 stainless steels, Optics and Lasers in Engineering, 45:960–966.
5. Srinivasan, P.B., 2008, Effect of laser beam mode on the microstructural evolution in AISI 410 martensitic stainless steel welds, Lasers in Engineering, 18:351–359.
6. Rajasekhar, A., Reddy, G.M., Mohandas, T., Murti, V.S.R., 2009, Influence of austenitizing temperature on microstructure and mechanical properties of AISI

431 martensitic stainless steel electron beam welds, Materials and Design, 30:1612–1624.

7.  Sharifitabar, M., Halvaee, A., 2010, Resistance upset butt welding of austenitic to martensitic stainless steels, Materials and Design, 31(6):3044–3050.

8.  Gualco, A., Svoboda, H.G.,  Surian, E.S., de Vedia, L. A., 2010, Effect of welding procedure on wear behaviour of a modified martensitic tool steel hardfacing deposit, Materials and Design, 31:4165–4173

9.  Khan MMA, Romoli L, Fiaschi M, Dini G, Sarri F., 2010, Experimental investigation on laser beam welding of martensitic stainless steels in a constrained overlap joint configuration, Journal of Material Processing Technology,210:1340–53

10. Kou, S., 2002, Welding metallurgy, 2nd ed. John Willey & Sons Inc., NJ, USA, pp. 143- 169.

11. Nakagawa H, Matsuda F, Uehara T, Katayama S, Arata Y. A., 1979, New explanation for role of delta ferrite improving weld solidification crack susceptibility in austenitic stainless steel, Trans Jpn Weld Res Inst. 8:105–12.

# CHAPTER 4

## EXPERIMENTAL DESIGN APPROACH TO LASER WELDING PROCESS OPTIMIZATION FOR OVERLAP CONFIGURATION

*This chapter presents an experimental design approach to process parameter optimization for the laser welding of martensitic AISI416 and AISI440FSe stainless steels in a constrained overlap configuration.*

*To determine the optimal laser-welding parameters, general full factorial design (FFD) is used as a statistical design of experiment (DOE) technique to develop a set of mathematical models relating the welding parameters to each of the weld characteristics such as weld width, resistance length, penetration depth, and shearing force. The developed models are then validated both statistically and experimentally.*

*Both the numerical and the graphical optimization methods are used in this work by selecting the desired goals for each factor and response. The quality criteria set for the weld to determine optimal parameters are the minimization of weld width and the maximization of weld penetration depth, resistance length, and shearing force.*

*Whatever the optimization criteria, fiber diameter has to be around its lower limit to achieve a weld with narrower width, deeper penetration, longer resistance length and with it, the greater shearing force. Laser power and welding speed in the range 855–930 W and 4.50–4.65 m/min, respectively are identified as the optimal set of process parameters. However, the laser power and welding speed can be reduced to 800–840 W and increased to 4.75–5.37 m/min, respectively, to obtain stronger and better welds. The graphical optimization results allows quicker search for the optimal settings for laser welding.*

**4.1 INTRODUCTION**

Laser welding is a high-energy-density welding process and is well known for its deep penetration, high speed, small heat-affected zone, fine welding seam quality, low heat input per unit volume, and fiber optic beam delivery as mentioned [1]. As a result, it has been increasingly utilized in industrial sectors such as automotive, marine, electronics, etc. Nowadays, in automotive industries, the fabrication of modern fuel injectors for gasoline, diesel, and gaseous fuels uses laser welding to improve quality and maximize production throughput. Of the lasers used in automotive industries to weld small and heat sensitive complex parts of a fuel injector, continuous wave (CW) Nd:YAG lasers perform the best for welding, because of its short time cycle and the metallurgy of the stainless steels used. More recently, research has shown that welding input parameters play a very significant role in determining the quality and shape of the laser weld bead as the combination of these parameters controls the heat input. However, it is well known that, whatever the welding method, fusion welding generally involves heating the two joined parts, which can cause modification of material characteristics. In other words, the properties of the area around the weld bead (HAZ) would be affected with variation in hardness, reduction of tensile strength, toughness, etc. The weld quality is, therefore, defined in terms of properties such as weld-bead geometry, mechanical properties, and distortion. Generally, all welding processes are used with the aim of obtaining a welded joint with desired weld-bead parameters, excellent mechanical properties with minimum distortion. In this context, for a good weld quality the combination of output power, welding speed, focal position, shielding gas and position accuracy should be correctly selected as stated by Huang et al. [2].

The main challenge for the manufacturer is how to choose the process input parameters that would produce an excellent welded joint with the required weld-bead geometry and weld quality with minimal detrimental residual stresses and distortion. Conventionally, selecting the weld input parameters for new welded products to produce a welded joint with the required specifications is a time consuming trial and error development effort with weld input parameters chosen by the skill of the engineer or machine operator. Then the weld is inspected to determine whether it meets the specification or not. Eventually the chosen parameters would produce a welded joint close to the required specification. Also, what often not considered or achieved are optimized welding parameters combinations. In other words, there are often alternative ideal welding parameters combinations that can be used if they can only be determined. To predict the welding parameters accurately without consuming time, materials and labor effort, various optimization methods are applied to define the desired output variables through developing mathematical models as reported by Benyounis and Olabi [3]. In the last two decades, the use of factorial design of experiment (DOE) has grown rapidly and a variety of industries have employed this technique to improve products or manufacturing processes as described [4]. It is a powerful and effective technique to solve challenging quality problems. In practice, the factorial design of experiment technique has been used quite successfully in several industrial applications as in designing electrical/mechanical components or optimizing various manufacturing processes as stated [5].

Douglass and Wu [6] performed an experimental investigation to assess weldability of polyolefin elastomers (POEs) and thermoplastic polyolefins (TPO) using through-transmission laser welding (TTLW). Two POEs of differing ultimate tensile strengths were welded to TPO in a lap joint configuration using a 100W Yb fiber laser. A three-factor (laser power, travel speed, and welding pressure) two-level full factorial design of experiments was used to optimize the welding process. The power was varied from 10 to 30 W, speeds from 10 to 40 mm/s and pressure from 20 to 50 psi. It was found that the lap shear strength was proportional to the laser power and welding pressure, and inversely proportional to speed. It was concluded that these materials indeed possessed good laser weldability. Koganti et al. [7] also applied a full factorial design to determine the optimum weld MIG process parameters for non-treatable 5754 aluminum alloys. The effects of weld process parameters on the lap joint failure load (tensile-shearing strength) and weld penetration were investigated. The process parameters were power input (torch speed, voltage, current, and wire feed-rate), pulse frequency and gas flow rate. The joint strengths and weld penetration were measured for various operating ranges of weld factors. It was indicated that power input and gas flow rate were the two significant factors affecting the lap shearing load to failure and weld penetration. Also, it was reported that the lower the power input, the lower the shearing load to failure and depth of penetration and vice versa. The optimum factor settings for higher joint strength were the high power input and the high gas flow rate. As a continuation of their previous work, Balasubramanian and Guha [8] developed mathematical models using factorial design of experiment to predict the fatigue life of shielded metal arc welding SMAW and FCAW cruciform joints failing from root and toe regions. Using the developed models, the fatigue life of SMAW and FCAW cruciform joint could be predicted at a 95% confidence level. However, the validity of the models is limited to the factors domain. It was found that the factorial experimentation technique design of experiment is more economical for predicting the effect of various factors on fatigue life through conducting a minimum number of experiments. Cicala et al. [9] followed the factorial design approach to optimize the T-joint properties in laser welding of Al–Mg–Si alloy. T-joint welding was carried out using two CW laser heads. With the optimum parameters, a good tensile strength was achieved. Simultaneous or sequential welding leads to different weld depths, but with similar values for tensile strength within the optimum parameter range. A cross-section of the weld showed a V-shaped seam that gave the highest tensile strength for the different laser configurations. From the results of the factorial design, a second degree polynomial model was also built to estimate the average tensile strength per mm of weld as a function of welding speed and wire volume deposited per mm of weld in the experimental field. In 2008, Kim et al. [10] examined the relationship between weldability and the process parameters of laser beam–arc distance, welding current and welding speed using a full factorial experimental design. In their study, laser–TIG hybrid welding was applied to the lap welding of zinc-coated steel without a gap. Weld quality was evaluated using the weight of the spatter, as porosity formation was a major weld defect in the lap welding of zinc-coated steel sheets. It was found that the weld quality increased with the increased laser beam–arc distance and welding current, and decreased as welding speed increased. In the same year, Datta et al. [11] evaluated an optimal parameter combination to obtain acceptable quality characteristics of bead geometry in submerged arc bead-on-plate weldment on mild steel plates. The SAW

process was designed to consume fused flux/slag in the mixture of fresh flux using the concept of 'waste to wealth'. Their work was initiated to develop mathematical models showing different bead geometry parameters as a function of process variables. Hence, optimization was performed to determine the maximum amount of slag–flux mixture that could be used without sacrificing any positive effect on bead geometry compared to the conventional SAW process, which consumes fresh flux only. Experiments were conducted using welding current, slag-mix percentage and flux basicity index as process parameters and each of the parameters was varied at four different levels. Using $4^3$ full factorial designs, without replication, the welding was carried out on mild steel plates to obtain bead-on-plate welds. After measuring bead width, depth of penetration and reinforcement; based on simple assumptions on the shape of bead geometry, other relevant bead geometry parameters such as percentage dilution, weld penetration shape factor, weld reinforcement form factor, area of penetration, area of reinforcement and total bead cross-sectional area were calculated. All these data were, finally, utilized to develop mathematical models between predictors and responses. Benyounis et al. [12] also investigated the parametric effects on the tensile strength and impact strength along with the joint-operating cost of $CO_2$ laser-welded butt joints made of AISI304. In their investigative study, three-factor-five-level full factorial central composite design (CCD) technique was applied to design the experiments and also to establish the relationships between the laser welding process parameters (laser power, welding speed, and focal position) and each of the three responses (i.e. tensile strength, impact strength, and operating cost). The developed mathematical models were tested for adequacy and used to optimize the welding conditions in order to increase the productivity and minimize the total operating cost. Sarsilmaz and Caydas [13] experimentally investigated the effect of friction–stir welding (FSW) parameters such as spindle rotational speed, traverse speed, and stirrer geometry on mechanical properties of AA 1050/AA 5083 alloy couples conducting the full-factorial experimental design. Ultimate tensile strength (UTS) and hardness of welded joints were determined as response factors. Analysis of variance (ANOVA) and main effect plot were used to determine the significant parameters and set the optimal level for each parameter. A linear regression equation was derived to predict each output characteristic. The experimental and predicted values were in a good agreement with a $R^2$ of 0.82 and 0.93 for UTS and hardness, respectively.

### 4.1.1 Research objectives

As seen from the literatures, factorial design technique is effective for various welding technologies in investigating the effect of process parameters on weld quality in terms of weld bead geometry and mechanical properties. Again, the effect of influential welding parameters depends largely on several factors such as material type, joint type, and welding process involved. Therefore, the research has to be carried out separately for each of new component, material, and welding process. Moreover, various mathematical models developed by using this technique are found fairly accurate in predicting weld-bead geometry and mechanical properties and optimizing the welding conditions. Besides, no attempt has been made so far to optimize the process parameter of laser welding of AISI416 and AISI440FSe stainless steels in a constrained overlap configuration

though the parametric effects on the aforestated type of laser weld have already been discussed elsewhere [14]. This study is, therefore, focused on

- Application of full factorial design approach to develop mathematical models for the above mentioned martensitic stainless steels to predict and optimize the following process responses:
  - ✓ Weld-bead geometry e.g. weld width, penetration depth, resistance length and
  - ✓ weld mechanical property e.g. shearing force
- Graphical presentation of the developed models to show the effect of significant model terms and their interactions on the selected responses.
- Use of analysis of variances (ANOVA) and other statistical measures to test adequacy of the developed models and examine each term in the developed models using statistical significance tools. Conducting the experiment to validate of the developed models as well.
- Determination of the optimal range of input welding parameters (laser power, welding speed, and spot diameter), using the developed models with numerical optimization and graphical optimization, to minimize the weld width and maximize the weld penetration depth, resistance length, and shearing force.

## 4.2 MATERIAL AND METHODS

### 4.2.1 Materials

The martensitic AISI 440FSe and AISI 416 stainless steels normally used in automotive industries for making respectively inner and outer shells of a fuel injector are selected as base metals for the constrained overlap weld fabrication. The chemical compositions of the base metals and weld bead characteristics are shown in Table 4.1 and Fig 4.1 respectively. The inside diameter of outer shell and the outside diameter of inner shell are machined to Ø7.5±0.025mm and Ø7.458±0.015mm respectively. These two parts are first assembled together so that there is a clearance between them and then crimped applying a uniform force of 12kN around the tip of outer shell, which is a replication of actual fabrication process.
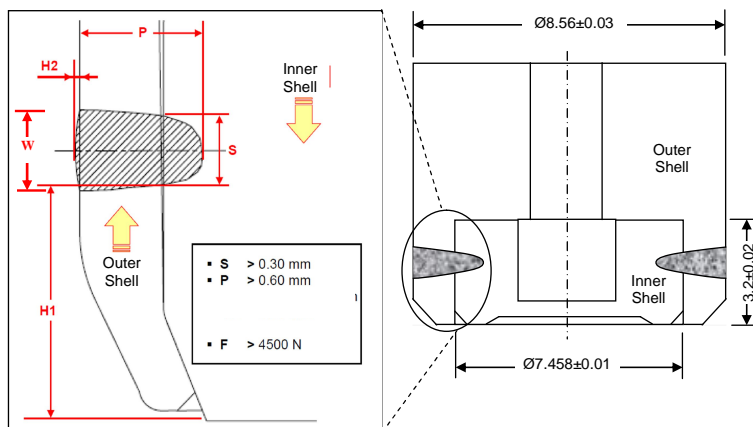


Fig 4.1: Characterization of welding cross-section (W: Weld width, P: Penetration depth, S: Resistance length) and their prerequisite values.

Table 4.1: Chemical compositions of base metals of the weld

| Base Metals | Chemical Compositions (%Wt) | | | | | |
|---|---|---|---|---|---|---|
| | C | Cr | Mn | Mo | Si | S |
| AISI440FSe | 0.60 | 17.0 | 1.00 | 0.75 | 1.0 | - |
| AISI416 | 0.15 | 13.0 | 1.25 | 0.60 | 1.0 | 0.15 (min) |

## 4.2.2 Experimental design

Welding experiments are planned based on statistical factorial experimental design. The statistical software Design-Expert V7 was used to create the design matrix and analyze the experimental data. Laser power, (P), welding speed (S), and fiber diameter (F) are considered as laser welding input factors. Each factor and its working range are selected based on experts' opinions and industrially recommended laser welding parameters used in automotive industries. Primary input factors, their corresponding levels and response factors considered are given in the Table 4.2.

Table 4.2: Experimental Conditions and Response Factors

| Process Factors | Symbols | Levels of Each Factor | | |
|---|---|---|---|---|
| | | 1 | 2 | 3 |
| Laser power (W) | P | 800 | 950 | 1100 |
| Welding speed (m/min) | S | 4.5 | 6.0 | 7.5 |
| Fiber Diameter (µm) | F | 300 | - | 400 |
| Constant Factors | | | | |
| Base material | : | Outer Shell : AISI 416<br>Inner Shell : AISI 440 FSe | | |
| Laser source | : | Nd:YAG Laser | | |
| Angle of Incidence (deg) | : | 90° (onto the surface) | | |
| Shielding gas | : | Type : Argon<br>Flow rate : 29 l/min | | |
| Response Factors | | | | |
| Weld bead characteristics | : | Weld Width (W), Resistance Length ($S_L$), and Penetration Depth ($D_p$) | | |
| Mechanical properties | : | Weld Shearing Force ($F_s$) | | |

General Full Factorial Design (FFD) is used as a statistical design of experiment (DOE) technique to develop mathematical models relating the welding parameters to each of the four output responses of the weld (weld width, resistance length, penetration depth, and shearing force). The adequacies of the models developed and their significant linear and interaction model terms are measured by analyzing variance and other adequacy measures. Finally, these mathematical models are used to determine the optimal settings of welding parameters to ensure the desired weld quality. In this study, the quality criteria defined for the weld to determine the optimal settings of welding parameters are the minimization of weld width, and the maximization of weld penetration depth, resistance length, and shearing force.

### 4.2.3 Experimental work

Welding tests were carried out according to the design matrix in a random order to avoid any systematic error in the experiment. Specimens were welded circularly in an overlap joint configuration using a continuous wave Nd:YAG laser (1.1 kW, Rofin DY011). During experimentation, laser power and welding speed are varied in the range of 800-1100 W and 4.5-7.5 m/min respectively. The optical system consisted of 300 µm and 400 µm fibers with the lenses of 200 mm focal length and collimating length delivered laser at focal spot diameters of 300 µm and 400 µm respectively. As a consequence, the corresponding energy density inputs on the focused area are in the range of 16.0-48.9 J/mm$^2$. During welding operation, the laser was focused normally onto the specimen surface and argon was supplied as a shielding gas at a constant flow rate of 29 l/min to protect heated surface from oxidation. A standard washing procedure practised in the automotive industries is followed to clean, cool and dry the specimens. No special heat treatment is carried out after welding. Photographic views of the experimental set-up for laser welding and push out test have been shown in Figs 4.2(a) and (b) respectively.
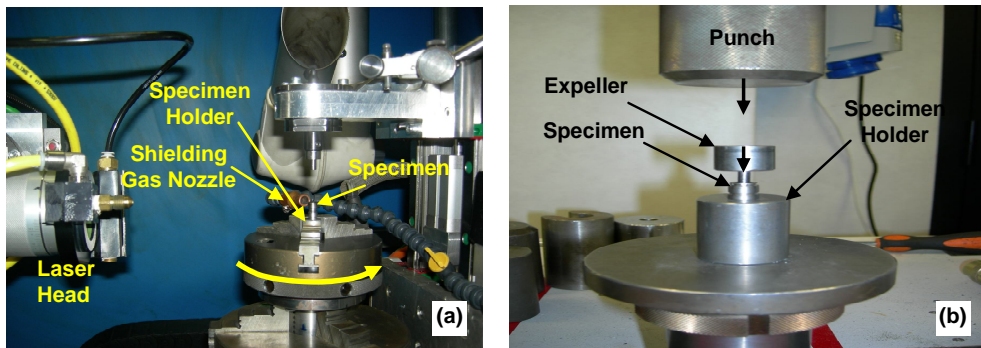


Fig 4.2: Photographic views of the experimental set-up for (a) laser welding and (b) shearing test

### 4.2.4 Mechanical characterization

After welding, specimens are first visually inspected and then sectioned axially to obtain transverse sections of the weld bead under various welding conditions. Software, Leica IM500, incorporated with an optical microscope (Leica MZ125) is used to measure various characteristics of the weld bead. The average value of each of measured response factors is determined and recorded for further analyses. Besides, push out tests are accomplished at room temperature (22 °C) using Instron push out calibrated press (model 3367) to determine the shearing load to failure of the welds fabricated under various conditions. During shearing test, specimens are set on a specimen holder or vice and pushed axially by a specially designed expeller so that the specimen fails due to shear across the weld as shown in Fig 4.2(b). Table 4.3 shows the design matrix with actual factors and measured mean responses.

Table 4.3: Design matrix with actual factors and measured mean responses

| Process Factors | | | Response Factors | | | |
|---|---|---|---|---|---|---|
| P (W) | S (m/min) | F (mm) | W (µm) | $D_p$ (µm) | $S_L$ (µm) | $F_s$ (N) |
| 800 | 4.50 | 300 | 490 | 960 | 440 | 5910 |
| 950 | 4.50 | 300 | 490 | 1290 | 480 | 6022 |
| 1100 | 4.50 | 300 | 580 | 1610 | 500 | 6775 |
| 800 | 6.00 | 300 | 530 | 710 | 370 | 6233 |
| 950 | 6.00 | 300 | 520 | 950 | 470 | 6129 |
| 1100 | 6.00 | 300 | 510 | 1180 | 450 | 6355 |
| 800 | 7.50 | 300 | 530 | 560 | 210 | 2999 |
| 950 | 7.50 | 300 | 590 | 730 | 390 | 5886 |
| 1100 | 7.50 | 300 | 590 | 880 | 510 | 6861 |
| 800 | 4.50 | 400 | 572 | 790 | 529 | 5722 |
| 950 | 4.50 | 400 | 612 | 1043 | 586 | 5809 |
| 1100 | 4.50 | 400 | 638 | 1307 | 613 | 6730 |
| 800 | 6.00 | 400 | 622 | 577 | 266 | 4457 |
| 950 | 6.00 | 400 | 699 | 727 | 481 | 6154 |
| 1100 | 6.00 | 400 | 771 | 920 | 588 | 5942 |
| 800 | 7.50 | 400 | 600 | 492 | 33 | 1897 |
| 950 | 7.50 | 400 | 721 | 580 | 273 | 2602 |
| 1100 | 7.50 | 400 | 732 | 749 | 442 | 5044 |



Fig. 4.3: Flow chart of optimization step

62

### 4.2.5 Optimization procedure

The optimization part in Design-Expert software V7 searches for a combination of factor levels that simultaneously satisfy the requirements placed (i.e. optimization criteria) on each of the responses and process input factors (i.e. multiple-response optimization). Numerical and graphical optimization methods are used in this work by selecting the desired goals for each factor and response. As mentioned before, the numerical optimization process involves combining the goals into an overall desirability function (D). The numerical optimization feature in the design-expert package finds one point or more in the factors domain that maximizes this objective function. In a graphical optimization with multiple responses, the software defines regions where requirements simultaneously meet the proposed criteria. Also, superimposing or overlaying critical response contours can be defined on a contour plot. Then, a visual search for the best compromise becomes possible. The graphical optimization displays the area of feasible response values in the factor space. Regions that fit the optimization criteria are colored as stated [15]. Fig 4.3 shows flow chart of the optimization steps [12].

## 4.3 RESULTS AND DISCUSSION

### 4.3.1 Development of mathematical models

At this stage, the fit summary in the design-expert software is used to select the models that best describe the response factors. The fit summary includes sequential model sum squares to select the highest order polynomial where additional terms are significant and the model is not aliased. In addition, model summary statistics of the fit summary focuses on the model that maximizes adjusted R-squared and predicted R-squared values. The sequential F-test is carried out using the same statistical software package to check if the regression model is significant and find out the significant model terms of the developed models as well. The step-wise regression method is also applied to eliminate the insignificant model terms automatically.

### 4.3.1.1 Response model selection

Suitable response models for the response factors are selected based on the fit summaries. From fit summary output of the measured responses shown in Tables 4.5 - 4.11, it is evident that linear model is statistically significant for the weld width and can, therefore, be used for further analysis. While for the other responses e.g. weld penetration depth, weld resistance width and shearing force, two-factor interaction (2FI) models are statistically recommended for further analyses.

Table 4.4: Sequential model sum of squares for weld width model

| Source | Sum of Squares | df | Mean Square | F Value | p-value Prob > F | |
|---|---|---|---|---|---|---|
| Mean | 6.479E+006 | 1 | 6.479E+006 | | | |
| Linear | 1.032E+005 | 3 | 34388.29 | 23.85 | < 0.0001 | Suggested |
| 2FI | 4628.36 | 3 | 1542.79 | 1.09 | 0.3935 | |
| Quadratic | 969.78 | 2 | 484.89 | 0.30 | 0.7485 | Aliased |

| Cubic | 10552.88 | 5 | 2110.58 | 2.09 | 0.2469 | Aliased |
|---|---|---|---|---|---|---|
| Residual | 4031.66 | 4 | 1007.92 | | | |
| Total | 6.603E+006 | 18 | 3.668E+005 | | | |

Table 4.5: Model summary statistics for weld width model

| Source | Std. Dev. | $R^2$ | Adj. $R^2$ | Pred. $R^2$ | PRESS | |
|---|---|---|---|---|---|---|
| Linear | 37.97 | 0.8364 | 0.8013 | 0.7309 | 33197.23 | Suggested |
| 2FI | 37.60 | 0.8739 | 0.8051 | 0.5743 | 52514.53 | |
| Quadratic | 40.26 | 0.8818 | 0.7767 | 0.4482 | 68057.36 | Aliased |
| Cubic | 31.75 | 0.9673 | 0.8611 | -0.1050 | 1.363E+005 | Aliased |

Table 4.6: Sequential model sum of squares for weld penetration depth model

| Source | Sum of Squares | df | Mean Square | F Value | p-value Prob > F | |
|---|---|---|---|---|---|---|
| Mean | 1.432E+007 | 1 | 1.432E+007 | | | |
| Linear | 1.457E+006 | 3 | 4.855E+005 | 77.15 | < 0.0001 | |
| 2FI | 63735.88 | 3 | 21245.29 | 9.59 | 0.0021 | Suggested |
| Quadratic | 21029.47 | 2 | 10514.74 | 28.35 | 0.0001 | Aliased |
| Cubic | 2930.23 | 5 | 586.05 | 5.74 | 0.0576 | Aliased |
| Residual | 408.15 | 4 | 102.04 | | | |
| Total | 1.586E+007 | 18 | 8.814E+005 | | | |

Table 4.7: Model summary statistics for weld penetration depth model

| Source | Std. Dev. | $R^2$ | Adj. $R^2$ | Pred. $R^2$ | PRESS | |
|---|---|---|---|---|---|---|
| Linear | 79.33 | 0.9430 | 0.9307 | 0.8974 | 1.585E+005 | |
| 2FI | 47.07 | 0.9842 | 0.9756 | 0.9559 | 68167.91 | Suggested |
| Quadratic | 19.26 | 0.9978 | 0.9959 | 0.9893 | 16565.79 | Aliased |
| Cubic | 10.10 | 0.9997 | 0.9989 | 0.9906 | 14486.37 | Aliased |

Table 4.8: Sequential model sum of squares for weld resistance length model

| Source | Sum of Squares | df | Mean Square | F Value | p-value Prob > F | |
|---|---|---|---|---|---|---|
| Mean | 3.235E+006 | 1 | 3.235E+006 | | | |
| Linear | 2.699E+005 | 3 | 89952.05 | 12.21 | 0.0003 | |
| 2FI | 88819.20 | 3 | 29606.40 | 22.70 | < 0.0001 | Suggested |
| Quadratic | 6286.94 | 2 | 3143.47 | 3.51 | 0.0746 | Aliased |
| Cubic | 1831.13 | 5 | 366.23 | 0.24 | 0.9279 | Aliased |
| Residual | 6228.19 | 4 | 1557.05 | | | |
| Total | 3.608E+006 | 18 | 2.005E+005 | | | |

Table 4.9: Model summary statistics for weld resistance length model

| Source | Std. Dev. | $R^2$ | Adj. $R^2$ | Pred. $R^2$ | PRESS | |
|---|---|---|---|---|---|---|
| Linear | 85.84 | 0.7234 | 0.6642 | 0.5075 | 1.837E+005 | |
| 2FI | 36.11 | 0.9615 | 0.9406 | 0.8934 | 39781.76 | Suggested |
| Quadratic | 29.92 | 0.9784 | 0.9592 | 0.9036 | 35941.38 | Aliased |
| Cubic | 39.46 | 0.9833 | 0.9290 | 0.4591 | 2.018E+005 | Aliased |

Table 4.10: Sequential model sum of squares for weld shearing force model

| Source | Sum of Squares | df | Mean Square | F Value | p-value Prob > F | |
|---|---|---|---|---|---|---|
| Mean | 5.284E+008 | 1 | 5.284E+008 | | | |
| Linear | 2.485E+007 | 3 | 8.284E+006 | 9.69 | 0.0010 | |
| 2FI | 6.113E+006 | 3 | 2.038E+006 | 3.82 | 0.0424 | Suggested |
| Quadratic | 1.908E+006 | 2 | 9.542E+005 | 2.17 | 0.1699 | Aliased |
| Cubic | 1.765E+006 | 5 | 3.529E+005 | 0.64 | 0.6828 | Aliased |
| Residual | 2.189E+006 | 4 | 5.473E+005 | | | |
| Total | 5.652E+008 | 18 | 3.140E+007 | | | |

Table 4.11: Model summary statistics for weld shearing force model

| Source | Std. Dev. | $R^2$ | Adj. $R^2$ | Pred. $R^2$ | PRESS | |
|---|---|---|---|---|---|---|
| Linear | 924.85 | 0.6748 | 0.6052 | 0.4581 | 1.996E+007 | |
| 2FI | 730.02 | 0.8408 | 0.7540 | 0.6077 | 1.445E+007 | Suggested |
| Quadratic | 662.81 | 0.8926 | 0.7972 | 0.5833 | 1.535E+007 | Aliased |
| Cubic | 739.81 | 0.9406 | 0.7474 | -0.4923 | 5.496E+007 | Aliased |

**4.3.1.2 Analysis of variance (ANOVA)**

The test for significance of the regression models and the test for significance on individual model coefficients are performed using the same statistical package. By selecting the step-wise regression method that eliminates the insignificant model terms automatically, the resulting ANOVA Tables 4.12-4.15 for the selected models summarize the analysis of variance of each response and illustrate its significant model terms as well. The aforestated tables demonstrate that calculated Fisher's 'Model-F' and 'Model-P' values are respectively 23.85 & <0.0001 for weld width linear model; 114.39 & <0.0001 for weld penetration depth 2FI model; 45.83 & <0.0001 for weld resistance length 2FI model; and 12.54 & 0.0002 for weld shearing force reduced 2FI model. These 'Model-F' and 'Model-P' values imply that the selected models are highly significant and there is only a less than 0.02% chance that these large 'Model-F' values could occur due to noise. The associated P value is also used to estimate whether F is large enough to indicate statistical significance. If P value is lower than 0.05, it indicates that the model is statistically significant as stated by Zulkali et al., [16].

The same tables also show other adequacy measures e.g. R-squared, adjusted R-squared, and predicted R-squared values. All the adequacy measures are in logical

agreement and indicate significant relationships. Moreover, adequate precision compares range of predicted value at the design points to average prediction error. The adequate precision ratios in all cases are dramatically greater than 4 indicating adequate models discrimination.

Table 4.12: ANOVA table for weld width linear model

| Source | Sum of Squares | df | Mean Square | F Value | p-value Prob > F | |
|--------|---------------|-----|-------------|---------|------------------|---|
| Model | 1.032E+005 | 3 | 34388.29 | 23.85 | < 0.0001 | significant |
| P | 18934.52 | 1 | 18934.52 | 13.13 | 0.0028 | |
| S | 12117.71 | 1 | 12117.71 | 8.41 | 0.0117 | |
| F | 72112.63 | 1 | 72112.63 | 50.02 | < 0.0001 | |
| Residual | 20182.67 | 14 | 1441.62 | | | |
| $R^2 = 0.8364$ | Adj. $R^2$ =0.8013 | | Pred. $R^2$ =0.7309 | | Adeq. Precision = 15.062 | |

Table 4.13: ANOVA table for weld penetration depth 2FI model

| Source | Sum of Squares | df | Mean Square | F Value | p-value Prob > F | |
|--------|---------------|-----|-------------|---------|------------------|---|
| Model | 1.520E+006 | 6 | 2.534E+005 | 114.39 | < 0.0001 | significant |
| P | 5.447E+005 | 1 | 5.447E+005 | 245.89 | < 0.0001 | |
| S | 7.542E+005 | 1 | 7.542E+005 | 340.44 | < 0.0001 | |
| F | 1.577E+005 | 1 | 1.577E+005 | 71.20 | < 0.0001 | |
| P-S | 43512.50 | 1 | 43512.50 | 19.64 | 0.0010 | |
| P-F | 8712.04 | 1 | 8712.04 | 3.93 | 0.0729 | |
| S-F | 11511.34 | 1 | 11511.34 | 5.20 | 0.0436 | |
| Residual | 24367.85 | 11 | 2215.26 | | | |
| Cor Total | 1.545E+006 | 17 | | | | |
| $R^2 = 0.9842$ | Adj. $R^2 = 0.9756$ | | Pred. $R^2 = 0.9559$ | | Adeq. Precision = 37.979 | |

Table 4.14: ANOVA table for weld resistance 2FI model

| Source | Sum of Squares | df | Mean Square | F Value | p-value Prob > F | |
|--------|---------------|-----|-------------|---------|------------------|---|
| Model | 3.587E+005 | 6 | 59779.23 | 45.84 | < 0.0001 | significant |
| P | 1.314E+005 | 1 | 1.314E+005 | 100.74 | < 0.0001 | |
| S | 1.385E+005 | 1 | 1.385E+005 | 106.16 | < 0.0001 | |
| F | 4.50 | 1 | 4.50 | 3.450E-003 | 0.9542 | |
| P-S | 39762.00 | 1 | 39762.00 | 30.49 | 0.0002 | |
| P-F | 11760.45 | 1 | 11760.45 | 9.02 | 0.0120 | |
| S-F | 37296.75 | 1 | 37296.75 | 28.60 | 0.0002 | |
| Residual | 14346.26 | 11 | 1304.21 | | | |
| Cor Total | 3.730E+005 | 17 | | | | |
| $R^2 = 0.9615$ | Adj. $R^2 = 0.9406$ | | Pred. $R^2 = 0.8934$ | | Adeq. Precision = 26.563 | |

Table 4.15: ANOVA table for shearing force reduced 2FI model

| Source | Sum of Squares | df | Mean Square | F-Value | p-value Prob > F | |
|---|---|---|---|---|---|---|
| Model | 3.091E+007 | 5 | 6.183E+006 | 12.54 | 0.0002 | Significant |
| P | 9.169E+006 | 1 | 9.169E+006 | 18.60 | 0.0010 | |
| S | 1.137E+007 | 1 | 1.137E+007 | 23.06 | 0.0004 | |
| F | 4.317E+006 | 1 | 4.317E+006 | 8.76 | 0.0119 | |
| P-S | 3.299E+006 | 1 | 3.299E+006 | 6.69 | 0.0238 | |
| S-F | 2.762E+006 | 1 | 2.762E+006 | 5.60 | 0.0356 | |
| Residual | 5.914E+006 | 12 | 4.929E+005 | | | |
| Cor Total | 3.683E+007 | 17 | | | | |

$R^2$ = 0.8394    Adj. $R^2$ = 0.7725    Pred. $R^2$ = 0.6820    Adeq. Precision = 12.265
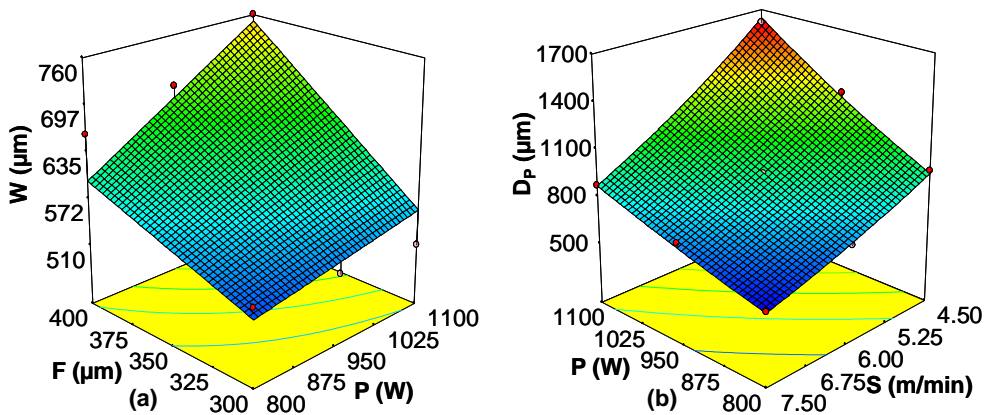


Fig 4.4: 3D graphs to show effects of (a) F and P on weld width, W for S = 6.0m/min, and (b) P and S on penetration depth, $D_P$ for F = 300μm.
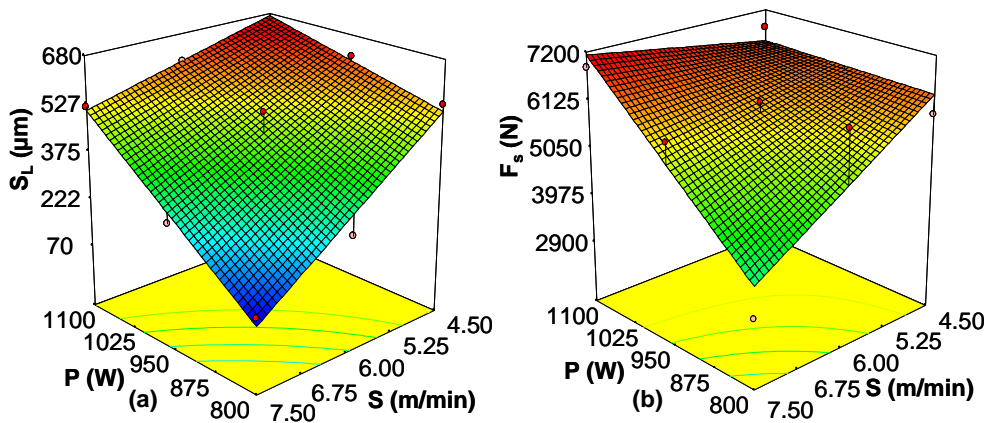


Fig 4.5: 3D graphs to show effects of (a) P and S on weld resistance length, $S_L$ for F = 400μm, and (b) P and S on shearing force, $F_s$ for F = 300μm.

Again, the ANOVA table for the weld width model shows that there is a linear relationship between weld width and weld parameters, and the fiber diameter (FD) is the most important factor affecting the weld width. For the weld penetration depth model, the ANOVA table illustrates that linear terms of laser power (P), welding speed (S), and fiber diameter (F) and two-factor interactions (2FI) of laser power-welding speed (P-S), and welding speed-fiber diameter (S-F) are the significant model terms associated with the weld penetration depth. Nevertheless, linear terms of laser power (P), welding speed (S), and fiber diameter (F) have the most significant effects on the weld penetration depth. For the weld resistance length model, ANOVA table demonstrates that linear terms e.g. laser power (P), and welding speed (S) and all the three two-factor interactions (2FI) i.e. laser power-welding speed (P-S), welding speed-fiber diameter (S-F), and laser power-fiber diameter (P-F) are significant model terms. However, linear term of fiber diameter is added to support hierarchy of weld resistance length model. Finally, for the weld shearing force model, the ANOVA table shows that the linear term of laser power (P), welding speed (S), and fiber diameter (F) and two-factor interactions of laser power-welding speed (P-S) and welding speed-fiber diameter (S-F) are significant model terms. However; laser power (P) and welding speed (S) are the most significant factors associated with shearing force. Effects of these individual significant model terms and their interactions (projected lines on the base) on weld width, penetration depth, resistance length and shearing force have also been illustrated graphically in Figs 4.4(a)-(b) and 4.5(a)-(b).

Moreover, a positive sign of the coefficient represents a synergistic effect, while a negative sign indicates an antagonistic effect. From the tables, it is found that all linear variables have positive effect on weld width; linear term laser power and interaction term welding speed-fiber diameter have positive relationship with weld penetration depth; linear parameter laser power and its interactions with welding speed and fiber diameter affect positively on weld resistance length; and finally, laser power and laser poser-welding speed have positive impact on weld shearing force. These abovementioned synergistic effects indicate that their corresponding response factors will increase with an increase in aforestated factors; otherwise decreases.

From the results shown in Tables 4.4-4.15, it is, therefore, apparent that the developed models are fairly accurate and can be used for further analyses. The final mathematical models as derived by design expert software are shown below:

(a) in terms of coded factors:

Weld width
$$W = -221.78917 + 0.26482P + 21.185S + 1.265F \tag{3}$$

Weld penetration depth
$$D_P = 891.94 + 213.06P - 250.69S - 93.61F - 73.75\,P \times S$$
$$- 26.94\,P \times F + 30.97\,S \times F \tag{4}$$

Weld resistance Length
$$S = 423.94 + 104.64P - 107.42S - 0.50F + 70.50\,P \times S$$
$$+ 31.31\,P \times F - 55.75\,S \times F \tag{5}$$

Weld shearing force

$$F_s = 5418.03 + 874.12P - 973.25S - 489.75F + 642.13\ P \times S - 479.75\ S \times F \tag{6}$$

(b) in terms of actual factors:

Weld width

$$W = -221.78917 + 0.26482P + 21.18500S + 1.26590F \tag{7}$$

Weld penetration depth

$$D_P = -995.0 + 4.64P - 0.28S - 0.94F - 0.33\ P \times S - 3.6 \times 10^{-3}\ P \times F + 0.42S \times F \tag{8}$$

Weld resistance length

$$S_L = 1807.2778 - 2.64333P - 109.11111S + 0.48463F + 0.31333P \times S + 4.17407 \times 10^{-3}\ P \times F - 0.74333\ S \times F \tag{9}$$

Weld shearing force

$$F_s = 10037.31944 - 11.29583P - 1121.19444S + 28.585\ F + 2.85389\ P \times S - 6.39667\ S \times F \tag{10}$$

### 4.3.1.3 Validation of the models developed

Normality of residual data, pattern of error variance, presence of outliers, and amount of residuals in prediction are checked to ensure statistical validation of the developed models. The normality of data is verified by plotting the normal probability plot (NPP) of residuals. The residual is the difference between observed and predicted value (or fitted value) obtained from the regression model. The data set is normally distributed if the points on the plot fall fairly close to the straight line. The normal probability plots of residual values for weld width, penetration depth, resistance length, and shearing force are illustrated in Figs 4.6 (a)-(d) respectively. The experimental points are reasonably aligned with predicted or fitted points suggesting the normality of data.
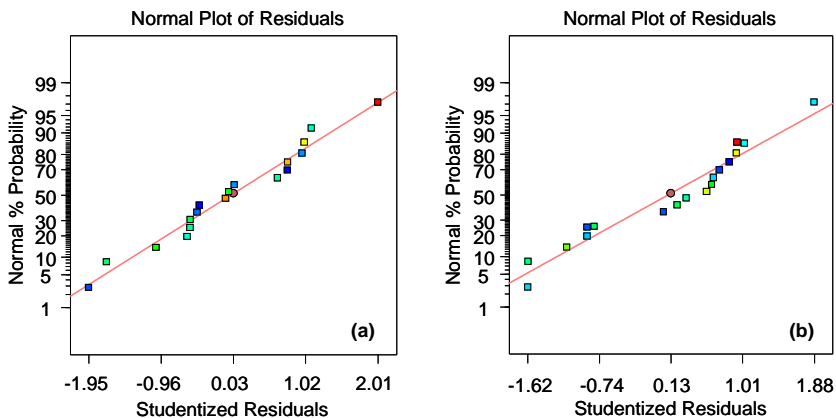


Fig. 6.8:  Normal probability plot for weld (a) width, and (b) penetration depth.
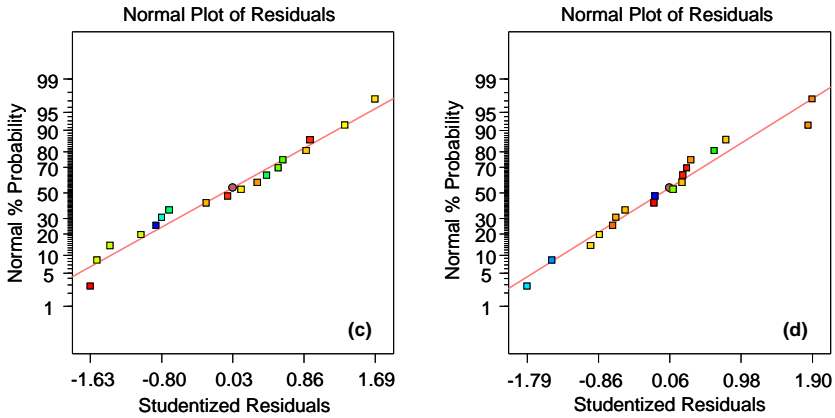
Fig. 6.8: Normal probability plot for weld (c) resistance length, and (d) shearing force

Figs 4.7 (a)-(d) demonstrate studentized residuals versus fitted values (predicted response) for weld width, penetration depth, resistance length, and shearing force respectively. The residuals are found to be scattered randomly about zero. This indicates that errors have a constant variance for all response variables. Plot of standardized residuals vs. predicted values also shows the possible existence of outliers. If a point lies far from the majority of points, it may be an outlier. It is important to identify the outliers as these can significantly influence the model and provide potentially misleading or incorrect results. As shown in the figures, all the points are within $\pm 2.0\sigma$ limits for each of the response models and confirm no existence of such outliers.



Fig. 4.7: Studentized residual vs predicted plot for weld (a) width, and (b) penetration depth.

Figs 4.8(a)-(d) are showing the relationships between the actual and predicted values of weld width, penetration depth, resistance length, and shearing forces respectively. These figures illustrate that the developed models are adequate and predicted results are in good agreement with the measured data as the residuals tend to be close to the diagonal line.

70
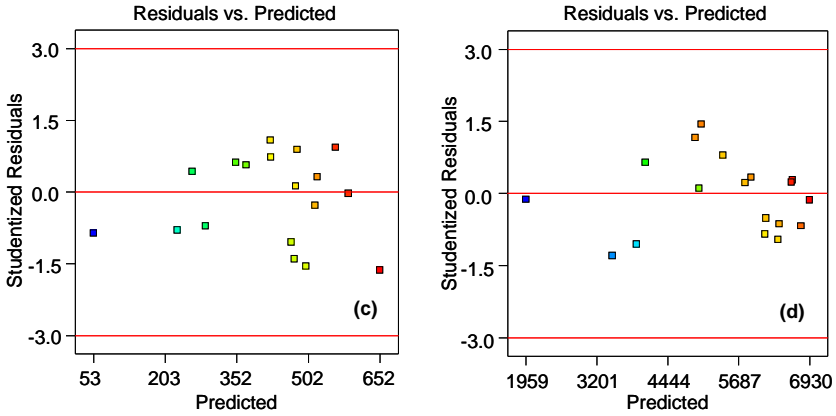
Fig. 4.7: Studentized residual vs predicted plot for weld (c) resistance length, and (d) shearing force.
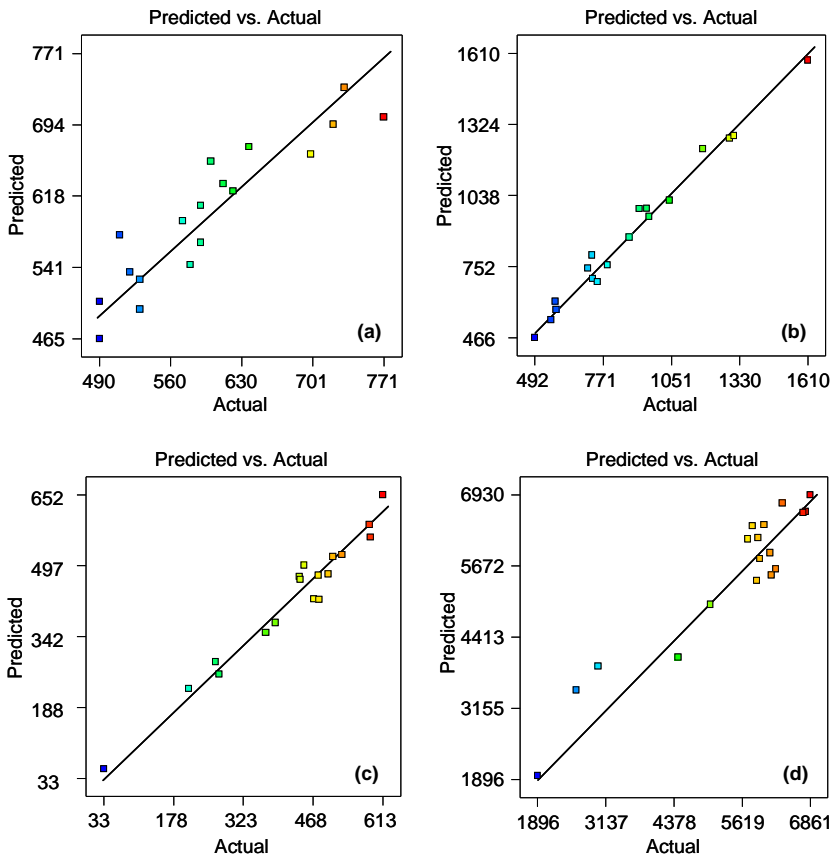


Fig. 4.8: Scatter diagrams of weld (a) width, (b) penetration depth, (c) resistance length, and (d) shearing force.

Besides, in order to validate the developed response surface equations derived from multiple regression analyses, three confirmation experiments are conducted

with welding conditions chosen randomly within the ranges for which the equations are developed. The actual results are calculated as the average of three measured results for each response. The actual results, predicted values and calculated percentage error of confirmation experiments are furnished in Table 4.16. It is observed from the validation experiments that there is a small percentage error between the estimated and the experimental values. These results indicate that the developed models can yield nearly accurate results.

Table 4.16: Confirmation Experiments

| No. of Expt | Process Parameters | | | Response Factors | | | | |
|---|---|---|---|---|---|---|---|---|
| | P (W) | S (m/min) | F (µm) | | W (µm) | $D_P$ (µm) | $S_L$ (µm) | $F_s$(N) |
| Expt. I | 1000 | 7.0 | 300 | Actual | 570 | 840 | 450 | 6167 |
| | | | | Predicted | 571.1 | 853.04 | 430.097 | 6012.9 |
| | | | | Error (%) | -0.192 | -1.53 | 4.4 | 2.49 |
| Expt. II | 900 | 6.5 | 400 | Actual | 660 | 634 | 317 | 4137 |
| | | | | Predicted | 660.61 | 668.68 | 315.9 | 4081.2 |
| | | | | Error (%) | -0.093 | -5.47 | 3.47 | 1.35 |
| Expt. III | 850 | 5.0 | 300 | Actual | 485 | 939 | 454 | 6188 |
| | | | | Predicted | 489 | 975.1 | 441.3 | 5939.4 |
| | | | | Error (%) | -0.825 | -3.84 | 2.79 | 4.02 |

## 4.3.2 Process parameter optimization

### 4.3.2.1 Numerical optimization

Two criteria are introduced in this numerical optimization. The first set of criteria are to create a full-depth penetration weld and maximize weld penetration depth, resistance length and shearing force with no limitation on either process parameters or weld width. In this case, all the process parameters and weld width (first response) are set within a specified range. Furthermore, lowering the laser power and increasing the welding speed are the most common techniques used in automotive industries to produce relatively low-cost and excellent weld joints. Taking these cost and quality aspects into account, second set of criteria for process parameter optimization are fixed to maximize weld penetration depth; resistance length; shearing force; and welding speed, and minimize the laser power as well as weld width. Table 4.17 summarizes these two criteria, lower and upper limits as well as importance for each input and response factor.

Table 4.17: Optimization criteria used in this study

| Parameters or Responses | Limits | | Importance | Criterion | |
|---|---|---|---|---|---|
| | Lower | Upper | | First | Second |
| P (W) | 800 | 1100 | 3 | is in range | minimize |
| S (m/min) | 4.5 | 7.5 | 3 | is in range | maximize |
| F (µm) | 300 | 400 | 3 | is in range | is in range |
| W (µm) | 460 | 500 | 5 | is in range | minimize |

| | | | | | |
|---|---|---|---|---|---|
| $D_P(\mu m)$ | 600 | 1200 | 5 | maximize | maximize |
| $S_L(\mu m)$ | 300 | 600 | 5 | maximize | maximize |
| $F_s$ (N) | 4500 | 6800 | 5 | maximize | maximize |

Table 4.18: optimal solutions as obtained based on first criterion

| Sol[n] No. | P (W) | S (m/min) | F (μm) | W (μm) | $D_P$ (μm) | $S_L$ (μm) | $F_s$ (N) |
|---|---|---|---|---|---|---|---|
| 1 | 920.52 | 4.50 | 302.30 | 500.00 | 1200.06 | 477.816 | 6355.22 |
| 2 | 926.36 | 4.50 | 301.08 | 500.00 | 1215.16 | 476.755 | 6364.49 |
| 3 | 927.61 | 4.50 | 300.82 | 500.00 | 1218.41 | 476.519 | 6366.48 |
| 4 | 931.48 | 4.50 | 300.01 | 500.00 | 1228.46 | 475.773 | 6372.63 |
| 5 | 919.99 | 4.50 | 301.59 | 499.03 | 1200.00 | 476.938 | 6352.98 |
| 6 | 924.44 | 4.50 | 300.00 | 498.12 | 1213.76 | 475.628 | 6361.74 |
| 7 | 922.22 | 4.53 | 301.41 | 500.00 | 1200.01 | 475.563 | 6344.62 |
| 8 | 923.06 | 4.55 | 300.83 | 499.86 | 1200.01 | 474.264 | 6339 |
| 9 | 913.08 | 4.50 | 300.00 | 495.11 | 1190.01 | 475.414 | 6344.18 |
| 10 | 900.07 | 4.50 | 300.00 | 491.67 | 1162.78 | 475.168 | 6324.05 |
| 11 | 898.64 | 4.50 | 300.00 | 491.29 | 1159.80 | 475.141 | 6321.84 |
| 12 | 917.47 | 4.65 | 300.00 | 499.45 | 1172.68 | 468.817 | 6287.84 |
| 13 | 884.79 | 4.50 | 300.00 | 487.62 | 1130.82 | 474.88 | 6300.42 |
| 14 | 855.00 | 4.50 | 300.00 | 479.73 | 1068.52 | 474.317 | 6254.35 |

Table 4.19: optimal solutions as obtained based on second criterion

| Sol[n] No. | P (W) | S (m/min) | F (μm) | W (μm) | $D_P$ (μm) | $S_L$ (μm) | $F_s$ (N) |
|---|---|---|---|---|---|---|---|
| 1 | 800.00 | 4.77 | 300.00 | 470.88 | 916.09 | 451.314 | 5965.11 |
| 2 | 800.00 | 4.80 | 300.00 | 471.59 | 911.47 | 448.596 | 5939.84 |
| 3 | 802.02 | 4.77 | 300.00 | 471.46 | 919.84 | 451.353 | 5968.21 |
| 4 | 800.04 | 4.75 | 300.09 | 470.50 | 919.30 | 453.283 | 5983.05 |
| 5 | 800.00 | 4.82 | 300.00 | 471.99 | 908.87 | 447.071 | 5925.66 |
| 6 | 804.18 | 4.76 | 300.00 | 471.84 | 925.40 | 452.283 | 5979.79 |
| 7 | 807.61 | 4.77 | 300.00 | 472.95 | 930.95 | 451.888 | 5980.76 |
| 8 | 813.06 | 4.77 | 300.00 | 474.28 | 942.66 | 452.885 | 5997.41 |
| 9 | 815.01 | 4.77 | 300.00 | 474.91 | 945.81 | 452.68 | 5998.13 |
| 10 | 817.99 | 4.76 | 300.00 | 475.35 | 954.13 | 454.221 | 6016.53 |
| 11 | 819.99 | 4.75 | 300.00 | 475.72 | 959.27 | 455 | 6026.5 |
| 12 | 829.78 | 4.76 | 300.00 | 478.59 | 976.98 | 454.991 | 6039.66 |
| 13 | 839.99 | 4.78 | 300.00 | 481.64 | 994.99 | 454.895 | 6052.58 |
| 14 | 800.00 | 5.37 | 300.00 | 483.59 | 832.94 | 402.456 | 5510.94 |

Tables 4.18 and 4.19 show the optimal solution based on the two optimization criteria as determined by design-expert software. The optimization results clearly demonstrate that, whatever the optimization criteria, the fiber diameter has to be

around its lower limit of 300µm to achieve the maximum weld penetration depth, resistance, as well as shearing force and minimum weld width. This result support the discussion made earlier on the effect of fiber diameter on the responses.

Again, Table 4.18 demonstrates the optimal welding conditions according to the first criterion that would lead to maximum weld penetration depth, resistance and shearing force of about 1228µm, 478µm and 6373N respectively, at high laser power and welding speed of 932W and 4.5 m/min respectively. However, with acceptable weld penetration depth, resistance and shearing force, the laser power can be minimized to its lowest value and welding speed of 5.37 m/min can be used instead of 4.5 m/min. In this case, as shown in Table 4.19, the weld penetration depth, resistance and shearing force would be of 833 µm, 402µm and 5511N respectively, which are much higher than the prerequisite values for the weld.

### 4.3.2.2 Graphical optimization

It is obvious that the graphical optimization allows visual selection of the optimum welding conditions according to certain criterion. The result of the graphical optimization are the overlay plots, these type of plots are extremely practical for quick technical use in the workshop to choose the values of the welding parameters that would achieve certain response value for these types of materials. In this case, for each response, the limits lower and/or upper have been chosen according to the numerical optimization results. The same two criteria, which are proposed in the numerical optimization, are introduced in the graphical optimization. As shown in Figs 4.9(a) and (b), the yellow areas on the overlay plots are the regions that meet the proposed criteria for fiber diameter of 300µm.
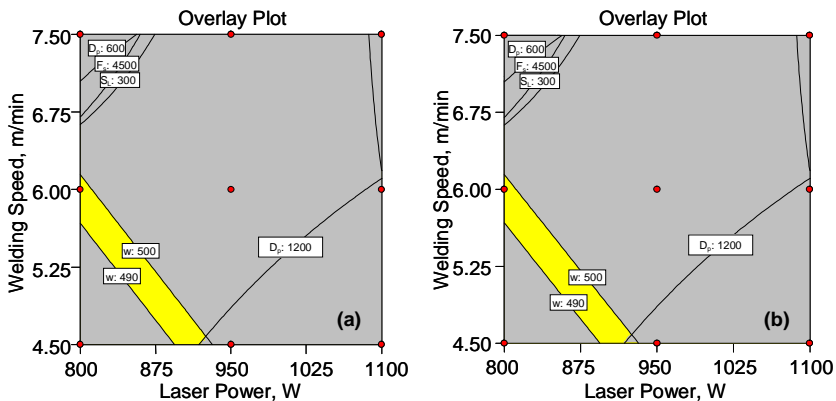


Fig 4.9: Overlay plot shows the region of optimal welding condition based on (a) first criterion and (b) second criterion at F=300µm

From Table 4.18 and Fig 4.9(a), it is evident that the optimal working range for the laser power has to be between 855W and 931.48 W, and the welding speed has to be between 4.5 m/min and 4.65 m/min using a fiber diameter of 300µm. However, with acceptable weld penetration depth, resistance and shearing force, optimal sets of the laser power and welding speed are 800-840W and 4.75-5.37 m/min as can be seen in Table 4.19 and Fig 4.9(b). Since optimal range of laser power and welding speed selected based on second criterion is respectively much lower and

higher than that of first-criterion-based laser power and welding speed, any combination of process parameters of the second optimal set would cause less heat input to constrained overlap joints to be made. This reduced energy density input to weld materials would, ultimately, result in less distortion, and formation of cracks, blow holes as well as spatter, and hence improve the weld quality. The results given in Table 4.20 also support the improvement of weld quality at lower laser power and higher welding speed. Moreover, increased welding speed would cause reduction in the welding cost that would, in turn, somewhat improve the process productivity.

Table 4.20: Visual inspection of weld quality

| Process Parameters | | | Visual check Cracks | Visual check Blow holes | Visual check Spatter |
|---|---|---|---|---|---|
| P (W) | S (m/min) | F (µm) | | | |
| 800 | 4.5 | 300 | 0 | 0 | 1 |
| 950 | 4.5 | 300 | 0 | 0 | 2 |
| 1100 | 4.5 | 300 | 0 | 0 | 2 |
| 800 | 6 | 300 | 0 | 0 | 1 |
| 950 | 6 | 300 | 1 | 0 | 2 |
| 1100 | 6 | 300 | 1 | 0 | 1 |
| 800 | 7.5 | 300 | 0 | 0 | 0 |
| 950 | 7.5 | 300 | 1 | 0 | 1 |
| 1100 | 7.5 | 300 | 1 | 0 | 1 |

0= No defect, 1= exist but acceptable, 2-3 = Not acceptable

## 4.4 CONCLUSIONS

Using the laser machine and within the limits of the laser parameters considered in this study the following points can be concluded:

- Full factorial design can be used to optimize the laser welding process in order to obtain the best weld bead parameters as well as shearing force of the welded component, and also to determine the corresponding optimum process factors.
- Whatever the optimization criteria, fiber diameter has to be around its lower limit to achieve a weld with narrower width, deeper penetration, longer resistance length and with it, the greater shearing force.
- A laser power of 800-840W with fiber diameter of 300µm and a welding speed of 4.75-5.37 m/min are the optimal input parameters to obtain an excellent welded component made of the selected martensitic stainless steels.
- Strong, efficient and low-cost weld joints could be achieved using the welding conditions drawn from the numerical optimization.
- The graphical optimization results allows quicker search for the optimal settings of welding.

## REFERENCES

1. Weichiat, C., Paul, A., Pal, M., 2009, $CO_2$ laser welding of galvanized steel sheets using vent holes, Materials and Design, 30:245–251.

2.  Huang, Q., Hagstroem, J., Skoog, H., Kullberg, G., 1991, Effect of laser parameter variation on sheet metal welding, Int. J. Join. Mater., 3:79–88.
3.  Benyounis, K.Y., Olabi., A.G., 2008, Optimization of different welding processes using statistical and numerical approaches - A reference guide, Advances in Engineering Software, 39:483–496.
4.  Montgomery, D.C., 2004, Design and Analysis of Experiments, 6th ed. John Wiley and Sons, Inc., New York.
5.  Yang, Y.K., Chuang, M.T. Lin, S.S., 2009, Optimization of dry machining parameters for high-purity graphite in end milling process via design of experiments methods, Journal of Materials Processing Technology, 209:4395–4400
6.  Douglass, D.M., Wu, C.Y., 2003, Laser welding of polyolefin elastomers to thermoplastic polyolefin, In: Proceedings of the 22nd international Congress on applications of lasers & electro-optics, Jacksonville, Florida, USA, 95:118–23.
7.  Koganti, R., Karas, C., Joaquin, A., Henderson, D., Zaluzec, M., Caliskan, A., 2003, Metal inert gas (MIG) welding process optimization for joining aluminum sheet material using OTC/DAIHEN equipment, In: Proceedings of IMECE'03, November 15–21, Washington [DC]: ASME International Mechanical Engineering Congress, pp. 409–425.
8.  Balasubramanian, V., Guha, B., 2004, Fatigue life prediction of load carrying cruciform joints of pressure vessel steel by statistical tools. J Mater Des, 25:615–623.
9.  Cicala, E., Duffet, G., Andrzjewski, H., Grevey, D., 2005, Optimization of T-joint properties in Al-Mg-Si alloy laser welding, 24th International Congress on Applications of Lasers and Electro-Optics, ICALEO: 543-548.
10. Kim, C., Choi, W., Kim, J., Rhee, S., 2008, Relationship between the weldability and the Process parameters for laser-TIG Hybrid welding of galvanized steel sheets, Materials Transactions, 49:179-186.
11. Datta, S., Bandyaopadhyay, A., Pal, P.K., 2008, Modeling and optimization of features of bead geometry including percentage dilution in submerged arc welding using mixture of fresh flux and fused slag, Int. J. Adv. Manuf. Technol., 36:1080–1090.
12. Benyounis, K.Y., Olabi, A.G., Hashmi, M.S.J., 2008, Multi-response optimization of $CO_2$ laser-welding process of austenitic stainless steel, Optics & Laser Technology, 40:76–87
13. Sarsılmaz, F., Çaydaş, U., 2009, Statistical analysis on mechanical properties of friction-stir-welded AA 1050/AA 5083 couples, Int. J. Adv. Manuf. Technol., 43:248–255.
14. Khan M.M.A., Romoli L., Fiaschi M., Sarri F., Dini G., 2010, Experimental investigation on laser beam welding of martensitic stainless steels in a constrained overlap joint configuration, Journal of Materials Processing Technology, 210(10):1340-1353.
15. Design-Expert software, v7, user's guide, technical manual, Stat-Ease Inc., Minneapolis, MN; 2005.
16. Zulkali, M.M.D., Ahmad, A.L., Norulakmal, N.H., 2006, Oryza sativa L. husk as heavy metal adsorbent: optimization with lead as model solution, Bioresour. Technol., 97:21–25.

# CHAPTER 5

## LASER BEAM WELDING OF DISSIMILAR STAINLESS STEELS IN A FILLET JOINT CONFIGURATION

*This chapter investigates laser beam welding of dissimilar AISI 304L and AISI 430 stainless steels in fillet joint configuration. Experimental studies are focused on effects of laser power, welding speed, defocus distance, beam incident angle, and line energy on weld bead geometry and shearing force. Metallurgical analysis is conducted on a selected weld only to show various microstructures typically formed at different zones and the consequent change in microhardness.*

*Laser power and welding speed are the most significant factors affecting weld geometry and shearing force. All the bead characteristics but radial penetration depth decreases with increased beam incident angle. The focused beam allows selecting lower laser power and faster welding speed to obtain the same weld geometry. Weld shape factor increases rapidly due to keyhole formation for line energy input ranging from 15kJ/m to 17kJ/m. For the line energy input above the 17kJ/m, generation of upper keyhole plasma plume forms a chalice shaped bead profile.*

*Fusion zone microstructures contain a variety of complex austenite–ferrite structures because of solidification behaviour and subsequent solid-phase transformation. Variation in local microhardness observed across the weld is correlated to the fraction intermix of each base metal and the redistribution of segregated austenite- and ferrite-promoting elements in the weld. Local microhardness of fusion zone is greater than that of both base metals.*

## 5.1 INTRODUCTION

With the growing availability of new materials, industries, nowadays, utilize a variety of materials to make their products on a large scale with a view to improve performance and reduce cost. Among the various material combinations, the demands for using ferritic/austenitic (F/A) joints in power generation, chemical, petrochemical, nuclear and automotive industries are enormous [1]. Thus, F/A joints are among one which has extensive industrial application in terms of production volume. This ultimately leads to an increased demand for techniques to weld these dissimilar materials and their use in large scale industrial production [2]. Of the available welding techniques, laser beam welding has received increasing attention due to rapid development in high-energy density beam technology in recent years [3]. Several researchers have reported the laser beam welding of dissimilar materials.

Li and Fontana [4] investigated the $CO_2$ laser welding of AISI 304L and AISI 12L13 in butt joint configuration and found that the offset and the impingement angle of the laser beam are the two key parameters for controlling the melt ratio of the dissimilar materials. The strength of the laser welds was found to be higher than both the yield strength of AISI 304L and the rupture strength of AISI 12L13 under the test conditions adopted. Mai and Spowage [5] conducted pulsed Nd:YAG laser autogenous welding of dissimilar metals for three different metal combinations and found no hot cracking in the welded joints. However, the porosity observed in the weld seam had a seemingly visible relationship with the welding speed. Liu et al. [6] studied the parametric effects on seam morphology and mechanical properties of CW Nd:YAG laser welded dissimilar cast Ni-based super alloy K418 and alloy steel 42CrMo in butt configuration. X and T shape welded seam morphology were observed, and asymmetrical welded seam cross-section was obtained. The microhardness of the laser-welded seam was lower than the base metal. The strength of the joint was, however, equal to that of the base metal, and the fracture mechanism showed admirable ductility. Berretta et al. [7] investigated the effects of laser position on the properties of two dissimilar AISI 304 and AISI 420 stainless steels. They found that joints obtained under all the welding conditions were uniform, and variations in beam position did not influence weld fillet geometry, which was typical of keyhole welding. Depending on the amount of shift of the laser beam position from the AISI 420 steel to AISI 304 steel, a gradual reduction in hardness along the cross-section of the weld zone was observed. Fracture occurred outside the weld zone in the tensile test. Besides, Mousavi and Sufizadeh [8] examined the pulsed Nd:YAG laser welding of AISI 321 austenitic and AISI 630 (17-4PH) precipitation hardening stainless steels in a circular butt weld configuration focusing their studies on the effects of laser power, beam diameter and pulse duration on the depth and width of the welds. The results showed that both weld depth and weld width increased with voltage. The pulse duration had bilateral effects on the weld bead depth and width. Microhardness was found to be maximum and minimum respectively at AISI 630 and AISI 321 sides. Pekkarinen and Kujanpää [9] investigated to determine empirically the microstructural changes occurred in ferritic (AISI 430 & AISI 41003) and duplex (AISI 2205 and LDX 2101) stainless steels when heat input was controlled by welding parameter. Autogenous bead-on-plate welds were made without shielding gas using 5 kW fiber laser. Microstructures in both ferritic and duplex stainless steels were found to be

dependent on composition and hence, welding parameters must be adjusted for each steel grade separately. With low-heat input, there was almost no martensite in AISI 430 stainless steels and grain size was high. Increasing heat input increased also the amount of martensite and decreased the grain size. The literatures support the fact that autogenous laser welding technique is suitable for producing weldable joints of dissimilar materials having considerable mechanical properties. Weld material, joint configuration, and welding parameters have significant effects on the weld seam characteristics, weld microstructure, the presence of defects and mechanical properties. Besides, it appears that laser welding of dissimilar ferritic AISI 430 and austenitic AISI 304L stainless steels in a circular and constrained fillet joint configuration has not been studied and reported yet. This is because this configuration complicates the joint design and requires accurate positioning of the focused beam at the corner. Otherwise, the focused beam can interfere with the vertical surface on its way to weld plane and reflect back to the adjacent horizontal surface making the welding process more complex.

Welding the dissimilar metals is still more challenging than that of similar metals due to the difference in the physical, mechanical, and metallurgical properties of the metals to be joined. Difference in thermal expansion coefficients of ferritic and austenitic steels may cause crack initiation at the interface, formation of hard zone close to weld interface, relatively soft regions adjacent to the hard zone, large hardness difference between hard and soft zones, and expected difference in microstructure leading to failure of the weld in service [10]. Pan and Zhang [11], on the other hand, report that micro-structural variations depend on the carbon content, the cooling rate, and the segregation of alloying elements. Proper selection of components, joint design, process, and process parameters are, therefore, mandatory to make the welds with desired properties during the laser welding of dissimilar ferritic and austenitic stainless steels.

### 5.1.1    Research objectives

Two tubular-shaped parts made of ferritic AISI 430 and austenitic AISI 304L stainless steels are assembled together ensuring a clearance between them, and then welded circularly to produce the desired fillet joint. In these contexts, two possibilities emerge to solve the associated problems: adjustment of laser power, welding speed, and defocus distance or variation of the laser beam incident angle with respect to the vertical surface. In the first case, it is possible to control the energy input into the metals to be welded and hence heating and cooling rates of the weld pool, which can improve the metallurgical characteristics of the weld area. In the second case, control of melting ratio of two metals can compensate for the differences in absorption of the laser beam and the thermal conductivity. This paper, therefore, examines Nd:YAG laser welding of dissimilar ferritic and austenitic stainless steels in a constrained and circular fillet joint configuration. Experimental studies include

- effects of above laser welding parameters on
  - ✓ the weld bead characteristics such as weld width, penetration depth, radial penetration, resistance length,
  - ✓ the mechanical properties such as shearing force

- effects of energy per unit length are also studied to
  - ✓ show how energy input influences the weld bead characteristics, and
  - ✓ explain various phenomena related to laser welding.
- Finally, metallographic study is performed on a selected welded specimen only to demonstrate the microstructures that typically form at different zones and the consequent changes in local microhardness.

## 5.2 MATERIALS AND EXPERIMENTAL PROCEDURES

### 5.2.1 Materials
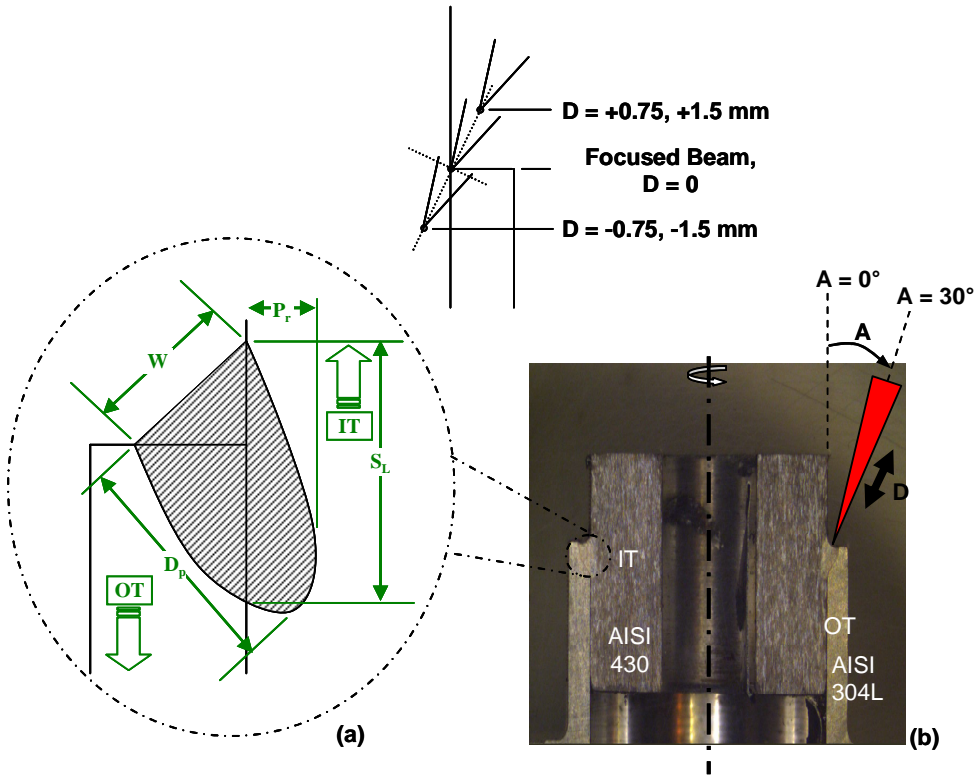


Fig. 5.1: Diagrams showing (a) bead characteristics of a welded fillet joint (W: Weld Width; $S_L$: Weld Resistance Length; $D_p$: Weld Penetration Depth; and $P_r$: Weld Radial Penetration), and (b) adopted laser-welding procedure

Two tubular-shaped parts are made of ferritic AISI 430 (cold drawn, annealed and centerless ground) and austenitic AISI 304L (annealed, cold finished and centerless ground) stainless steels. These parts are welded circularly to make a fillet joint. This dissimilar joint is selected based on both technical and economical aspects, because they can provide satisfactory service performance and considerable savings. Moreover, in automotive industries, these materials are frequently used in welded form for making different types of fuel injectors. The chemical compositions of base metals available in as received condition and the weld seam characteristics are shown in Table 5.1 and Fig. 5.1 respectively. The

inside diameter of the outer tube and the outside diameter of the inner tube are machined to Ø11.8±0.025 mm and Ø11.758±0.015 mm respectively to have a clearance between the parts when assembled. Inner (IT) and outer (OT) tubes are first assembled and then laser welded.

Table 5.1: Chemical compositions of base metals of the weld

| Base Metals | Chemical Compositions (%Wt) | | | | | | | | Thermal Conductivity 298.2K ~ 1900K (W/mK) |
|---|---|---|---|---|---|---|---|---|---|
| | C | Cr | Ni | Mn | P | S | Si | Fe | |
| AISI 304L | 0.03 | 18.0-20.0 | 8.0-12.0 | 2.0 | 0.045 | 0.03 | 1.0 | Rest | 15-25.1 |
| AISI 430 | 0.12 | 16.0-18.0 | 0.75 | 1.0 | 0.04 | 0.03 | 1.0 | Rest | 25-26.9 |

### 5.2.2 Laser welding experimental procedures

Specimens are welded circularly in a fillet joint configuration using a 1.1kW continuous wave Nd:YAG laser (Rofin DY011). The optical system consisted of a 300 µm fiber and two lenses of 200 mm focal and collimate lengths are used to deliver the laser with a minimum focal spot diameter of 300 µm. A three-step procedure is followed to locate the focal point. First, an exceptionally sharp-nosed tool of 200 mm in height is attached to laser head mounted on Z motion stage. The laser head is then set to an intended beam incident angle. Finally, the positions of the X-Y-Z motion stages are adjusted in such a way that pointed tool tip touches the planned point of focus. Laser beam is focused on this located point through the laser head at the specified angle, and the necessary rotary motion is provided to the specimen through specimen holder mounted on an X-Y motion stage. Computer control panel is interfaced with the linear X-Y-Z as well as rotary motion systems to regulate the above said movements. Defocus distance is determined by changing the position of the focusing lens of the laser head in either a backward or a forward direction with a resolution of 0.025 mm.

The experiment is initially designed based on central composite rotatable design with full replication. During experimentation, laser power, (P), welding speed (S), defocusing distance (D), and Beam incident angle (A) are selected as process input variables for laser welding. Table 5.2 shows the experimental condition, laser welding input variables, and design levels used at a glance. Each of the input variables and its working range is selected based on industrially recommended laser-welding parameters used in automotive industries.

The energy delivered per unit length of weld line is referred to as line energy (LE), which is frequently used in various laser-processing techniques and termed as a key-parameter when continuous-wave laser is used. This term is calculated as the ratio of laser power over the welding speed as shown in equation (5.1):

$$LE = 0.06 \times \frac{P}{S} (kJ/m) \tag{5.1}$$

where, LE is line energy; P is laser power in watt (W) describing the thermal source; and S is welding speed in m/min determining the irradiation time. According to the equation (5.1), the combinations of laser power of 600-1000W

and welding speed of 2.0-4.0 m/min resulted in nominal line energy input in the range of 12.0 - 24.0 kJ/m

Table 5.2: Experimental conditions and response factors

| Process Factors | Symbols | Actual Values | | | | |
|---|---|---|---|---|---|---|
| Laser power (W) | P | 600 | 700 | 800 | 900 | 1000 |
| Welding speed (m/min) | S | 2.0 | 2.5 | 3.0 | 3.5 | 4.0 |
| Angle of incidence (°) | A | 10 | 15 | 20 | 25 | 30 |
| Defocus distance (mm) | D | -1.5 | -0.75 | 0 | +0.75 | +1.5 |
| Constant Factors | | | | | | |
| Base material | | Outer Tube<br>Inner Tube | | AISI 304L<br>AISI 430 | | |
| Laser source | | Continuous Wave Nd:YAG Laser | | | | |
| Shielding gas | | Type<br>Flow rate | | Argon<br>29 l/min | | |
| Response Factors | | | | | | |
| Weld bead characteristics | | Weld width (W), weld penetration depth ($D_p$), weld radial penetration ($P_r$), and weld resistance length ($S_L$) | | | | |
| Weld mechanical Properties | | Weld shearing force ($F_S$) | | | | |
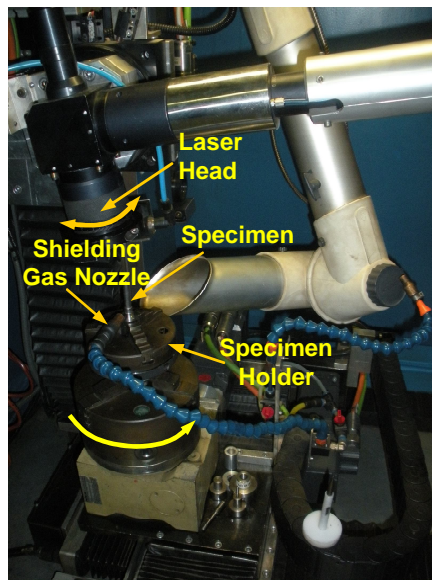


Fig. 5.2:  Photographic view of Nd:YAG laser-welding system

During the experiment, defocusing distance and laser beam incident angle are varied in the range of -1.5 - +1.5 mm and 10° - 30° respectively. Argon is used as shielding gas with a constant flow rate of 29 l/min to protect weld surface from oxidation and suppress the generation of plasma during welding. A standard

washing procedure, which is practised in the automotive industries, is followed to clean, cool and dry the specimens.

In order to investigate the effects of line energy on the selected weld bead characteristics and shear force, line energy, defocus distance, and beam incident angle were varied in the range of 12.0-21.6 kJ/m, -0.75-+0.75 mm and 10°-30° respectively. Beam incident angle and defocus distance are kept constant at their central values to study the effects of defocus distance and beam incident angle respectively. The experimental set-up for the laser-welding system is illustrated in Fig. 5.2.

Table 5.3: Design matrix with actual factors and measured mean responses.

| Standard Order | Process Factors | | | | Response Factors | | | | |
|---|---|---|---|---|---|---|---|---|---|
| | P (W) | S (m/min) | A (deg) | D (mm) | W (mm) | $S_L$ (mm) | $P_r$ (mm) | $D_p$ (mm) | $F_s$ (kN) |
| 1 | 700 | 2.5 | 15 | -0.75 | 1.173 | 1.130 | 0.160 | 1.064 | 28.18 |
| 2 | 900 | 2.5 | 15 | -0.75 | 1.573 | 1.337 | 0.240 | 1.368 | 30.04 |
| 3 | 700 | 3.5 | 15 | -0.75 | 0.953 | 0.843 | 0.094 | 0.857 | 25.61 |
| 4 | 900 | 3.5 | 15 | -0.75 | 1.272 | 1.223 | 0.173 | 1.137 | 29.02 |
| 5 | 700 | 2.5 | 25 | -0.75 | 1.213 | 0.943 | 0.353 | 1.123 | 26.51 |
| 6 | 900 | 2.5 | 25 | -0.75 | 1.250 | 1.150 | 0.466 | 1.390 | 28.36 |
| 7 | 700 | 3.5 | 25 | -0.75 | 0.977 | 0.803 | 0.273 | 0.883 | 25.25 |
| 8 | 900 | 3.5 | 25 | -0.75 | 1.000 | 0.977 | 0.387 | 1.189 | 26.81 |
| 9 | 700 | 2.5 | 15 | 0.75 | 1.263 | 1.097 | 0.167 | 1.203 | 27.89 |
| 10 | 900 | 2.5 | 15 | 0.75 | 1.543 | 1.457 | 0.293 | 1.457 | 31.12 |
| 11 | 700 | 3.5 | 15 | 0.75 | 1.020 | 0.880 | 0.130 | 0.990 | 25.94 |
| 12 | 900 | 3.5 | 15 | 0.75 | 1.375 | 1.330 | 0.200 | 1.240 | 29.98 |
| 13 | 700 | 2.5 | 25 | 0.75 | 1.050 | 0.940 | 0.320 | 0.980 | 26.48 |
| 14 | 900 | 2.5 | 25 | 0.75 | 1.100 | 1.040 | 0.430 | 1.320 | 27.38 |
| 15 | 700 | 3.5 | 25 | 0.75 | 0.499 | 0.790 | 0.200 | 0.810 | 25.13 |
| 16 | 900 | 3.5 | 25 | 0.75 | 0.950 | 0.952 | 0.316 | 1.093 | 26.59 |
| 17 | 600 | 3.0 | 20 | 0.00 | 1.040 | 0.830 | 0.140 | 0.890 | 25.49 |
| 18 | 1000 | 3.0 | 20 | 0.00 | 1.490 | 1.370 | 0.380 | 1.590 | 30.34 |
| 19 | 800 | 2.0 | 20 | 0.00 | 1.700 | 1.360 | 0.350 | 1.470 | 30.25 |
| 20 | 800 | 4.0 | 20 | 0.00 | 1.110 | 1.040 | 0.200 | 1.030 | 27.38 |
| 21 | 800 | 3.0 | 10 | 0.00 | 1.290 | 1.030 | 0.140 | 1.120 | 27.29 |
| 22 | 800 | 3.0 | 30 | 0.00 | 0.624 | 0.800 | 0.475 | 0.989 | 25.22 |
| 23 | 800 | 3.0 | 20 | -1.50 | 0.637 | 1.260 | 0.150 | 0.968 | 29.35 |
| 24 | 800 | 3.0 | 20 | 1.50 | 1.050 | 1.021 | 0.130 | 0.987 | 27.21 |
| 25 | 800 | 3.0 | 20 | 0.00 | 1.340 | 1.220 | 0.240 | 1.270 | 28.99 |
| 26 | 800 | 3.0 | 20 | 0.00 | 1.390 | 1.080 | 0.340 | 1.250 | 27.74 |
| 27 | 800 | 3.0 | 20 | 0.00 | 1.270 | 1.000 | 0.270 | 1.200 | 27.02 |
| 28 | 800 | 3.0 | 20 | 0.00 | 1.370 | 1.130 | 0.290 | 1.260 | 28.18 |
| 29 | 800 | 3.0 | 20 | 0.00 | 1.270 | 1.150 | 0.300 | 1.240 | 28.36 |
| 30 | 800 | 3.0 | 20 | 0.00 | 1.390 | 1.240 | 0.220 | 1.260 | 29.17 |

## 2.2.3 Weld bead characterization

Welding tests are carried out in a random order to avoid any systematic error in the experiment. After welding, transverse sections are prepared by cutting the samples axially using SampleMet II (Beuhler, IL) model abrasive cutter. The sectioned samples are mounted, polished, and etched for mechanical characterization. Software, Leica IM500, incorporated with an optical microscope (Leica MZ125) is used to measure weld bead width, resistance length, radial penetration, and penetration depth. Push-out tests are also conducted to assess the shearing force of the weld. Each set of experiments is replicated three times to ensure statistical accuracy. The mean value of each measured response parameter is determined and recorded for further analysis. Table 5.3 shows the average measured responses for various laser-welding conditions.

The guidance on quality levels for imperfections given in ISO 13919-1:1996 is followed to assure the desired weld quality. At this point, each welded specimen is visually inspected before and after the cut using the optical microscope. Hermetic weld is ensured by performing leak test in vacuum for each of welded specimens. During leak test, nitrogen is inflated into the assembled part at a pulsed pressure in the range 10-150 bar for the expected life cycles. This method also guarantees that the weld will not fail during its service life. In case of failure, the internal cracks generated during the welding process propagate up to the free surface and $N_2$ leakage is detected by a loss of vacuum into the chamber.

As for the microstructural characterization, the selected sample is prepared and etched with kalling II solution (5 g $CuCl_2$, 100 mL HCl, 100 mL ethanol). The microstructure is characterized by optical microscope (Reichert MF-2) and scanning electron microscopy (JEOL-JSM-5600 LV). Chemical composition of the weld material at various regions of the fusion zone is determined through energy dispersive spectrometer (EDS) analysis. The microhardness properties are assessed from inner to the outer tube by measuring the Vicker's microhardness along the line shown in Fig. 5.4.

## 5.3 RESULTS AND DISCUSSION

Various weld profile characteristics are measured with axially cut specimens using an optical microscope and are recorded for further analyses described in the succeeding sections.

Perturbation plots are used to illustrate the effects of individual process parameter such as laser power (P); welding speed (S); beam incident angle (A); and defocus distance (D) on the weld bead geometry and its mechanical properties. Contour plots are used to show the two-factor interaction effects of the selected process parameters on weld bead characteristics and shearing force.

The line energy is plotted against weld width, penetration depth, radial penetration, resistance length, and shearing force with a view to demonstrate the effects of energy input on weld profile characteristics, and to explain different laser welding phenomena as well. Angular distortion associated with laser welding has also been analyzed.

### 5.3.1 Effects of process parameters

#### 5.3.1.1 Weld bead geometry

The Fig. 5.3(a)-(d) shows the perturbation plots to compare the effects of all the process parameters at the center point in the design space. The results suggest that laser power has the most significant positive impact on the weld width; penetration depth; and resistance length, and a secondary effect on the weld radial penetration. The opposite phenomena are observed for the welding speed. This is because higher laser power and slower welding speed result in higher energy deposition on the weld area, and longer irradiation time for the deposited energy to diffuse into material.
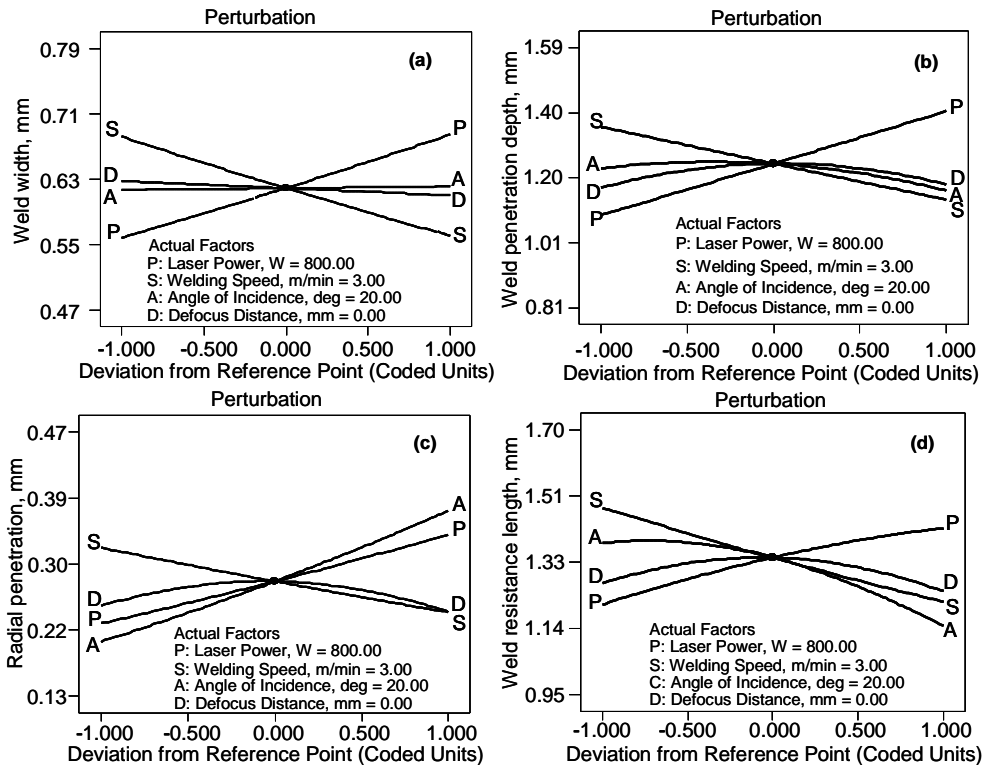


Fig. 5.3: Perturbation plot showing effect of all factors on weld (a) width, (b) penetration depth, (c) radial penetration, and (d) resistance length.

Except the initial beam incident angle (A = 10°), as shown in the Fig. 5.3(b)-(d), an increase in beam angle incident leads to a decrease in both the weld penetration depth and the resistance length with an enlargement in radial penetration depth. These facts are also evident from the Fig. 5.7(a)-(c). These phenomena are due to the following reasons: with an increase in beam incident angle, the direction of the laser beam focus changes from outer to the inner tube and the fraction of inner tube material become larger with a consequent rise in thermal conductivity of the weld molten mass. As a result, shallower weld penetration depth and shorter weld resistance length are achieved as described in [12]. Moreover, it has a small or

almost no effect on weld width as compared to other factors as can be noticed in Fig. 5.3(a).
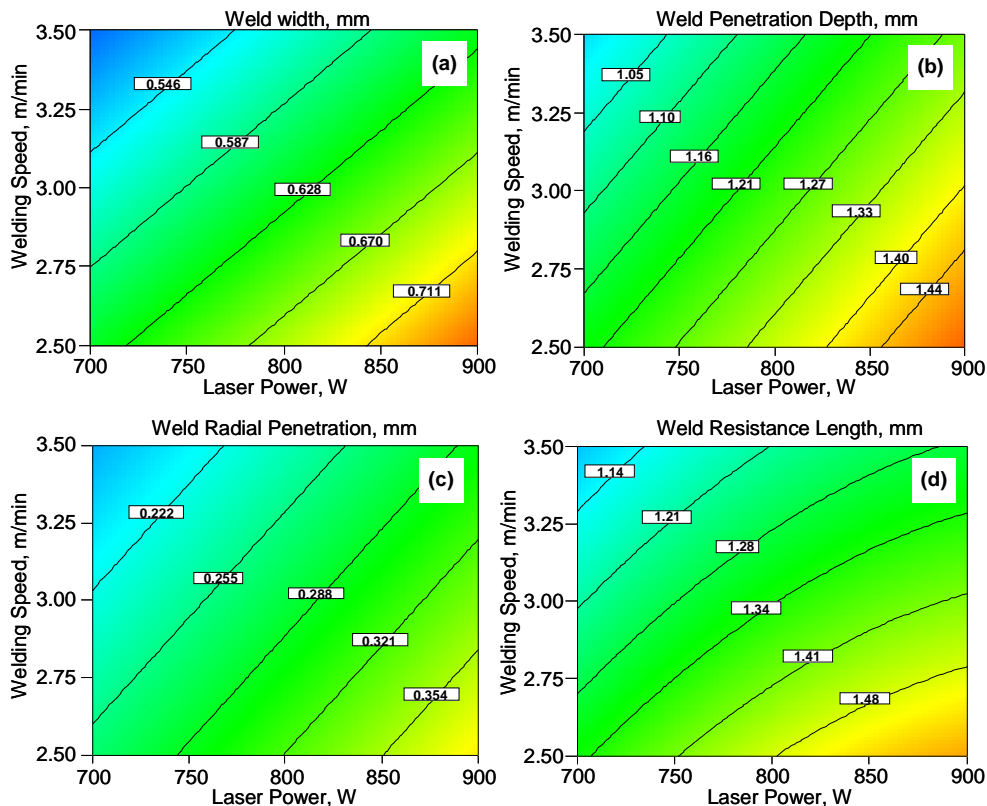


Fig. 5.4: Contour graphs to show the interaction effects of P and S on weld (a) width, (b) penetration depth, (c) radial penetration, and (d) resistance length at A = 20° and D = 0.0 mm.

At an incident angle, A = 10°, the incident laser beam remains extremely close to sidewall. A fraction of beam energy is lost due to its interference with the vertical surface on its way to the weld plane and reflects back to the adjacent horizontal surfaces. These phenomena eventually widen the weld width and reduce the weld penetration depth and the resistance length. Since the axis of the weld moves away from the contact surface with a larger beam incident angle, weld radial penetration becomes longer.

The perturbation plots also illustrate that all the weld profile characteristics but the weld width decrease if the defocus distance changes from zero to positive and negative values. The laser beam transfer characteristics reveal that the laser beam has the smallest spot diameter in the focal plane, which causes the highest energy density input into material. As a result, the deepest weld penetration, the longest radial penetration and the resistance length are achieved when the focused (D = 0) beam is used as shown in the Fig. 3.1(b)-(d) and 5.8. When the laser beam is focused above weld plane, it diverges gradually while entering into

the material. This results in lower energy input to the weld with a consequent decrease in the weld characteristics length. The effects are found to be somewhat higher when laser is focused below the weld plane. This is because the laser beam, in this case, converges gradually towards focal point and imparts higher amount of energy to the material. This facilitates diffusion of energy into greater depth favoring stronger melting and vaporization. However, the weld width increases with the variation in defocus distance from its positive to negative values [Fig. 5.3(a)]. This is due to the facts that negative defocused beam imposes higher energy to the weld material than positive defocused one, and the laser spot size increases sharply when its negative focal point distance exceeds the Rayleigh length as stated in [13].

The contour plots shown in the Fig. 5.4(a)-(d) demonstrate the facts that interactions of higher laser power and slower welding speed result in wider weld width; deeper weld penetration; larger radial penetration; and longer resistance length.

### 5.3.1.2 Weld shearing force

The perturbation plot shown in the Fig. 5.5(a) depicts that the weld shearing force increases with the laser power whereas decreases with the welding speed and the beam incident angle.  It also decreases as the defocus distance varies from zero to positive and negative values. This is because of the linear, positive relationship between the weld shearing force and the resistance length that can be observed in the Fig. 5.5(b).
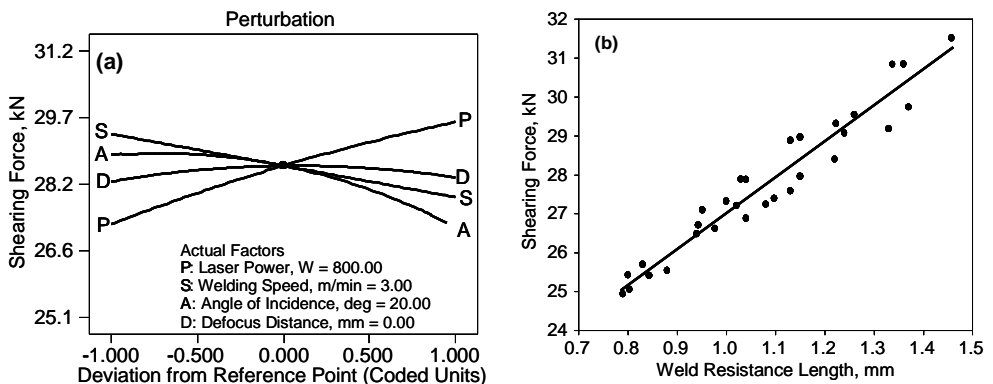


Fig. 5.5: (a) perturbation plot showing effect of all factors on weld shearing force and (b) relationship between weld shearing force and resistance length.

The contour plots, as illustrated in the Figs 5.4(d) and 5.5(a), show that higher laser power with slower welding speed results in longer weld resistance length with a consequent increase in shearing force. As shown in the Fig. 5.6(a)-(c), it is possible to make a weld with similar shearing force for lower laser power and faster welding speed by adjusting the focused beam to the smallest possible incident angle.
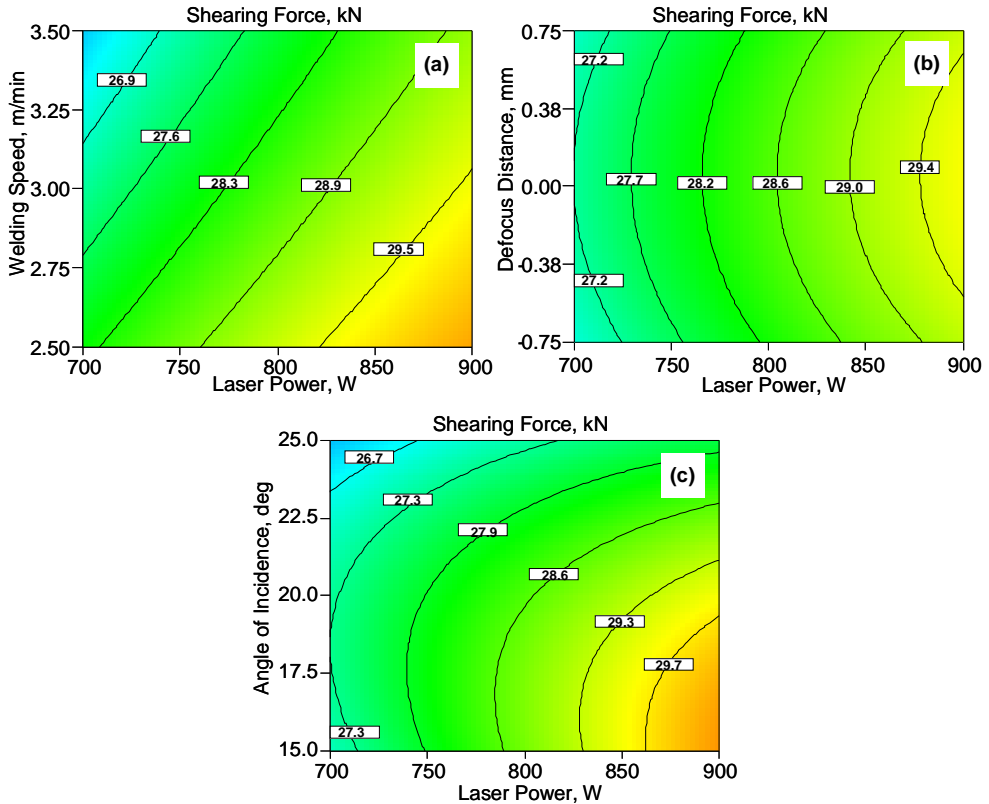
Fig. 5.6: Contour graphs to show the interaction effects of (a) P and S, (b) D and P, and (c) A and P on weld shearing force.

### 5.3.2 Effects of line energy

#### 5.3.2.1 Weld bead geometry

The Figs 5.7 and 5.8 indicate that the weld penetration depth and the radial penetration have linear, positive relationships with the line energy input. The weld resistance length, on the other hand, varies nonlinearly with it. These facts can be attributed to the existing linear and nonlinear interaction effects of laser power and welding speed as illustrated in Figs 5.4(b)-(d). Khan et al. [14] also show this linear dependence of weld penetration depth on energy input for welding martensitic stainless steels in an overlap joint design. The change in weld resistance length is more pronounced for the beam incident angle than the defocus distance. These variations are due to the establishment of different modes of laser welding with different ranges of line energy input.

The results also clearly show that lower line energy input is needed to achieve the same weld penetration depth and resistance length when the laser beam is focused on the weld plane. An increase in beam incident angle intensifies the impact of energy input on weld radial penetration. Besides, any added energy input with a smaller beam incident angle results in deeper penetration depth and longer resistance length of the weld.

Fig. 5.7: Effect of line energy on weld (a) penetration depth, (b) radial penetration, (c) resistance length for different incident angles (A) at D = 0.0 mm.
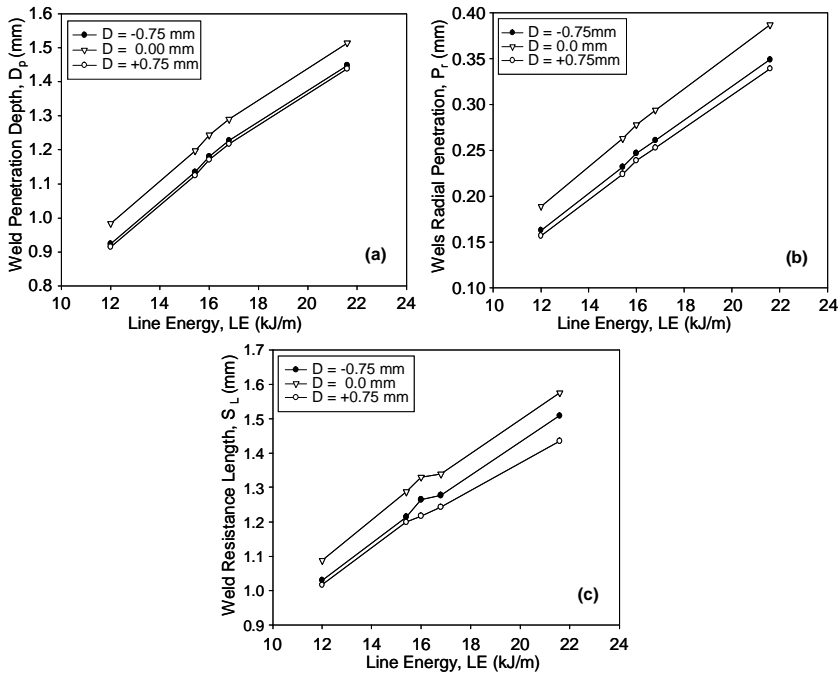


Fig. 5.8: Effect of line energy on weld (a) penetration depth, (b) radial penetration, (c) resistance length for different defocus distance (D) at A = 20°.

The Fig. 5.9(a)-(b) shows the effects of line energy on the weld zone width. Since higher energy input leads to larger volume of melted materials, the weld width tends to increase with line energy input at the welded zone. Small change in weld width for different defocus distance and angle of incidence confirms the fact that these factors have an insignificant impact on it.
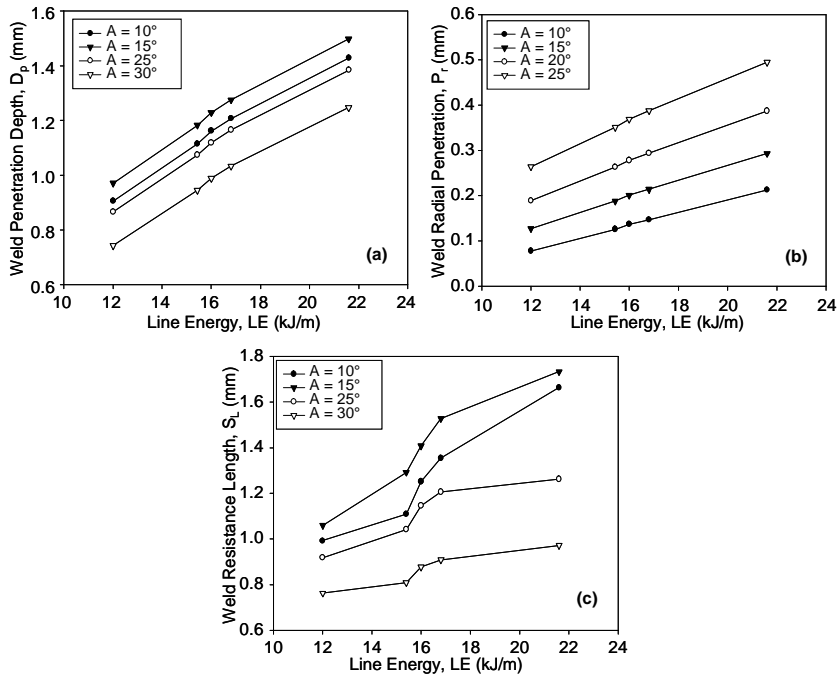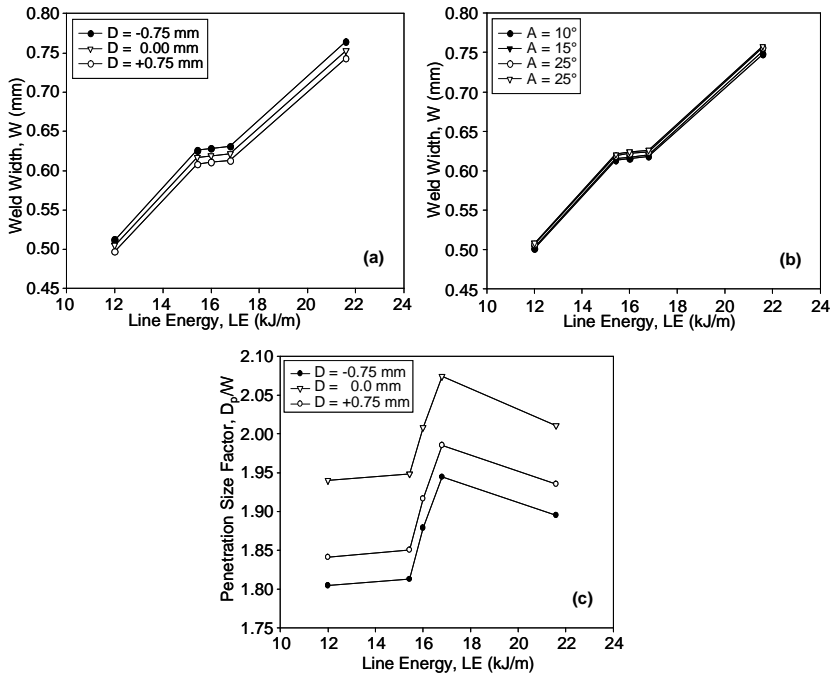


Fig. 5.9: Effect of line energy on weld width for different (a) defocus distance (D) at A = 20°, (b) angle of incidence (A) at D = 0.0 mm, and (c) effect of line energy on penetration size factor for different defocus distance at A = 20°.

For line energy in the range of 12-15kJ/m, as illustrated in the Fig. 5.9(a)-(c), there is a rapid growth in weld width (W) with energy input, whereas change in shape factor ($D_p$/W) is negligible. Slight positive variations in weld shape factor prove that the laser welding is mainly conduction limited. Since the melt pool geometry depends on energy intensity, uniform conduction occurring in all directions usually results in semi-circular weld profile. However, the heat conduction along the beam axis becomes dominant with the increase in energy input and weld shape changes from semi-circular to parabolic.

There is almost no change in weld width when the line energy is in the range of 15-17kJ/m. Nonetheless, a sharp rise (starting from 15kJ/m) in $D_p$/W demonstrates the fact that the weld penetration depth increases at a faster rate than the weld width in this range and establishes a keyhole formation regime. As a result, the weld bead becomes almost cylindrical. Weld shape factor decreases with further increase in line energy. This is due to the creation of upper keyhole plasma plume that acts as a point heat source above weld plane. This generated plasma plume acts in the keyhole and forms a 'chalice' shaped weld bead profile when energy input is more than 17kJ/m. Variation in weld shape factor for

different laser welding modes is also illustrated pictorially as well as schematically in Fig. 5.10.
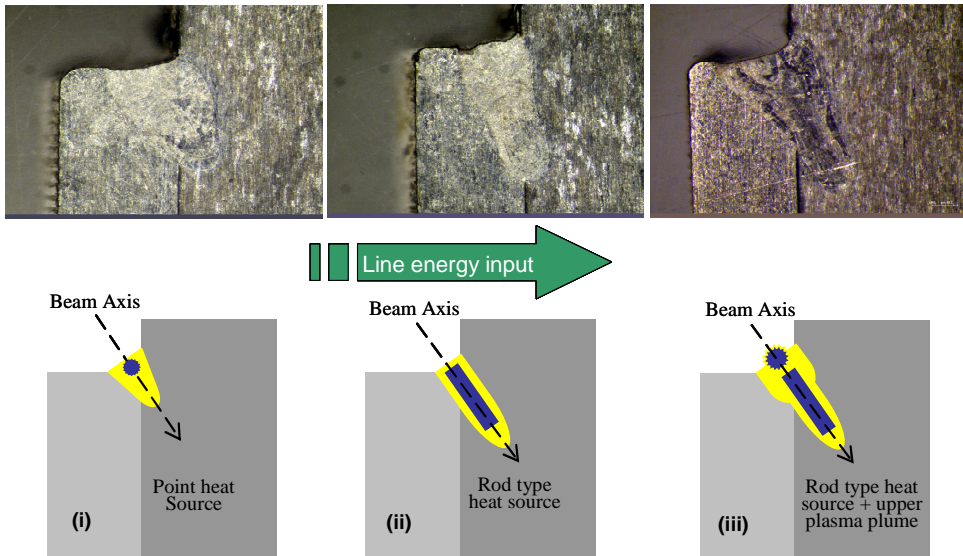


Fig. 5.10: Pictural and schematic views showing the change in shape factor with LE (i) conduction limited (12-<15kJ/m), (ii) keyhole formation (15-17kJ/m), and (iii) keyhole with upper plasma plume (>17kJ/m)
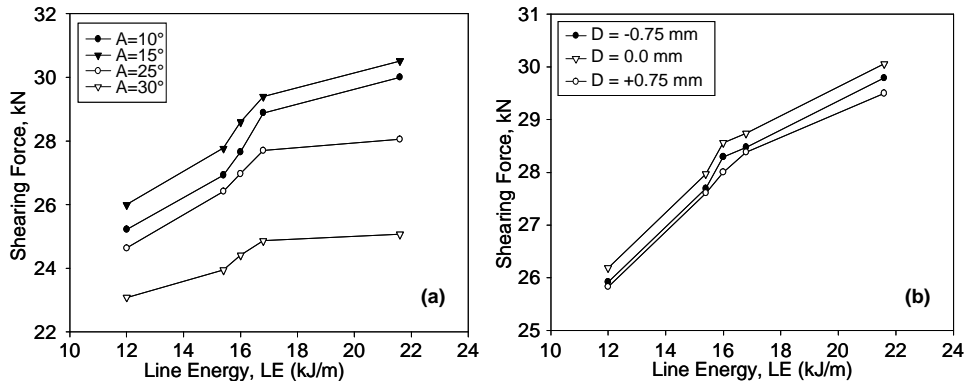


Fig. 5.11: Effect of line energy on weld shearing force for different (a) angle of incidence (A) at D = 0.0 mm, and (b) defocus distance (D) at A = 20°.

### 5.3.2.2 Weld shearing force

As illustrated in the Fig. 5.11(a)-(b), the weld shearing force increases sharply with the increased line energy input in the range of 15-17 kJ/m. This phenomenon can be described as a function of weld resistance length. It is worthmentioning that this resistance length increases rapidly within this range due to the establishment of a keyhole regime, and is linearly related to the resisting force to shear along the weld interface as can be seen in the Figs 5.7(c) and 5.5(b) respectively. Though their relationship shows a linear trend, dispersion of data

from empirical straight line in Fig. 5.5(b) points out that failure due to shear might depend on microstructure formation and its alignment along the resisting section, which needs further investigation.

### 5.3.3 Angular distortion

Laser welding of two coaxial inner and outer tubes in fillet joint configuration often results in misalignment with a consequent adverse effect on the performance of a fuel injector. The resulted misalignments that determine the angular distortion need to be checked and measured. A specialized run-out setup shown in Fig. 5.12 is used for this purpose. Each welded specimen is mounted on the workpiece holder and rotated with the manual rotary motion mechanism. The total misalignment caused by the laser welding is measured by placing a displacement sensor at the top of the specimen. The values thus obtained for all the welded samples are observed to be random in the range of 25-250 µm. It is found that the angular distortion calculated is in the range of 0.06°- 0.35° only, which is much lesser than the allowable limit.
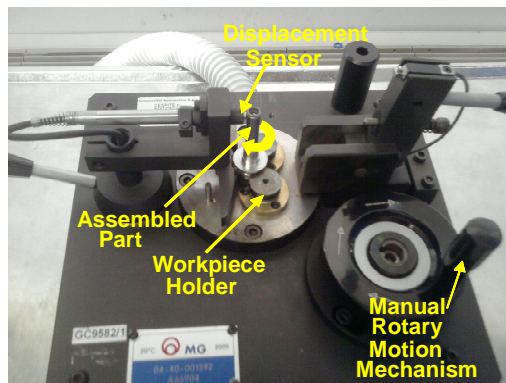


Fig. 5.12: Photographic view of the angular distortion test setup
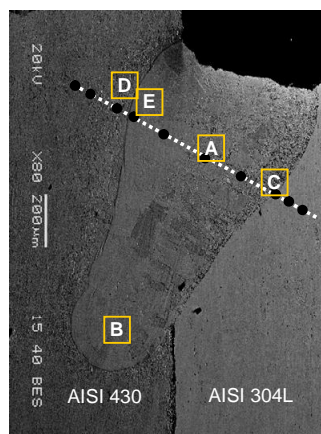


Fig. 5.13: Typical micrograph of laser welding of ferritic AISI 430 and austenitic AISI 304L stainless steels.

### 5.3.4 Weld microstructures

The particular sample, as shown in the Fig. 5.13, is selected for metallurgical analyses as it ensures the minimum design criteria for the weld geometry and mechanical properties. The analyses are carried out with a view to study the microstructures that typically form at various locations of the fusion zone and the heat affected zones in the weld. The selected specimen is welded with a focused beam for the line energy input and the beam incident angle of 15.4 kJ/m and 25° respectively.

The Fig. 5.14(a) shows that the fusion zone microstructure mostly consists of primary ferrite dendrites with an interdendritic layer of austenite. This austenite forms through a peritectic-eutectic reaction and exists at the ferrite solidification boundaries at the end of solidification. Some lathy ferrite morphology is also observed in this zone. This is due to restricted diffusion during ferrite-austenite transformation that results in a residual ferrite pattern.
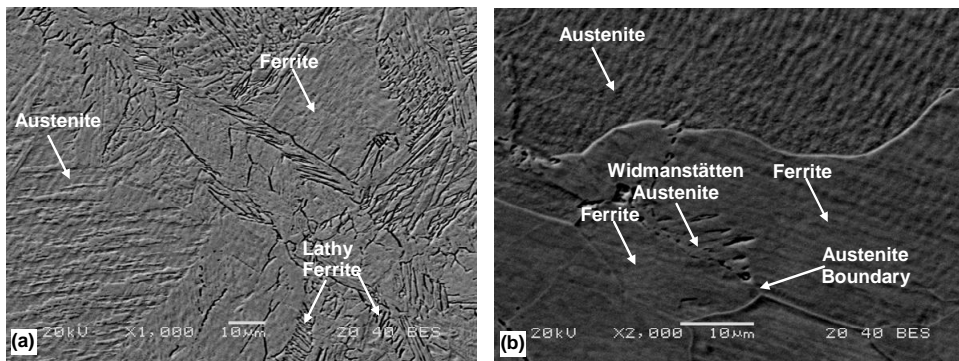


Fig. 5.14: Formation of microstructure in the fusion zone area indicated as (a) A and (b) B in the Fig. 5.13

The Fig. 5.14(b) confirms that developed microstructures are a mixture of austenite and ferrite where Widmanstätten austenite nucleates from austenite along ferrite grain boundary. This is because solidification occurs as ferrite and no austenite forms at the end of solidification at this zone. As a result, this ferrite remains stable in the solid state at the elevated temperature. Austenite initially forms at the ferrite grain boundary when the ferrite structure cools below its solvus temperature. However, the transformation front breaks down and parallel needles of austenite form within the ferrite.

Fusion zone (FZ2) microstructures, as illustrated in the Fig. 5.15, consist of austenite with ferrite along the solidification sub-grain boundaries. This is because, during solidification, sufficient ferrite-promoting elements (particularly Cr) partition towards the solidification boundaries to promote the formation of ferrite as a terminal solidification product. The redistribution of principal alloying elements is reported in Table 5.4. The ferrite that forms along the boundary is relatively stable and resists transformation to austenite during weld cooling since it is already enriched in ferrite promoting elements. This solidification mode is termed as Type AF (Austenite-Ferrite) because it is associated with primary

austenite solidification, where austenite is the first phase to form on solidification and ferrite forms at the end of the solidification process via an eutectic reaction.
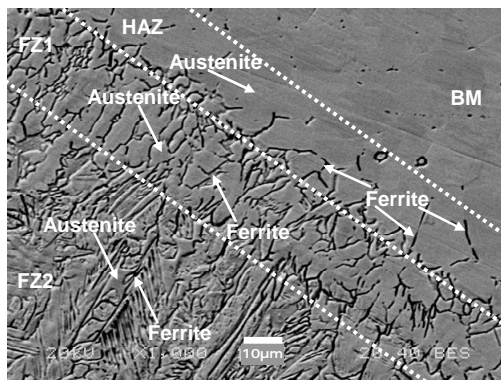


Fig. 5.15: Microstructures of as-supplied base metal, HAZ and fusion zone indicated as C in the Fig. 5.13.

Microstructures, however, show distinct solidification structures (cells and dendrites) near the HAZ (FZ1) as these are fully austenitic at the end of solidification and remains austenite upon cooling to room temperature. This characteristic of solidification is due to the formation of primary austenite, the segregation of alloying and impurity elements that occur during solidification, and the relatively low diffusivity of these elements in the elevated temperature, which preserves the segregation profile that develops during solidification. Some ferrite also forms along the austenite grain boundary in the heat affected zone, which restrict the grain growth and minimize the susceptibility to HAZ liquation cracking.

Table 5.4: Redistribution of major alloying elements over the weld fusion zone

| Measured area indicated as | Weight percentage of major alloying elements (%Wt) in fusion zone | | | |
|---|---|---|---|---|
| | Cr | Ni | Mn | Fe |
| A | 18.16 | 6.37 | 1.57 | 72.8 |
| B | 18.55 | 3.05 | 1.02 | 77.2 |
| C | 17.76 | 7.16 | 1.95 | 75.6 |
| E | 19.22 | 4.89 | 1.16 | 76.9 |

The Fig 5.16(a)-(b) confirm that the microstructures of the base metal are the mixture of ferrite and carbides. The fusion zone microstructures, however, consist of a continuous layer of martensite along the ferrite grain boundaries and inter-granular $Cr_{23}C_6$ carbide precipitates. Primary solidification occurs solely as ferrite and remains stable over some temperature range at this zone. On cooling, some stable austenite forms and reprecipitation of $Cr_{23}C_6$ carbide occurs inter-granularly at the elevated temperature. Since the laser-welding is a self-quenching process, the austenite distributed normally along the ferrite grain boundaries transforms into martensite as the fusion zone cools rapidly to room temperature.
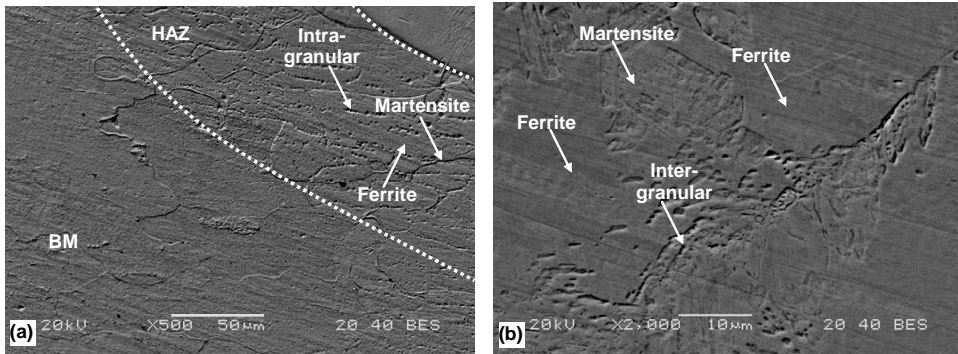
Fig. 5.16: Microstructure of (a) as-supplied base metal and HAZ indicated as D and (b) fusion zone indicated as E in the Fig. 5.13.

As shown in the Fig. 5.16(a), two-phase ferrite and martensite is present in the heat-affected zone. Intra-granular carbide formation is also evident. On cooling, precipitates normally form either inter- or intra-granularly with site based on cooling rate. Intra-granular precipitation typically occurs at high cooling rates while the creation of inter-granular precipitates is due to slow cooling rates.

### 5.3.5 Weld microhardness profile

Fig. 5.17 shows the microhardness profiles of the joint along the line shown in the Fig. 5.13. The specimens selected for studying the change in local microhardness are made for two different beam incident angles. The line energy input and the defocus distance are kept constant during the experiment. The local microhardness of the fusion zone is greater than that of both base metals made of AISI 304L and AISI 430, which might have resulted from the effect of rapid solidification. As shown in the Table 5.4, the microhardness gradient correlates with the gradient of the redistribution of elements Cr, Fe, and Ni. This is a remarkable phenomenon of dissimilar fusion joints.
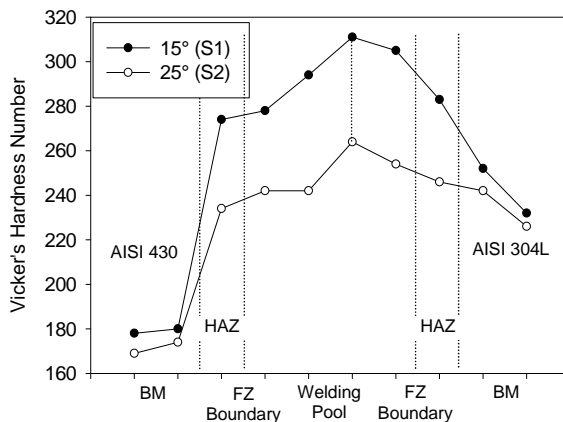


Fig. 5.17: Variation in local microhardness profile for different laser beam incident angles for LE = 15.4 kJ/m and D = 0 mm.

The local microhardness measured at both sides of HAZ is lower than that of the fusion zone and higher than that of the respective base metals. This is due to the rapid solidification as mentioned earlier. Results also demonstrate that local microhardness in the specimen S1 is higher than in the specimen S2. This can be attributed to the intermixture of increased percentage of austenitic stainless steel in the weld volume with the smaller beam incident angle.

## 5.4 CONCLUSIONS

Continuous wave Nd:YAG laser welding has been carried out on the ferritic/austenitic stainless steels. Parametric effects on the weld bead geometry and mechanical properties are investigated. The results can be summarized as follows:

- All the weld characteristics lengths and shearing force increases as laser power increases or welding speed decreases.
- Laser power has the most significant positive effect on all the characteristics lengths except the weld radial penetration. An increase in laser power only intensifies the effect of beam incident angle on radial penetration.
- The focused beam with lower laser power and faster welding speed produces a weld having the same weld geometry and shearing force.
- Beam incident angle is also found as a key factor that determines the weld bead geometry. The weld radial penetration increases significantly with beam incident angle whereas weld penetration depth, resistance length and hence shearing force decrease.
- A rapid increase in weld shape factor and shearing force with the line energy input in the range of 15-17 kJ/m depicts the establishment of a keyhole regime.
- Various, complex austenite–ferrite microstructures are identified in the fusion zone because of solidification behaviour and subsequent solid-phase transformation, which are controlled by composition and cooling rates.
- Formation of some ferrite along the austenite grain boundary in the heat affected zone on austenite side is observed. At the same time, microstructures are composed of two-phase ferrite and martensite with intra-granular carbide on ferrite side.
- Variation in local microhardness observed across the weld depends on the fraction intermix of each base metal and correlates with the redistribution of segregated austenite- and ferrite-promoting elements in the weld.

## REFERENCES

1. Sun, Z., 1996, Feasibility of producing ferritic/austenitic dissimilar metal joints by high energy density laser beam process, International Journal of Pressure Vessels and Piping, 68:153-160.
2. Katayama, S., 2004, Laser welding of aluminium alloys and dissimilar metals, Weld International, 18(8):618–25.
3. Kaiser, E., Schafer, P., 2005, Pulse sharpening optimizes the quality of seam and spot welds. In: Lasers in manufacturing, proceeding of the third international WLT conference on lasers in manufacturing, pp. 695–698.

4. Li, Z., Fontana, G., 1998, Autogenous laser welding of stainless steel to free-cutting steel for the manufacture of hydraulic valves, Journal of Materials Processing Technology, 74:174–182.

5. Mai, T.A., Spowage, A.C., 2004, Characterisation of dissimilar joints in laser welding of steel–kovar, copper–steel and copper–aluminium, Materials Science and Engineering: A, 374:224–233.

6. Liu, X.B., Yu, G., Pang, M., Fan, J.W., Wang, H.H., Zheng, C.Y., 2007, Dissimilar autogenous full penetration welding of superalloy K418 and 42CrMo steel by a high power CW Nd:YAG laser, Applied Surface Science, 253:7281–7289.

7. Berretta, J.R., de Rossi, W., Neves, M.D.M., de Almeida, I.A., Junior, N.D.V., 2007, Pulsed Nd:YAG laser welding of AISI 304 to AISI 420 stainless steels, Optics and Lasers in Engineering, 45:960–966.

8. Mousavi, S.A.A.A., Sufizadeh, A.R., 2009, Metallurgical investigations of pulsed Nd:YAG laser welding of AISI 321 and AISI 630 stainless steels, Materials and Design, 30:3150–3157.

9. Pekkarinen, J., Kujanpää, V., 2010, The effects of laser welding parameters on the microstructure of ferritic and duplex stainless steels welds, Physics Procedia, 5:517–523.

10. Allabhakshi, S., Madhusudhan Reddy, G., Ramarao, V.V., Phani Babu, C., Ramachandran, C.S., 2002, Studies on weld overlaying of austenitic stainless steel (AISI 304) with ferritic stainless steel (AISI 430). In: Proceedings of the national welding conference, Indian Institute of Welding, Chennai, India, Paper 8.

11. Pan, C., Zhang, E., 1996, Morphologies of the transition region in dissimilar austenitic–ferritic welds, Material Characterization, 36(1):5–10.

12. Wang, S. C., Wang, C., Tu, Y. K., Hwang, C. J., Chi, S., Wang, W. H., Cheng, W. H., 1996, Effect of Au coating on joint strength in laser welding for invar-invar packages, Electronic Components and Technology Conference, IEEE, pp. 942-945.

13. Cui, C., Hu, J., Gao, K., Pang, S., Yang, Y., Wang, H., Guo, Z., 2008, Effects of process parameters on weld metal keyhole characteristics with COR2R laser butt welding, Lasers in Engineering, 18:319–327.

14. Khan, M.M.A., Romoli, L., Fiaschi, M., Dini, G., Sarri, F., 2010, Experimental investigation on laser beam welding of martensitic stainless steels in a constrained overlap joint configuration. Journal of Material Processing Technology, 210:1340–53.

# CHAPTER 6

## USING RESPONSE SURFACE METHOD TO LASER WELDING PROCESS OPTIMIZATION FOR FILLET CONFIGURATION

*This chapter presents process parameter optimization for CW Nd:YAG laser welding of ferritic/austenitic stainless steels in a constrained fillet joint configuration using response surface methodology. The tubular shaped specimens considered in this work are made of ferritic AISI430 and austenitic AISI304L with 2.9 ± 0.02 and 1.75 ± 0.02 mm wall thicknesses respectively.*

*Response surface methodology is used to develop a set of mathematical models relating the welding parameters to each of the weld characteristics such as weld penetration depth, radial penetration, resistance length, and shearing force. Statistical and experimental validations of the models developed are checked, and the models are optimized by determining the best combination of input process parameters.*

*Numerical and graphical optimization methods are used in this work by selecting the desired goals for each factor and response. The quality criteria set for the weld to determine the optimal settings of welding parameters are the maximization of weld resistance length and shearing force, and the minimization of weld radial penetration. These optimization criteria are derived from mechanical and geometric requirements of fillet weld joint stated in ISO 15614-11.*

*Whatever the optimization criteria, laser has to be focused on weld plane at an angle around 12° to obtain a weld with longer resistance length, smaller radial penetration, and hence, greater shearing force. Laser power and welding speed in the range of 860–875W and 3.4–4.0 m/min respectively are identified as the optimal set of laser fillet welding parameters to obtain stronger and better welds. The graphical optimization showing the overlay plots are extremely practical for quick technical use in the workshop to choose the values of the welding parameters that would achieve optimal response value for this combination of materials.*

## 6.1 INTRODUCTION

In recent years, interest in the use of laser welding as a joining process in various industrial applications has increased rapidly because of its associated unique features such as the low and precise heat input, small HAZ, deep and narrow FZ, low residual stress and weld distortion and high welding speed [1-2]. These features come from its high power density, which make laser welding one of the available key welding techniques [3-5]. Laser welding being autogenous needs no filler materials resulting in reduction in welding costs and increase in weld quality [6-7]. Generally, welding quality is characterized by the weld bead geometry, which plays an important role in determining the mechanical properties of the weld [8]. To achieve a good weld quality, the influential welding process parameters such as laser beam power, welding speed, focal position, shielding gas, and focused position should be selected and controlled accurately [7, 9-11].

However, the selection of the welding parameters that would produce an excellent welded joint is the main challenge for today's manufacturers. Usually, the desired welding process parameters are determined based on a time consuming trial and error development effort with input parameters. This approach does not ensure that the selected welding parameters result in optimal or near optimal weld pool geometry [8]. Also, the accuracy of process parameters thus selected depends on the skill and the experience of the engineers or machine operators. To predict the welding parameters accurately, without consuming time, materials and labor effort, various optimization methods are available to define the desired output variables. Considering the capabilities of reducing a great number of experimental trials as compared to other approaches and developing mathematical functions to achieve a logical relationship between the input and output parameters, many researchers have been motivated to apply response surface methodology (RSM) for predicting and optimizing the welding process parameters.

Benyounis et al. [12] studied the effect of the main laser welding parameters on the weld-bead profile using RSM to develop appropriate models. Manonmani et al. [13] used RSM to develop mathematical models to predict the geometry of weld bead in butt joint of austenitic stainless steel AISI304 sheets. Elangovan and Balasubramanian [14] developed an empirical relationship to predict tensile strength of friction stir welded joints of AA2219 alloy using RSM. Benyounis et al. [15] employed RSM to relate the laser welding input parameters (laser power, welding speed and focal position) to each of the response outputs (i.e. tensile strength, impact strength and operating cost) and to find out the optimal welding combination that would maximize both the tensile and impact strengths while keeping the cost relatively low. Moradi and Ghoreishi [16] developed statistical models using RSM to investigate the effect of laser butt welding parameters on the geometrical shape of Ni-base super-alloy Rene 80. Padmanaban and Balasubramanian [17] developed an empirical relationship using RSM to predict tensile strength of laser beam welded AZ31B magnesium alloy joint and to find the optimal welding conditions to attain maximum tensile strength. Rajakumar et al. [18] developed mathematical models using RSM to analyze the effect of FSW process parameters and tool parameters on the tensile strength of AA7075 aluminum alloy. Ruggiero et al. [19] studied the CW $CO_2$ dissimilar laser-butt welding of low carbon steel and austenitic steel. They used RSM to relate laser

welding input parameters to response variations and to find the optimal welding combinations.

### 6.1.1 Research objectives

The welding process parameters have apparently very complex relationships with the weld bead geometry determining the mechanical properties of the weld. Welding the dissimilar metals is more complicated than that of similar metals due to difference in the physical, mechanical, and metallurgical properties of the metals to be joined. Laser welding of dissimilar ferritic and austenitic stainless steels in a circular and constrained fillet joint configuration has not been studied and reported yet. This is because this configuration complicates the joint design and inaccurate positioning of the focused beam at the corner can cause its interference with the vertical surface on its way to weld plane and reflection back to the adjacent horizontal surface making the welding process more complex. To solve the problems associated with laser welding of dissimilar ferritic and austenitic stainless steels and to obtain welds with adequate properties, it is essential to precisely select and control the welding processes and the process parameters. This paper will, therefore, try to find the optimal conditions for Nd:YAG laser beam welding of ferritic AISI430 and austenitic AISI304L stainless steels in fillet joint configuration. The following points summarize the main objectives of this research:

- Application of response surface approach to develop mathematical models for the above mentioned dissimilar materials to predict and optimize the following process responses:
  - ✓ Weld-bead geometry e.g. weld penetration depth, radial penetration, resistance length and
  - ✓ weld mechanical property e.g. shearing force
- Graphical presentation of the developed models graphically to illustrate the effect of significant model terms and their interactions on the above mentioned responses.
- Application of the analysis of variances (ANOVA) and other adequacy measures to test adequacy of the developed models and examine each term in the developed models using statistical significance tools. Also, conducting some tests for experimental validations of the developed models.
- Determination of the optimal combinations of input welding parameters (laser power, welding speed, laser beam incident angle, and defocus distance), using the developed models with numerical optimization and graphical optimization, to maximize both the weld resistance length and shearing force and minimize the weld radial penetration.

### 6.2 MATERIALS AND METHODS

### 6.2.1 Materials

Two tubular-shaped parts of ferritic AISI430 and austenitic AISI304L stainless steels are fillet welded in a circular configuration to produce the welded joint. The selection of this material combination is based on both technical and economical reasons as they can provide satisfactory service performance and considerable savings, and also on their frequent use in welded form in automotive industries for

making various types of fuel injectors. The chemical compositions of the base metals and the weld bead characteristics are shown in Table 6.1 and Fig. 6.1 respectively. In this study, inner (IT) and outer (OT) tubes with 2.9 ± 0.02 and 1.75 ± 0.02 mm wall thicknesses respectively are first assembled together so that there is a clearance between them and then fillet welded autogenously.

Table 6.1: Chemical compositions of base metals of the weld

| Base Metals | Chemical Compositions (%Wt) | | | | | | |
|---|---|---|---|---|---|---|---|
| | C | Cr | Ni | Mn | P | S | Si |
| AISI 304L | 0.03 | 18.0-20.0 | 8.0-12.0 | 2.0 | 0.45 | 0.03 | 1.0 |
| AISI 430 | 0.12 | 16.0-18.0 | 0.75 | 1.0 | 0.04 | 0.03 | 1.0 |
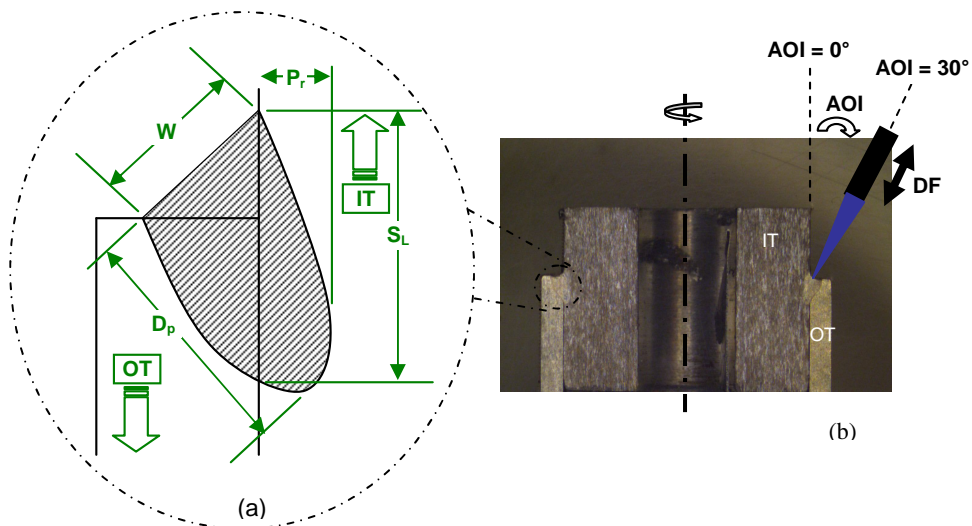


Fig. 6.1: Diagrams showing (a) bead characteristics of a welded fillet joint, and (b) adopted laser-welding procedure.

### 6.2.2 Response surface methodology (RSM)

Response surface methodology (RSM) is a collection of mathematical and statistical techniques that are useful for modeling and analyzing engineering problems. In this technique, the main objective is to optimize (maximize or minimize or equal to a specific target value) the response surface that is influenced by various process parameters [20]. Fundamental to RSM is the model(s) that specify the relationships among one or more measured responses and a number of accurately controllable predictors, or input factors [21]. If all the independent variables are measurable, continuous, and controllable by experiments with negligible errors, the response surface can be expressed by

$$y = f(\chi_1, \chi_2 \ldots \ldots \chi_k) \tag{1}$$

where $y$ is the response of the system; $f$ is the true response function whose form is unknown and perhaps very complicated; $\chi_i$ is the variable of action called factor; and $k$ is the number of independent variables.

In order to optimize the response '$y$', it is, therefore, essential to find a suitable approximation for the true functional relationship between the independent variables and the response surface [22]. The postulated mathematical model used with response surface designs is typically a second degree model with second-order interactions [15] as given below:

$$y = b_o + \sum_{i=1}^{k} b_i \chi_i + \sum_{i=1}^{k} b_{ii} \chi_i^2 + \sum_{i<j} \sum_{j=2}^{k} b_{ij} \chi_i \chi_j + \varepsilon \tag{2}$$

where $b_{ii}$ = 0,1,......k are called the regression coefficients, and $\varepsilon$ is usually treated as a statistical error, which is often assumed to be independent with N(0, $\sigma^2$) distributions.

The **b** coefficients, which should be determined in the second order model, are obtained by the least squares method. In general Eq. (2) can be written in matrix form:

$$\boldsymbol{Y} = \boldsymbol{b}\boldsymbol{X} + \varepsilon \tag{3}$$

where **Y** is defined to be a matrix of measured values and **X** to be a matrix of independent variables. The matrices **b** and **ε** consist of coefficients and errors, respectively. The solution of Eq. (3) can be obtained by the matrix approach:

$$\boldsymbol{b} = (\boldsymbol{X}^T \boldsymbol{X})^{-1} \boldsymbol{X}^T \boldsymbol{Y} \tag{4}$$

The coefficients, i.e. the main effect ($b_i$) and two-factor interactions ($b_{ij}$) can be estimated from the experimental results by applying a least squares method.

## 6.2.3 Experimental design

A four factor five levels central composite rotatable experimental design with full replication is planned to conduct the experiments. The statistical software Design-Expert V7 is used to create the design matrix and analyze the experimental data. The laser-welding input variables are laser power (P), welding speed (S), angle of incidence (A), and defocus distance (D). In order to find out the range of each process input parameter, initial trial runs are carried out by changing one of the process parameters whilst keeping the rest of them at constant values. The stringent weld quality requirements stated in ISO 13919-1 i.e. absence of visible defects, size and position of weld spatter, and smooth appearance of welded surface are considered as the selection criteria for the working range of each input factor. Table 6.2 shows primary input factors, their corresponding coded and actual levels, and response factors considered.

Response surface methodology (RSM) is applied to the experimental data using the same software to develop mathematical models relating the selected welding parameters to each of the four output responses of the weld (weld penetration depth, radial penetration, resistance length, and shearing force). The adequacies of the models developed and their significant terms are measured by analyzing variance and other adequacy measures. Finally, these mathematical models are used to determine the optimal settings of welding parameters to ensure the desired

weld quality. In this study, the quality criteria defined for the weld to determine the optimal settings of welding parameters are the minimization of weld radial penetration, and the maximization of weld resistance length and shearing force. These optimization criteria are derived from mechanical and geometric requirements of fillet weld joint stated in ISO 15614-11.

Table 6.2: Experimental conditions and response factors

| Process Factors | Symbols | limits | | | | |
|---|---|---|---|---|---|---|
| | | -2 | -1 | 0 | +1 | +2 |
| Laser power (W) | P | 600 | 700 | 800 | 900 | 1000 |
| Welding speed (m/min) | S | 2.0 | 3.5 | 3.0 | 3.5 | 4.0 |
| Angle of incidence (°) | A | 10 | 15 | 20 | 25 | 30 |
| Defocus Distance (mm) | D | -1.5 | -0.75 | 0 | +0.75 | +1.5 |

Constant Factors

| Base material | : | Outer Tube | : AISI 304L |
|---|---|---|---|
| | | Inner Tube | : AISI 430 |
| Laser source | : | Continuous Wave Nd:YAG Laser | |
| Shielding gas | : | Type | : Argon |
| | | Flow rate | : 29 l/min |

Response Factors

| Weld bead characteristics | : | Weld penetration depth ($D_p$), radial penetration ($P_r$), and resistance length ($S_L$) |
|---|---|---|
| Weld mechanical Properties | : | Weld shearing force |
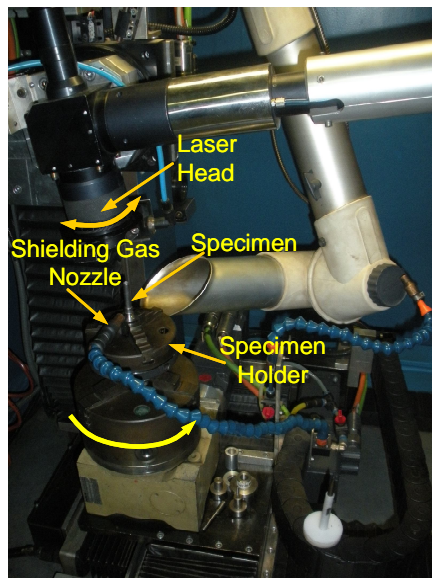


Fig. 6.2:  Photographic view of Nd:YAG laser-welding system

### 6.2.4 Experimental work

Thirty experimental runs are carried out according to the design matrix in a random order to avoid any systematic error creeping into the system. Specimens were welded circularly in a fillet joint configuration using a 1.1 kW continuous wave Nd: YAG laser (Rofin DY011). During experimentation, laser power, welding speed, defocus distance, and incident angle are varied in the range 800–1100W, 4.5–7.5 m/min, -1.5- +1.5 mm, and 10°-30° respectively. The optical system consisted of a 300 μm fiber and two lenses of 200 mm focal and collimating lengths is able to deliver the laser with a minimum focal spot diameter of 300 μm. Argon is used as shielding gas with constant flow rate of 29 l/min to protect heated surface from oxidation and suppress plasma during welding. A standard washing procedure practised in the automotive industries is followed to clean, cool and dry the specimens. None of the samples are subjected to any form of heat treatment after laser welding. Photographic view of the experimental set-up for laser welding has been shown in Fig. 6.2.

### 6.2.5 Mechanical characterization

After welding, each of specimens is first visually inspected and then cut axially to obtain transverse section of the welds under various welding conditions. Finally, part of the cut surfaces is prepared for metallographic inspection by polishing and etching to display a bead shape. The bead shape measurements are made using an optical microscope (Leica MZ125) with an image analysis system (Leica IM500). Three pairs of coaxially assembled parts are welded for each combination of laser-welding parameters to ensure statistical accuracy. The average value of each of the measured response factors is determined and recorded for further analyses. Push-out tests are performed to measure the shearing strength of the weld.
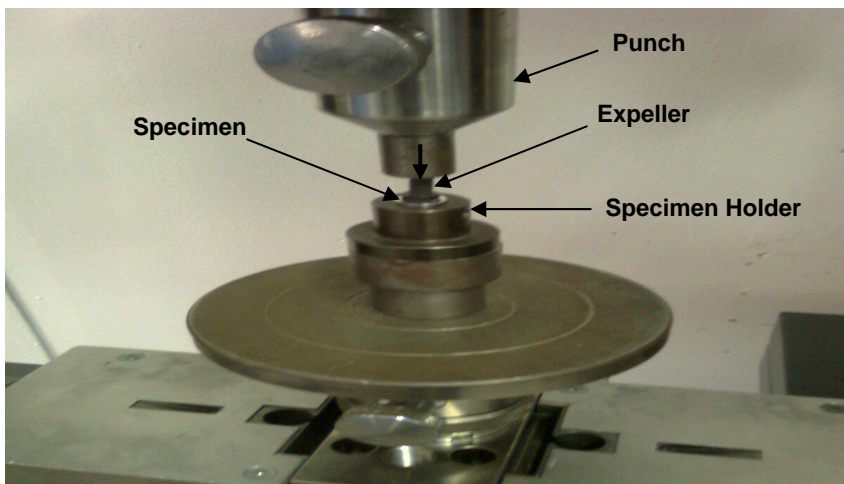


Fig. 6.3: Photographic view of the experimental setup for push out test

Push out tests are accomplished at room temperature(22.1°C) using Instron push-out calibrated press (model 3367) to determine the shearing load to failure of the

welds fabricated under various conditions. During shearing test, as shown in Fig. 6.3, specimens are placed on a specimen holder or vice and pushed axially by a specially designed expeller so that the specimen fails due to shear along the resistance section of the weld. Table 6.3 shows the design matrix with actual factors and measured mean responses.

Table 6.3: Design matrix with actual factors and measured mean responses

| Process Factors | | | | Response Factors | | | |
|---|---|---|---|---|---|---|---|
| P (W) | S (m/min) | A (deg) | D (mm) | $S_l$ (mm) | Pr (mm) | $D_p$ (mm) | $F_s$ (kN) |
| 700 | 2.5 | 15 | -0.75 | 1.130 | 0.160 | 1.064 | 28.98 |
| 900 | 2.0 | 15 | -0.75 | 1.337 | 0.240 | 1.368 | 30.84 |
| 700 | 3.5 | 15 | -0.75 | 0.843 | 0.094 | 0.857 | 25.01 |
| 900 | 3.5 | 15 | -0.75 | 1.223 | 0.173 | 1.137 | 28.32 |
| 700 | 2.5 | 25 | -0.75 | 0.943 | 0.353 | 1.123 | 27.01 |
| 900 | 2.5 | 25 | -0.75 | 1.150 | 0.466 | 1.390 | 28.56 |
| 700 | 3.5 | 25 | -0.75 | 0.803 | 0.273 | 0.883 | 24.95 |
| 900 | 3.5 | 25 | -0.75 | 0.977 | 0.387 | 1.189 | 26.41 |
| 700 | 2.5 | 15 | 0.75 | 1.097 | 0.167 | 1.203 | 27.59 |
| 900 | 2.5 | 15 | 0.75 | 1.457 | 0.293 | 1.457 | 31.32 |
| 700 | 3.5 | 15 | 0.75 | 0.880 | 0.130 | 0.990 | 25.54 |
| 900 | 3.5 | 15 | 0.75 | 1.330 | 0.200 | 1.240 | 29.28 |
| 700 | 2.5 | 25 | 0.75 | 0.940 | 0.320 | 0.980 | 26.48 |
| 900 | 2.5 | 25 | 0.75 | 1.040 | 0.430 | 1.320 | 27.78 |
| 700 | 3.5 | 25 | 0.75 | 0.790 | 0.200 | 0.810 | 24.93 |
| 900 | 3.5 | 25 | 0.75 | 0.952 | 0.316 | 1.093 | 27.09 |
| 600 | 3.0 | 20 | 0.00 | 0.830 | 0.140 | 0.890 | 25.69 |
| 1000 | 3.0 | 20 | 0.00 | 1.370 | 0.380 | 1.590 | 29.54 |
| 800 | 2.0 | 20 | 0.00 | 1.360 | 0.350 | 1.470 | 30.85 |
| 800 | 4.0 | 20 | 0.00 | 1.040 | 0.200 | 1.030 | 26.88 |
| 800 | 3.0 | 10 | 0.00 | 1.030 | 0.140 | 1.120 | 27.89 |
| 800 | 3.0 | 30 | 0.00 | 0.800 | 0.475 | 0.989 | 25.42 |
| 800 | 3.0 | 20 | -1.50 | 1.260 | 0.150 | 0.968 | 29.55 |
| 800 | 3.0 | 20 | 1.50 | 1.021 | 0.130 | 0.987 | 27.21 |
| 800 | 3.0 | 20 | 0.00 | 1.220 | 0.240 | 1.270 | 28.19 |
| 800 | 3.0 | 20 | 0.00 | 1.080 | 0.340 | 1.250 | 27.24 |
| 800 | 3.0 | 20 | 0.00 | 1.000 | 0.270 | 1.200 | 27.32 |
| 800 | 3.0 | 20 | 0.00 | 1.130 | 0.290 | 1.260 | 27.18 |
| 800 | 3.0 | 20 | 0.00 | 1.150 | 0.300 | 1.240 | 28.96 |
| 800 | 3.0 | 20 | 0.00 | 1.240 | 0.220 | 1.260 | 29.07 |

### 6.2.6 Optimization procedure

The optimization part in Design-Expert software V7 searches for a combination of factor levels that simultaneously satisfy the requirements placed (i.e. optimization criteria) on each of the responses and process input factors (i.e. multiple-response optimization). Numerical and graphical optimization methods are used in this work by selecting the desired goals for each factor and response. The numerical optimization process involves combining the goals into an overall desirability

function (D). The numerical optimization feature in the design-expert package finds one point or more in the factors domain that maximizes this objective function. In a graphical optimization with multiple responses, the software defines regions where requirements simultaneously meet the proposed criteria. Also, superimposing or overlaying critical response contours can be defined on a contour plot. Then, a visual search for the best compromise becomes possible. The graphical optimization displays the area of feasible response values in the factor space. Regions that fit the optimization criteria are colored [23]. Fig. 6.4 shows flow chart of the optimization steps as developed [15].
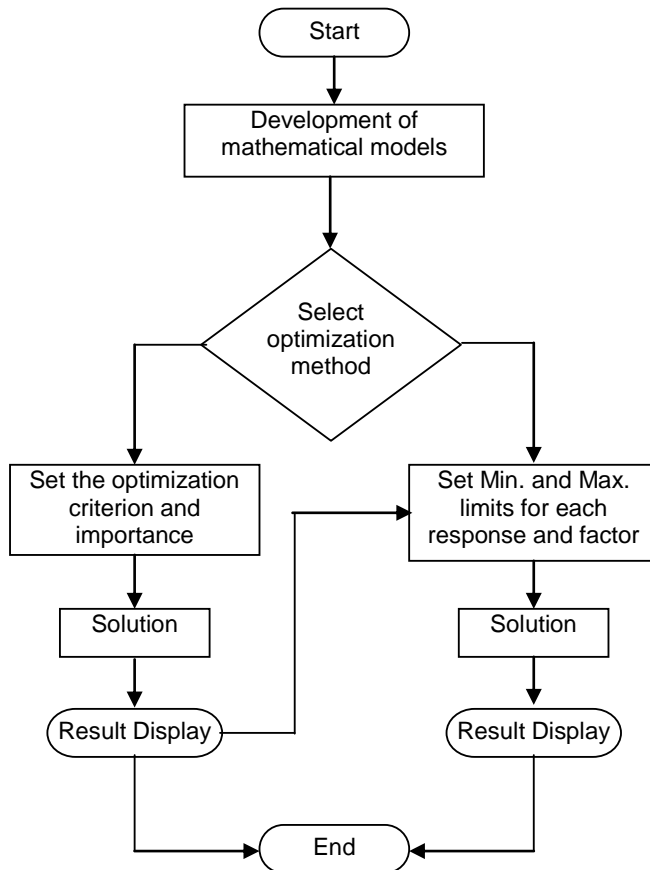


Fig. 6.4: Flow chart of optimization step

## 6.3 RESULTS AND DISCUSSION

### 6.3.1 Development of mathematical models

At this stage, the fit summary statistics is used to select the models that best describe the response factors. The fit summary includes sequential model sum squares to select the highest order polynomial where additional terms are significant and the model is not aliased. In addition, model summary statistics of the fit summary focuses on the model that maximizes adjusted R-squared and

predicted R-squared values. The sequential F-test and lack-of-fit test are carried out using the same statistical software package to check if the regression model is significant and to find out the significant model terms of the developed models as well. The step-wise regression method is also applied to eliminate the insignificant model terms automatically.

### 6.3.1.1 Response model selection

Suitable response models for the response factors are selected based on the fit summaries. From fit summary output of the measured responses shown in Tables 6.3 – 6.10, it is evident that quadratic model shown in Eq. (2) is statistically fitted to the experimental data to obtain the regression equations for all responses and can, therefore, be used for further analysis.

Table 6.3: Sequential model sum of squares for weld penetration depth

| Source | Sum of Squares | df | Mean Square | F Value | p-value Prob > F | |
|---|---|---|---|---|---|---|
| Mean | 39.97 | 1 | 39.97 | | | |
| Linear | 0.870 | 4 | 0.220 | 23.47 | < 0.0001 | |
| 2FI | 0.046 | 6 | 0.0076 | 0.78 | 0.5952 | |
| Quadratic | 0.170 | 4 | 0.044 | 59.14 | < 0.0001 | Suggested |
| Cubic | 0.007 | 8 | 0.0009 | 1.56 | 0.2846 | Aliased |

Table 6.4: Model summary statistics for weld penetration depth

| Source | Std. Dev. | $R^2$ | Adj. $R^2$ | Pred. $R^2$ | PRESS | |
|---|---|---|---|---|---|---|
| Linear | 0.096 | 0.7897 | 0.7560 | 0.6956 | 0.34 | |
| 2FI | 0.099 | 0.8313 | 0.7425 | 0.7156 | 0.31 | |
| Quadratic | 0.027 | 0.9899 | 0.9806 | 0.9543 | 0.050 | Suggested |
| Cubic | 0.024 | 0.9964 | 0.9850 | 0.8854 | 0.13 | Aliased |

Table 6.5: Sequential model sum of squares for weld radial penetration

| Source | Sum of Squares | df | Mean Square | F Value | p-value Prob > F | |
|---|---|---|---|---|---|---|
| Mean | 2.04 | 1 | 2.040 | | | |
| Linear | 0.27 | 4 | 0.0670 | 29.96 | < 0.0001 | |
| 2FI | 0.0093 | 6 | 0.0015 | 0.63 | 0.7041 | |
| Quadratic | 0.034 | 4 | 0.0085 | 10.12 | 0.0004 | Suggested |
| Cubic | 0.0015 | 8 | 0.0019 | 0.12 | 0.9964 | Aliased |

Table 6.6: Model summary statistics for weld radial penetration

| Source | Std. Dev. | $R^2$ | Adj. $R^2$ | Pred. $R^2$ | PRESS | |
|---|---|---|---|---|---|---|
| Linear | 0.047 | 0.8274 | 0.7998 | 0.7468 | 0.082 | |
| 2FI | 0.050 | 0.8561 | 0.7803 | 0.7749 | 0.073 | |
| Quadratic | 0.029 | 0.9611 | 0.9248 | 0.9005 | 0.032 | Suggested |
| Cubic | 0.040 | 0.9657 | 0.8578 | 0.1722 | 0.27 | Aliased |

Table 6.7: Sequential model sum of squares for weld resistance length

| Source | Sum of Squares | df | Mean Square | F Value | p-value Prob > F | |
|---|---|---|---|---|---|---|
| Mean | 34.48 | 1 | 34.48 | | | |
| Linear | 0.69 | 4 | 0.170 | 16.70 | < 0.0001 | |
| 2FI | 0.054 | 6 | 0.009 | 0.83 | 0.5613 | |
| Quadratic | 0.12 | 4 | 0.030 | 5.56 | 0.0068 | Suggested |
| Cubic | 0.034 | 8 | 0.004 | 0.61 | 0.7493 | Aliased |

Table 6.8: Model summary statistics for weld resistance length

| Source | Std. Dev. | $R^2$ | Adj. $R^2$ | Pred. $R^2$ | PRESS | |
|---|---|---|---|---|---|---|
| Linear | 0.10 | 0.7357 | 0.6917 | 0.6071 | 0.37 | |
| 2FI | 0.10 | 0.7931 | 0.6781 | 0.4911 | 0.48 | |
| Quadratic | 0.073 | 0.9200 | 0.8401 | 0.6983 | 0.28 | Suggested |
| Cubic | 0.083 | 0.9558 | 0.7937 | | + | Aliased |

+ Case(s) with leverage of 1.00: PRESS statistic is not defined

Table 6.9: Sequential model sum of squares for weld shearing force

| Source | Sum of Squares | df | Mean Square | F Value | p-value Prob > F | |
|---|---|---|---|---|---|---|
| Mean | $4.34 \times 10^{-6}$ | 1 | $4.34 \times 10^{-6}$ | | | |
| Linear | $7.92 \times 10^{-9}$ | 4 | $1.98 \times 10^{-9}$ | 23.63 | < 0.0001 | |
| 2FI | $5.68 \times 10^{-10}$ | 6 | $9.46 \times 10^{-11}$ | 1.18 | 0.3593 | |
| Quadratic | $7.15 \times 10^{-10}$ | 4 | $1.79 \times 10^{-10}$ | 3.30 | 0.0395 | Suggested |
| Cubic | $2.78 \times 10^{-10}$ | 8 | $3.47 \times 10^{-11}$ | 0.45 | 0.8542 | Aliased |

Table 6.10: Model summary statistics for weld shearing force

| Source | Std. Dev. | $R^2$ | Adj. $R^2$ | Pred. $R^2$ | PRESS | |
|---|---|---|---|---|---|---|
| Linear | $9.15 \times 10^{-6}$ | 0.7908 | 0.7574 | 0.6975 | $3.03 \times 10^{-9}$ | |
| 2FI | $8.96 \times 10^{-6}$ | 0.8475 | 0.7673 | 0.6916 | $3.09 \times 10^{-9}$ | |
| Quadratic | $7.36 \times 10^{-6}$ | 0.9190 | 0.8433 | 0.7080 | $2.92 \times 10^{-9}$ | Suggested |
| Cubic | $8.74 \times 10^{-6}$ | 0.9467 | 0.7790 | 0.7112 | $1.91 \times 10^{-8}$ | Aliased |

## 6.3.1.2 Analysis of variance (ANOVA)

The test for significance of the regression models and the test for significance on individual model coefficients are performed using the same statistical package. By selecting the step-wise regression method that eliminates the insignificant model terms automatically, the resulting ANOVA Tables 6.11-6.14 for the selected models summarize the analysis of variance of each response and illustrate its significant model terms as well. The aforestated tables demonstrate that calculated Fisher's 'Model-F' and 'Model-P' values are respectively 277.72 & <0.0001 for weld penetration depth model; 64.43 & <0.0001 for radial penetration model; 34.55 & <0.0001 for weld resistance length model; and 28.42 & <0.0001 for weld shearing force model. These 'Model-F' and 'Model-P' values imply that the selected models are highly significant and there is only a less than 0.01% chance that these large 'Model-F' values could occur due to noise. The associated P values of less than 0.05 for the models (i.e. $\alpha = 0.05$, or 95% confidence level) indicate that the models are statistically significant as stated in [24]. The lack-of-fit values of the selected

models given in Table 6.15 indicate non-significance, as it is desirable. Also, lack-of-fit F-values imply that lack-of-fits are not significant relative to pure error.

Table 6.11: ANOVA table for weld penetration depth reduced quadratic Model

| Source | Sum of Squares | df | Mean Square | F Value | p-value Prob > F | |
|---|---|---|---|---|---|---|
| Model | 1.090 | 7 | 0.160 | 277.72 | < 0.0001 | significant |
| P (W) | 0.570 | 1 | 0.570 | 1008.28 | < 0.0001 | |
| S (m/min) | 0.280 | 1 | 0.280 | 496.82 | < 0.0001 | |
| A (deg) | 0.026 | 1 | 0.026 | 46.37 | < 0.0001 | |
| D (mm) | 0.0006 | 1 | 0.0006 | 1.07 | 0.3122 | |
| A×D | 0.045 | 1 | 0.045 | 79.76 | < 0.0001 | |
| $A^2$ | 0.065 | 1 | 0.065 | 115.94 | < 0.0001 | |
| $D^2$ | 0.130 | 1 | 0.130 | 228.09 | < 0.0001 | |
| Residual | 0.012 | 22 | 0.0006 | | | |
| Cor Total | 1.10 | 29 | | | | |
| $R^2$ = 0.989 | Adj. $R^2$ = 0.985 | | Pred. $R^2$ = 0.981 | | Adq. Precision = 62.46 | |

Table 6.12: ANOVA table for weld radial penetration reduced quadratic model

| Source | Sum of Squares | df | Mean Square | F Value | p-value Prob > F | |
|---|---|---|---|---|---|---|
| Model | 0.310 | 7 | 0.044 | 64.43 | < 0.0001 | significant |
| P (W) | 0.069 | 1 | 0.069 | 101.08 | < 0.0001 | |
| S (m/min) | 0.038 | 1 | 0.038 | 55.69 | < 0.0001 | |
| A (deg) | 0.160 | 1 | 0.16 | 233.60 | < 0.0001 | |
| D (mm) | 0.0007 | 1 | 0.0007 | 1.03 | 0.3213 | |
| A×D | 0.0071 | 1 | 0.0071 | 10.32 | 0.0040 | |
| $A^2$ | 0.0031 | 1 | 0.0031 | 4.50 | 0.0453 | |
| $D^2$ | 0.028 | 1 | 0.028 | 41.19 | < 0.0001 | |
| Residual | 0.015 | 22 | 0.0006 | | | |
| Cor Total | 0.32 | 29 | | | | |
| $R^2$ = 0.954 | Adj. $R^2$ = 0.939 | | Pred. $R^2$ = 0.927 | | Adq. Precision = 30.84 | |

Table 6.13: ANOVA table for weld resistance length reduced quadratic model

| Source | Sum of Squares | df | Mean Square | F Value | p-value Prob > F | |
|---|---|---|---|---|---|---|
| Model | 0.83 | 5 | 0.17 | 34.55 | < 0.0001 | significant |
| P (W) | 0.41 | 1 | 0.41 | 84.15 | < 0.0001 | |
| S (m/min) | 0.16 | 1 | 0.16 | 32.40 | < 0.0001 | |
| A (deg) | 0.20 | 1 | 0.20 | 41.60 | < 0.0001 | |
| P×A | 0.036 | 1 | 0.036 | 7.37 | 0.0123 | |
| $A^2$ | 0.11 | 1 | 0.11 | 22.73 | < 0.0001 | |
| Residual | 0.11 | 23 | 0.00482 | | | |
| Cor Total | 0.94 | 28 | | | | |
| $R^2$ = 0.882 | Adj. $R^2$ = 0.857 | | Pred. $R^2$ = 0.841 | | Adq. Precision = 20.13 | |

Table 6.14: ANOVA for weld shearing force reduced quadratic model

| Source | Sum of Squares | df | Mean Square | F Value | p-value Prob > F | |
|--------|---------------|-----|------------|---------|-----------------|---|
| Model | $8.57 \times 10^{-9}$ | 5 | $1.71 \times 10^{-9}$ | 28.42 | < 0.0001 | significant |
| P (W) | $3.41 \times 10^{-9}$ | 1 | $3.40 \times 10^{-9}$ | 56.50 | < 0.0001 | |
| S (m/min) | $2.84 \times 10^{-9}$ | 1 | $2.81 \times 10^{-9}$ | 47.13 | < 0.0001 | |
| A (deg) | $1.58 \times 10^{-9}$ | 1 | $1.57 \times 10^{-9}$ | 26.14 | < 0.0001 | |
| P×A | $2.01 \times 10^{-10}$ | 1 | $2.01 \times 10^{-10}$ | 3.34 | 0.0801 | |
| $A^2$ | $5.43 \times 10^{-10}$ | 1 | $5.42 \times 10^{-10}$ | 9.01 | 0.0062 | |
| Residual | $1.45 \times 10^{-9}$ | 24 | $6.03 \times 10^{-11}$ | | | |
| Cor Total | $1.00 \times 10^{-8}$ | 29 | | | | |

$R^2 = 0.856$  Adj. $R^2 = 0.825$  Pred. $R^2 = 0.791$  Adq. Precision = 18.34

Table 6.15: Lack-of-fit tests for the selected models

| | Sum of Squares | df | Mean Square | F Value | p-value Prob > F | |
|--|---------------|-----|------------|---------|-----------------|---|
| **For weld penetration depth reduced quadratic  model** | | | | | | |
| Lack of Fit | 0.0092 | 17 | 0.0005 | 0.86 | 0.6304 | Not significant |
| Pure Error | 0.0031 | 5 | 0.0006 | | | |
| **For weld radial penetration reduced quadratic  model** | | | | | | |
| Lack of Fit | 0.0057 | 17 | 0.0003 | 0.18 | 0.9967 | Not significant |
| Pure Error | 0.0093 | 5 | 0.0019 | | | |
| **For weld resistance length reduced quadratic  model** | | | | | | |
| Lack of Fit | 0.071 | 18 | 0.0039 | 0.50 | 0.874 | Not significant |
| Pure Error | 0.040 | 5 | 0.0079 | | | |
| **For weld shearing force reduced quadratic  model** | | | | | | |
| Lack of Fit | $1.04 \times 10^{-9}$ | 19 | $5.48 \times 10^{-11}$ | 0.68 | 0.757 | Not significant |
| Pure Error | $4.05 \times 10^{-10}$ | 5 | $8.11 \times 10^{-11}$ | | | |

The same ANOVA tables show the other adequacy measures e.g.  R-squared, adjusted R-squared, and predicted R-squared values. All these measures are in logical agreement and indicate significant relationships. Moreover, adequate precision compares range of predicted value at the design points to average prediction error. The adequate precision ratios in all cases are dramatically greater than 4 indicating adequate models discrimination.

From Tables 6.11 and 6.12 showing the ANOVA results for reduced quadratic models, it is evident that the main effects of laser power (P), welding speed (S), and incident angle (A), the quadratic effects of incident angle ($A^2$), and defocus distance ($D^2$) along with the interaction effects of incident angle and defocus distance (A×D) are the significant model terms associated with weld penetration depth and radial penetration. Nevertheless, the effect of defocus distance (D) is

added to the aforestated models to support hierarchy. For the weld resistance length and shearing force reduced quadratic models, the corresponding ANOVA tables show that the main effects of laser power (P), welding speed (S), and incident angle (A), the quadratic effect of incident angles ($A^2$) along with two-factor interaction of laser power and incident angle (P×A) are the significant model terms. The other model terms are not significant and thus eliminated by backward elimination process to improve the model adequacy.

The developed statistical models are, therefore, fairly accurate and can be used for prediction within the same design space. The final models as determined by Design Expert software are given below:

(a) in terms of coded factors:

Weld penetration depth

$$D_p = 1.25 + 0.31P - 0.22S - 0.066A + 1 \times 10^{-2}D - 0.21A \times D$$
$$-0.19A^2 - 0.27D^2 \tag{3}$$

Weld radial penetration

$$P_r = 0.28 + 0.11P - 0.08S + 0.16A - 0.011D - 0.084A \times D$$
$$+0.042A^2 - 0.13D^2 \tag{4}$$

Weld resistance Length

$$S_L = 1.14 + 0.26P - 0.16S - 0.21A - 0.19P \times A - 0.33A^2 \tag{5}$$

Weld shearing force

$$(F_s)^{-0.77} = 3.77 \times 10^{-4} - 2.383 \times 10^{-5}P + 2.176 \times 10^{-5}S$$
$$+1.621 \times 10^{-5}A + 1.419 \times 10^{-5}P \times A + 1.737 \times 10^{-5}A^2 \tag{6}$$

(b) in terms of actual factors:

Weld penetration depth

$$D_P = 0.0313 + 1.535 \times 10^{-3}P - 0.2155S + 0.0699A + 0.2887D$$
$$-0.0141A \times D - 1.9125 \times 10^{-3}A^2 - 0.1192D^2 \tag{7}$$

Weld radial penetration

$$P_r = -0.0724 + 5.3667 \times 10^{-4}P - 0.0797S - 3.333 \times 10^{-4}A + 0.1048D$$
$$-5.6 \times 10^{-3}A \times D + 4.1625 \times 10^{-4}A^2 - 0.0559D^2 \tag{8}$$

Weld resistance length

$$S_L = -1.8191 + 3.185 \times 10^{-3}P - 0.1613S + 0.1864A$$
$$-9.425 \times 10^{-5}P \times A - 3.31 \times 10^{-3}A^2 \tag{9}$$

Weld shearing force

$$(F_s)^{-0.77} = 5.577 \times 10^{-4} - 2.61 \times 10^{-7}P + 2.176 \times 10^{-5}S$$
$$-1.1 \times 10^{-5}A + 7.093 \times 10^{-9}P \times A + 1.737 \times 10^{-7}A^2 \tag{10}$$

Figs 6.5-6.7 are the 3D surface plots illustrating the effects of process parameters and their interactions on weld bead geometric parameters.
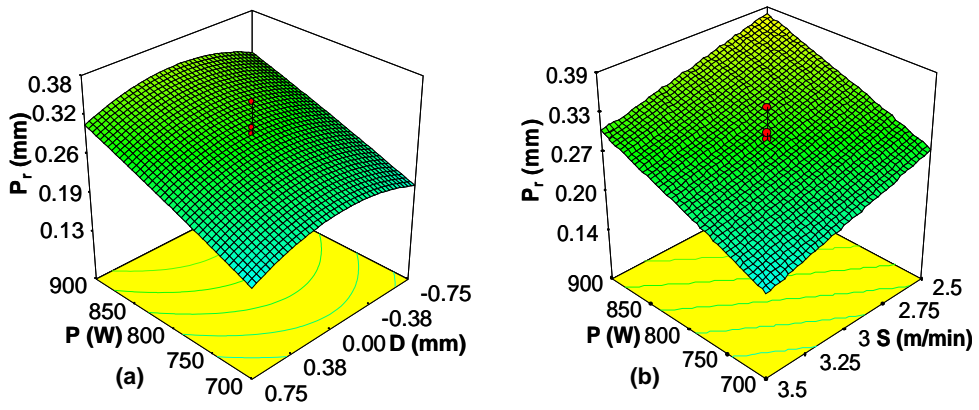
Fig. 6.5: 3D graphs show effects of (a) P and D, and  (b) P and S on weld radial penetration depth.
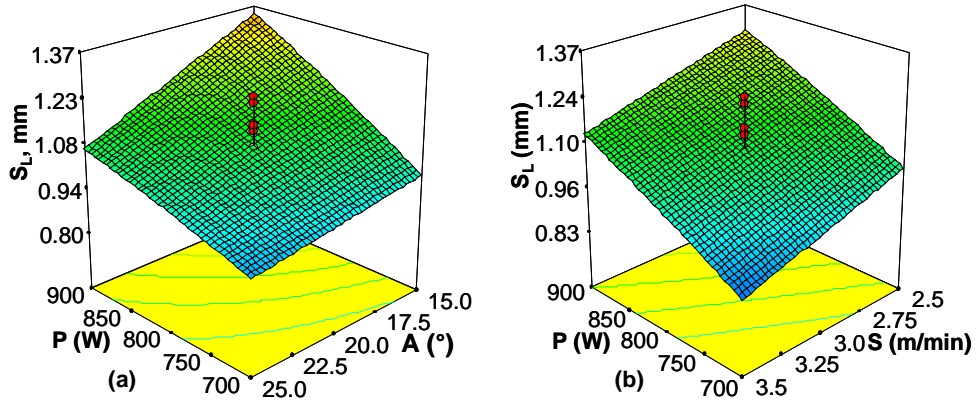


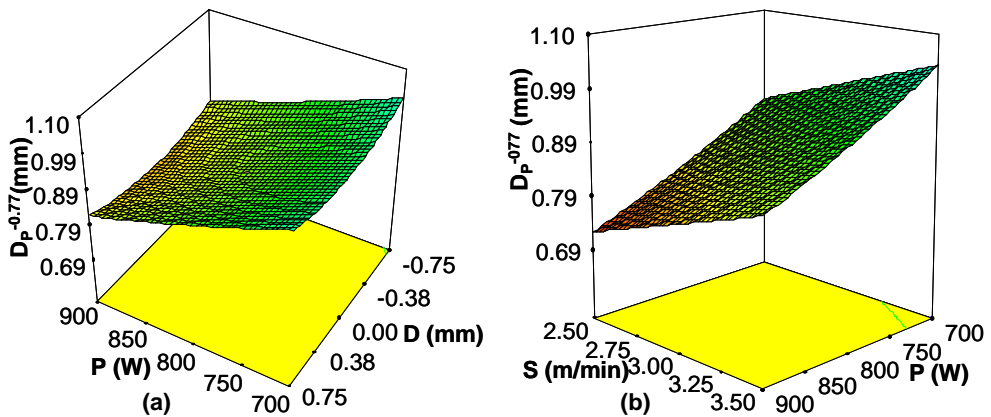Fig. 6.6: 3D graphs show effects of (a) P and A, and (b) P and S on weld resistance length.



Fig. 6.6: 3D graphs show effects of (a) P and D, and (b) P and S weld penetration depth.

## 6.3.1.3 Validation of the models developed

Normality of residual data, pattern of error variance, presence of outliers, and amount of residuals in prediction are checked to ensure statistical validation of the developed models. The normality of data is verified by plotting the normal probability plot (NPP) of residuals. The residual is the difference between observed and predicted value (or fitted value) obtained from the regression model. The data set is normally distributed if the points on the plot fall fairly close to the straight line. The normal probability plots of residual values for weld penetration depth, radial penetration, resistance length and shearing force are illustrated in Figs 6.8 (a)-(d) respectively. The experimental points are reasonably aligned with predicted or fitted points suggesting the normality of data.
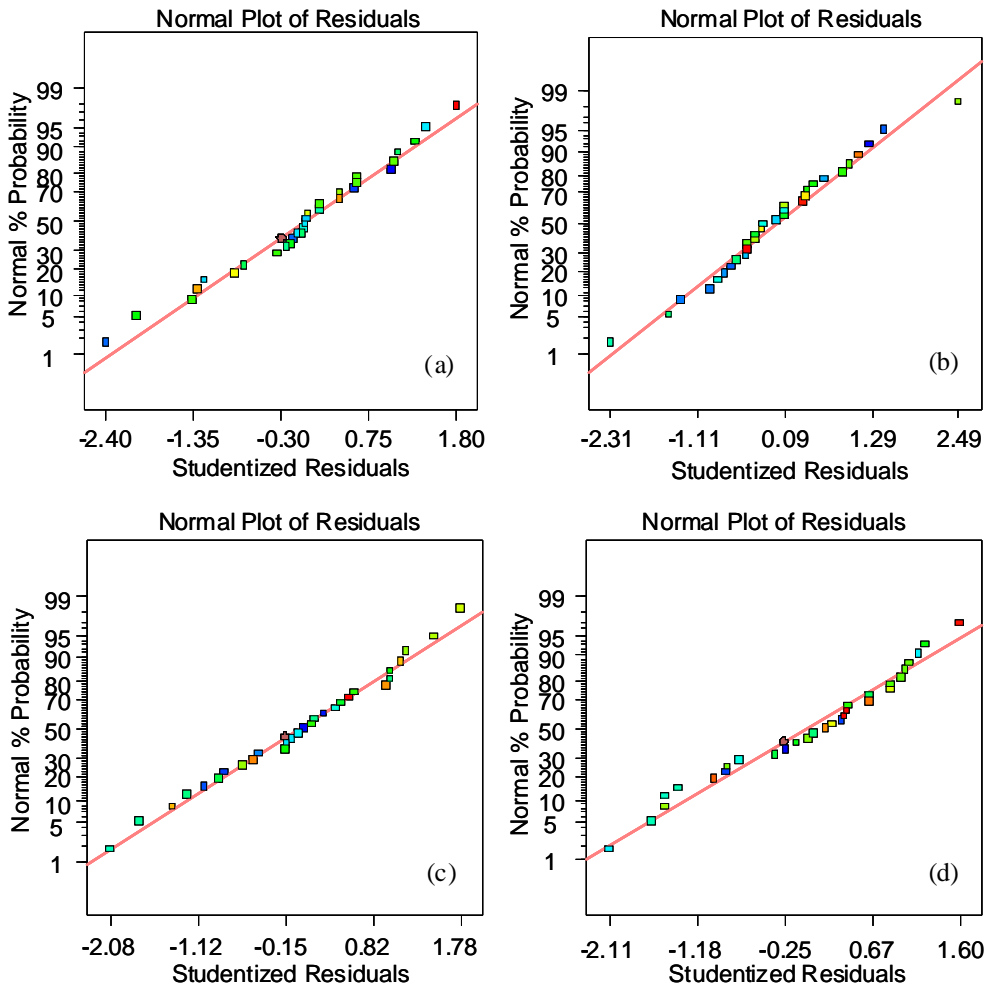


Fig. 6.8:  Normal probability plot for weld (a) penetration depth, (b) radial penetration, (c) resistance length, and (d) shearing force

Figs 6.9 (a)-(d) demonstrate studentized residuals versus fitted values (predicted response) for weld penetration, radial penetration, resistance length, and shearing force respectively. The residuals are found to be scattered randomly about zero. This indicates that errors have a constant variance for all response variables. Plot of standardized residuals vs. predicted values also shows the possible existence of outliers. If a point lies far from the majority of points, it may be an outlier. It is important to identify the outliers as these can significantly influence the model and provide potentially misleading or incorrect results. As shown in the figures, all the points are within $\pm$ 2.0$\sigma$ limits for each of the response models and confirm no existence of such outliers.
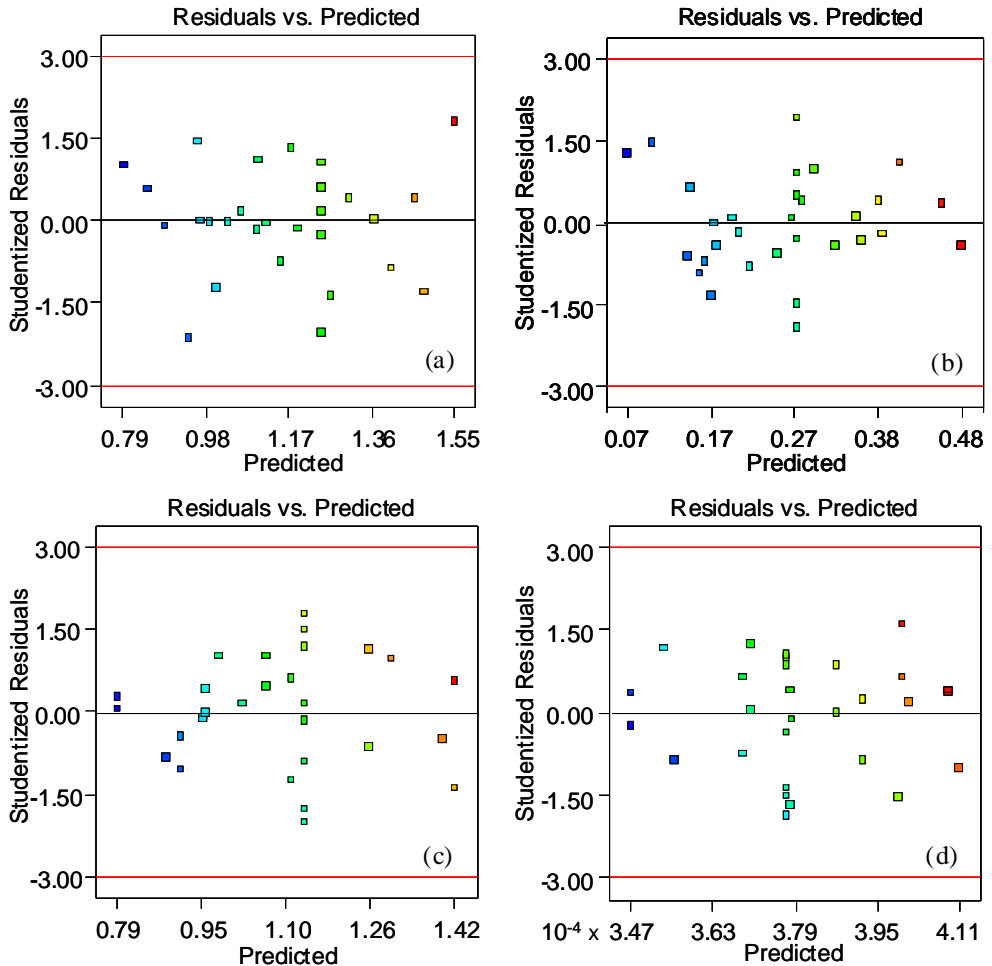


Fig. 6.9:  Studentized residual vs predicted plot for weld (a) penetration depth, (b) radial penetration, (c) resistance length, and (d) shearing force.

Figs 6.10(a)-(d) are showing the relationships between the actual and predicted values of weld penetration depth, radial penetration, resistance length and shearing forces respectively. These figures illustrate that the developed models are

adequate and predicted results are in good agreement with the measured data as the residuals tend to be close to the diagonal line.
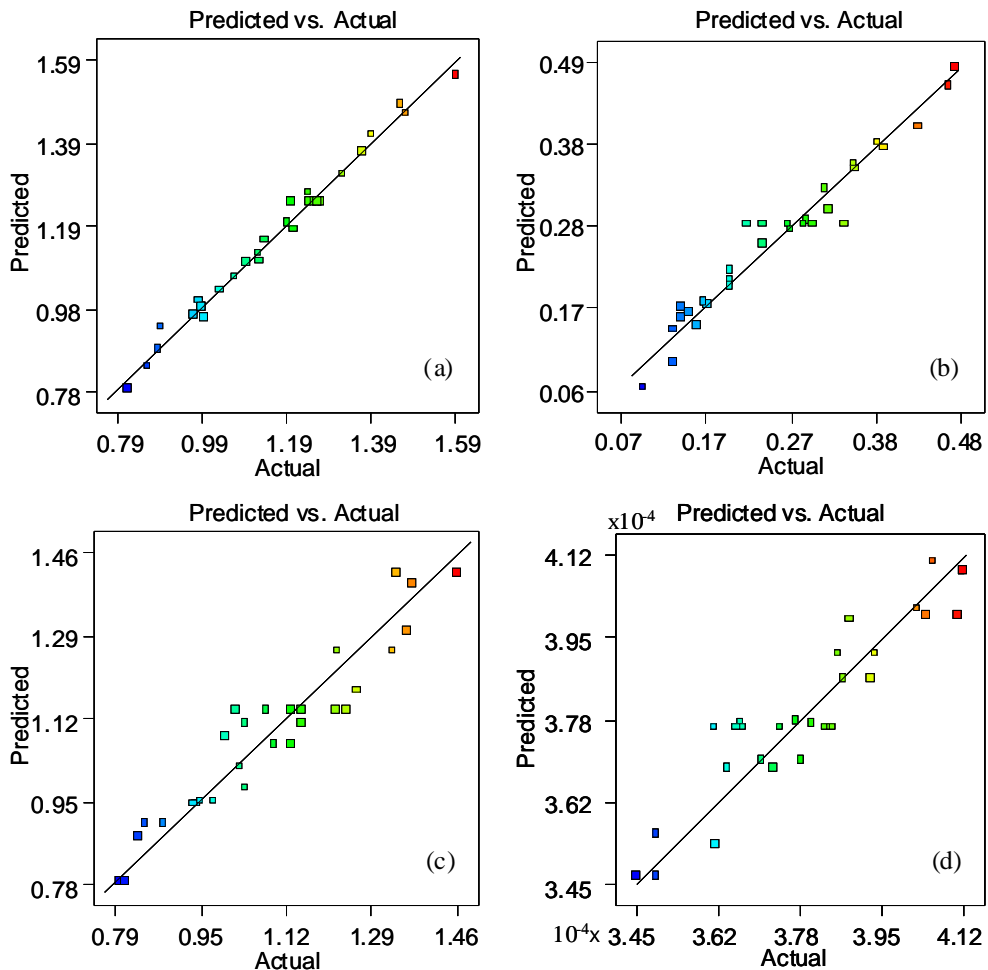


Fig. 6.10: Scatter diagrams of weld (a) penetration depth, (b) radial penetration, (c) resistance length, and (d) shearing force.

Besides, in order to validate the developed response surface equations derived from multiple regression analyses, three confirmation experiments are conducted with welding conditions chosen randomly within the ranges for which the equations are developed. The actual results are calculated as the average of three measured results for each response. The actual results, predicted values and calculated percentage error of confirmation experiments are furnished in Table 6.16. It is observed from the validation experiments that there is a small percentage error between the estimated and the experimental values. These results indicate that the developed models can yield nearly accurate results.

Table 6.16: Confirmation experiments

| No. of Expt | Process Parameters | | | | | Response Factors | | | |
|---|---|---|---|---|---|---|---|---|---|
| | P (W) | S (m/min) | A (Deg) | D (mm) | | $P_r$ (mm) | $D_P$ (mm) | $S_L$ (mm) | $F_S$ (N) |
| Expt. I | 950 | 3.0 | 25 | 0.75 | Actual | 0.390 | 1.260 | 1.110 | 28890 |
| | | | | | Predicted | 0.392 | 1.281 | 1.075 | 27946 |
| | | | | | **Error(%)** | **0.517** | **1.53** | **-3.12** | **-3.39** |
| Expt. II | 850 | 3 | 15 | -0.75 | Actual | 0.185 | 1.155 | 1.285 | 29390 |
| | | | | | Predicted | 0.186 | 1.183 | 1.253 | 29082 |
| | | | | | **Error(%)** | **0.062** | **2.41** | **-2.47** | **-1.05** |
| Expt. III | 750 | 2.0 | 20 | 0 | Actual | 0.328 | 1.355 | 1.280 | 30770 |
| | | | | | Predicted | 0.331 | 1.385 | 1.236 | 29534 |
| | | | | | **Error(%)** | **0.912** | **2.24** | **-3.51** | **-4.19** |

## 6.3.2 Process parameter optimization

### 6.3.2.1 Numerical optimization

From weld design specification as described in ISO15614-11, weld radial penetration, resistance length and shearing force are the response factors that characterize a fillet welded joint. Laser fillet welding input parameters should be optimized to obtain the optimal values of these response factors. Two sets of criteria have been implemented in the numerical optimization. The first set of criteria is to reach minimum radial penetration, and maximum resistance length and shearing force of the weld with no limitation on the process parameters. For this particular type of joint, lowering the laser power and incident angle, and increasing the welding speed are the most common techniques used in automotive industries to produce relatively low-cost and excellent weld joints. Taking these cost and quality aspects into account, second set of criteria are fixed to maximize welding speed and minimize laser power and incident angle along with the goals defined for the response factors in the first set. Also, a target value of zero is set to defocus distance as the focused beam (D=0 mm) provides the smallest spot diameter on the weld plane and hence, the highest energy input onto the materials being welded. Table 6.17 summarizes these two criteria, limiting values and importance for each input and response factor.

Table 6.17: Optimization criteria used in this study

| Name | Limit | | First Criterion | | Second Criterion | |
|---|---|---|---|---|---|---|
| | Lower | Upper | Goal | Importance | Goal | Importance |
| P (W) | 600 | 1000 | is in range | 3 | minimize | 5 |
| S (m/min) | 2 | 4 | is in range | 3 | maximize | 5 |
| A (deg) | 10 | 30 | is in range | 3 | minimize | 5 |
| D (mm) | -1.5 | 1.5 | is in range | 3 | is target = 0 | 5 |
| $S_L$ (mm) | 0.790 | 1.457 | maximize | 5 | maximize | 5 |
| $P_r$ (mm) | 0.094 | 0.475 | minimize | 5 | minimize | 5 |
| $F_s$ (N) | 24933 | 31317 | maximize | 5 | maximize | 5 |

Tables 6.18 and 6.19 show the optimal solutions based on two optimization criteria as determined by design-expert software. The results demonstrate that, whatever

117

the criteria, the laser has to be focused on the weld plane (i.e. D = 0 mm) to obtain a weld with longer resistance length, smaller radial penetration and higher shearing force.

Table 6.18: Optimal solutions as obtained based on first criterion

| $Sol^n$ No. | P (W) | S (m/min) | A (deg) | D (mm) | $S_L$ (mm) | $P_r$ (mm) | $F_s$ (N) |
|---|---|---|---|---|---|---|---|
| 1 | 1000 | 3.24 | 10.4 | 0.00 | 1.444 | 0.248 | 31317 |
| 2 | 1000 | 3.24 | 10.3 | 0.00 | 1.440 | 0.247 | 31317 |
| 3 | 1000 | 3.24 | 10.6 | 0.00 | 1.440 | 0.249 | 31317 |
| 4 | 1000 | 3.24 | 10.2 | 0.00 | 1.438 | 0.246 | 31317 |
| 5 | 1000 | 3.25 | 10.8 | 0.00 | 1.451 | 0.251 | 31317 |
| 6 | 1000 | 3.23 | 10.0 | 0.00 | 1.434 | 0.245 | 31317 |
| 7 | 999 | 3.23 | 10.4 | 0.00 | 1.441 | 0.248 | 31317 |
| 8 | 1000 | 3.21 | 10.3 | 0.00 | 1.444 | 0.249 | 31386 |
| 9 | 1000 | 3.20 | 10.0 | 0.00 | 1.447 | 0.245 | 31410 |

Again, from Table 6.18 demonstrating the optimal welding conditions based on the first set of criteria, it is evident that the obtainable longest resistance length, the smallest radial penetration and the highest shearing force are respectively 1.447 mm, 0.245 mm and 31410 N for laser power, welding speed and incident angle of 1000 W, 3.2 m/min and 10° respectively. However, with an acceptable weld resistance length, radial penetration and shearing force, the laser power can be minimized to 865 W, and the welding speed can be maximized to 4 m/min as shown in Table 6.19. However, incident angle increases to 12°. Under this condition, the weld resistance length, radial penetration, and shearing force are found to be 1.176 mm, 0.18 mm and 28479 N respectively, which are much greater than the respective prerequisite values for this particular weld.

Table 6.19: Optimal solutions as obtained based on second criterion

| $Sol^n$ No. | P (W) | S (m/min) | A (deg) | D (mm) | $S_L$ (mm) | $P_r$ (mm) | $F_s$ (N) |
|---|---|---|---|---|---|---|---|
| 1 | 875 | 3.44 | 11.7 | 0.00 | 1.177 | 0.177 | 28468 |
| 2 | 874 | 3.43 | 11.7 | 0.00 | 1.178 | 0.177 | 28479 |
| 3 | 876 | 3.45 | 11.7 | 0.00 | 1.179 | 0.177 | 28473 |
| 4 | 877 | 3.45 | 11.7 | 0.00 | 1.176 | 0.176 | 28455 |
| 5 | 875 | 3.43 | 11.8 | 0.00 | 1.180 | 0.178 | 28484 |
| 6 | 877 | 3.44 | 11.6 | 0.00 | 1.179 | 0.176 | 28493 |
| 7 | 873 | 3.44 | 11.8 | 0.00 | 1.176 | 0.176 | 28433 |
| 8 | 865 | 4.00 | 12.0 | 0.00 | 1.176 | 0.180 | 28479 |

The aforestated tables also show that, for the first set of optimization criteria, the optimal range of welding speed is 3.2-3.25 m/min with a laser power of 1000W. However, the optimal ranges of laser power and welding speed can be reduced to 860-875W and increased to 3.4-4.0 m/min respectively if the second set of optimization criteria are applied. As a consequence, any combination of process

parameters for the second optimal settings would cause less energy density input to the weld. The reduced energy input that results in less distortion and formation of cracks, blow holes, and spatter would lead to better weld quality as can be seen from visual inspection data given in Table 6.20.

Table 6.20: Visual inspection of weld quality

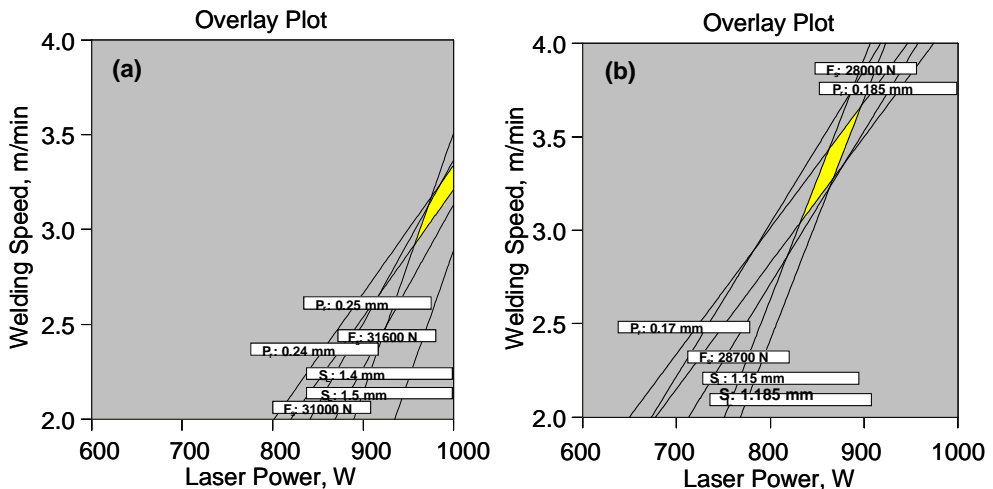| Process Parameters | | | | Visual check | | |
|---|---|---|---|---|---|---|
| P (W) | S (m/min) | A (deg) | D (mm) | Spatter | Cracks | Blow holes |
| 700 | 2.5 | 15 | -0.75 | 1 | 0 | 0 |
| 900 | 2.5 | 15 | -0.75 | 1 | 1 | 0 |
| 700 | 3.5 | 15 | 0.75 | 0 | 0 | 0 |
| 900 | 3.5 | 15 | 0.75 | 1 | 1 | 0 |
| 800 | 3.0 | 10 | 0 | 1 | 1 | 0 |
| 800 | 3.0 | 30 | 0 | 1 | 0 | 0 |
| 800 | 2.0 | 20 | 0 | 1 | 1 | 0 |
| 800 | 4.0 | 20 | 0 | 0 | 0 | 0 |
| 600 | 3.0 | 20 | 0 | 0 | 0 | 0 |
| 1000 | 3.0 | 20 | 0 | 2 | 0 | 1 |

0: No defect,   1: Marginally acceptable;     2: Not acceptable



Fig. 6.11: Overlay plots show the region of optimal welding condition based on (a) the first criterion at A = 10° & D = 0 and (b) the second criterion at A = 12° & D = 0.

### 6.3.2.2 Graphical optimization

The graphical optimization allows visual selection of the optimum welding conditions according to certain criterion. The result of the graphical optimization are the overlay plots and these type of plots are extremely practical for quick technical use in the workshop to choose the values of the welding parameters that would achieve certain response value for this type of material. In this case, for each response, the limits lower and/or upper have been chosen according to the numerical optimization results. The same two criteria, which are proposed in the

numerical optimization, are introduced in the graphical optimization. The yellow colored areas on the overlay plots shown in Figs 6.11 (a) and (b) are the regions that meet the proposed criteria.

## 6.4 CONCLUSIONS

For the laser system, weld joint type and the limits of laser parameters considered in this study, the following points can be concluded:

- RSM is an accurate technique to optimize the laser welding process in order to obtain the most desirable weld quality in terms of weld bead geometry and mechanical strength, and to determine the corresponding optimal settings of welding parameters,
- Welding speed has a negative effect on all the responses investigated whereas; the laser power has a positive effect. Laser beam incident angle plays an important role in weld bead profile dimensions determining the weld shearing force.
- Whatever the optimization criteria, laser has to be focused on weld plane at an angle within the range of 10°-12° to obtain a weld with longer resistance length, smaller radial penetration and greater shearing force,
- Laser power and welding speed of a focused beam in the range 860–875W and 3.4–4.0 m/min respectively with an incident angle of around 12° are the optimal settings of fillet welding input parameters to obtain an excellent welded component made of ferritic AISI430 and austenitic AISI304L stainless steels,
- Weld joint of desired quality and strength could be using the optimal welding combinations obtained from the numerical optimization,
- The graphical optimization results allows quicker search for the optimal settings for laser fillet welding.

## REFERENCES

1. Steem WM, Mazumder J, 2010, laser material processing, Springer-Verlag London limited, London.
2. Weichiat C, Paul A, Pal M., 2009, $CO_2$ laser welding of galvanized steel sheets using vent holes, Materials and Design, 30:245–51.
3. Mackwood AP, Crafer RC, 2005, Thermal modeling of laser welding and related processes: a literature review, Opt Laser Technol, 37:99–115
4. Kaiser E, Schafer P, 2005, Pulse shaping optimizes the quality of seam and spot welds. In: Lasers in manufacturing, proceeding of the third international WLT—conference on lasers in manufacturing. pp. 695–670
5. Sun Z, Kuo M, 1998, Bridging the joint gap with wire feed laser welding, J Mater Process Technol, 87:213–222
6. Liu X-B, Yu G,Guo J, Gu Y-J, Pang M, Zheng C-Y, Wang H-H, 2008, Research on laser welding of cast Ni-based superalloy K418 turbo disk and alloy steel 42CrMo shaft, J Alloy Comp, 453(1–2):371–378.
7. Huang Q, Hagstroem J, Skoog H, Kullberg G, 1991, Effect of $CO_2$ laser parameter variations on sheet metal welding, International Journal for the Joining of Materials, 3(3):79–88

8. Juang SC, Tarng YS, 2002, Process parameter selection for optimizing the weld pool geometry in the tungsten inert gas welding of stainless steel, J Mater Process Technol, 122:33–37

9. Marya M, Edwards G, Marya S, Olson DL, 2001, Fundamentals in the fusion welding of magnesium and its alloys. In: Proceedings of the seventh JWS international symposium. pp. 597–602.

10. Haferkamp H, Niemeyer M, Dilthey U, Trager G, 2000, Laser and electron beam welding of magnesium materials, Weld Cutt 52(8):178–80.

11. Haferkamp H, Bach Fr-W, Burmester I, Kreutzburg K, Niemeyer M, 1996, Nd:YAG laser beam welding of magnesium constructions. In: Proceedings of the third international magnesium conference. pp. 89–98.

12. Benyounis KY, Olabi AG, Hashmi MSJ, 2005, Effect of laser welding parameters on the heat input and weld-bead profile, J Mater Process Technol, 164-165:978–985.

13. Manonmani K, Murugan N, Buvanasekaran G, 2007, Effects of process parameters on the bead geometry of laser beam butt welded stainless steel sheets, J Adv Manuf Technol, 32(11-12):1125-1133.

14. Elangovan K, Balasubramanian V, 2008, Developing an empirical relationship to predict tensile strength of friction stir welded AA2219 aluminium alloy joints, J Mater Eng Perform, 17:820–830.

15. Benyounis KY, Olabi AG, Hashmi MSJ, 2008, Multi-response optimization of CO2 laser-welding process of austenitic stainless steel, Opt Laser Technol 40:76-87.

16. Moradi M, Ghoreishi M, 2010, Influences of laser welding parameters on the geometric profile of NI-base superalloy Rene 80 weld-bead, Int J Adv Manuf Technol, doi: 10.1007/s00170-010-3036-1.

17. Padmanaban G, Balasubramanian V, 2010, Optimization of laser beam welding process parameters to attain maximum tensile strength in AZ31B magnesium alloy, Opt Laser Technol, 42:1253–1260

18. Rajakumar S, Muralidharan C, Balasubramanian V, 2010, Optimization of the friction-stir-welding process and the tool parameters to attain a maximum tensile strength of AA7075-T6 aluminium alloy, J Eng Manuf, 224:1175–1191.

19. Ruggiero A, Tricarico L, Olabi AG, Benyounis KY, 2011, Weld-bead profile and costs optimization of the $CO_2$ dissimilar laser welding process of low carbon steel and austenitic steel AISI316, Opt Laser Technol, 43:82–90.

20. Myers RH, Montgomery DC, 2002, Response Surface Methodology: Process and Product Optimization Using Designed Experiments, Wiley, New York.

21. Robinson TJ, Wulff SS, 2006, Response surface approaches to robust parameter design. In: Khuri AI (ed) Response surface methodology and related topics, World Scientific, Singapore, pp. 123-157.

22. Gunaraj V, Murugan N, 1999, Application of response surface methodologies for predicting weld base quality in submerged arc welding of pipes, J Mater Process Technol, 88:266–275.

23. Design-ExpertSoftware,V7, 2005, User's guide: Technical Manual, Minneapolis, MN: Stat-Ease Inc.

24. Zulkali MMD, Ahmad AL, Norulakmal NH, 2006, Oryza sativa L. husk as heavy metal adsorbent: optimization with lead as model solution, Bioresource Technology, 97:21–25.

25. Cui C, Hu J, Gao K, Pang S, Yang Y, Wang H, Guo Z, 2008, Effects of process parameters on weld metal keyhole characteristics with $CO_2$ laser butt welding, Lasers in Engineering, 18:319–327.

# CHAPTER 7

## A SIMPLIFIED ENERGY-BASED MODEL FOR LASER WELDING OF FERRITIC STAINLESS STEELS

*This chapter describes a simplified energy-based theoretical model for predicting the weld shape produced by a continuous wave (CW) Nd:YAG laser in a constrained overlap configuration on a ferritic stainless steel.*

*The model developed is verified by means of experiments. Tests demonstrate that, as assumed in the modeling phase, penetration depth is linearly dependent on the energy density input and determines the weld resistance length at the interface within the hypothesis of conduction-dominated welding.*

*Developed model predicts the weld penetration depth accurately (with 5% prediction error) for conduction-limited laser welding. Though error in prediction increases, developed model is also able to reasonably predict the penetration depth (with a prediction error of 10%) beyond conduction limit. However, it also indicates that different heat transfer phenomena and thermal losses restrict the use of the model.*

*This energy based model needs only the accurate thermophysical property data for reliable predictions. This model will be able to predict reasonably the penetration depth of weld made of ferritic stainless steels in a wider range provided that (i) reliable values for thermo-physical properties of the intended stainless steels are given (ii) welding is conduction limited (iii) welds are in overlap joint configurations.*

## 7.1 INTRODUCTION

The increasing use of laser beam welding in automotive industries to weld small and heat sensitive complex parts of fuel injectors, poses new theoretical tasks with respect to process development, defect explanation, and process control. Since the early days of laser welding, an impressive amount of research has been carried out in order to explain shape and size of weld pool [1]. In recent years, researchers developed models for high laser power, which led to keyhole formation and transportation of heat well below the surface as soon as the laser beam impinged on the material. In this context, 'Gaussian rod' type heat source was proposed [2]. The double ellipsoid model incorporated the volumetric heat input from a moving source [3]. Moreover, Su et al. [4] established a rotary Gaussian volumetric heat source model. Apart from those models, several FEM based models for predicting the weld pool geometry in laser welding were developed [5-8].

### 7.1.1 Research objective

The literature review demonstrates that numerous sophisticated models have been developed to study wide range of conditions. The shape of the heat source can be retained up to now the main concern: recent studies are then devoted to improve the complexity of volumetric heat sources to better describe the real weld pool geometry. However, the complexity of these models limits their application for a direct control on process parameters while production is going on. Currently, after setting the process parameters and as a routine activity, the technicians have to select some samples randomly from the production line and undergo some cost-consuming monitoring activities to ensure the required weld penetration depth. This is because penetration depth is the characterizing parameter that determines the desired weld resistance length at the shells interface and hence, the shearing strength of the weld joint in overlap configuration as shown in figure 7.2. An easy-to-use model is, therefore, needed to estimate the weld penetration depth directly from the process parameters. At this purpose, the main objective of the present research is to overcome the abovementioned drawbacks by developing a simplified theoretical model based on energy density. This parameter is commonly used to express laser variables in energetic term [9] and will be correlated with weld characteristics obtained by a CW Nd:YAG laser in a constrained overlap configuration on a ferritic stainless steel.

## 7.2 PENETRATION DEPTH MODELING

The following assumptions are made to analytically describe the welding process in overlap configuration:

- The maximum temperature $T_{max}$, reached at the material surface, is lower than the vaporization point. Keyhole formation is not considered in the model.
- Heat transfer is governed by conduction. Convection and radiation are neglected due to the small exchange area.
- Heat is mainly conducted along beam axis. This is justified by the need of providing a weld profile which ensures a desired resistance length at the interface and at the same time reducing energy diffusion in the surroundings.

- The weld profile is deemed to be dependent on the Gaussian energy distribution of the beam.

The mass of welded material m is considered to be proportional to the amount of energy available to melt the steel, as also reported in [10]. Available energy can be evaluated as the difference between the absorbed energy $Q_{ab}$ and a threshold value $Q_{th}$ that has to be overcome to initiate the melting process. $Q_{th}$ represents energy losses which are mainly related to heat conduction in directions differing from the beam axis. m is then given by:

$$m = K(Q_{ab} - Q_{th})$$ (1)

The constant K (kg/J), which is the reciprocal of the specific energy needed to change the physical state of 1kg of steel, can be obviously expressed as follows:

$$K = \frac{1}{C_{ps}(T_m - T_{amb}) + H_m + C_{pl}(T_{max} - T_m)}$$ (2)

being $C_{ps}$ the specific heat in solid state, $H_m$ the latent heat at the melting point, $C_{pl}$ the specific heat in liquid state, $T_m$ and $T_{amb}$ the melting and the environment temperatures.

The absorbed energy can be evaluated as the product of the absorption coefficient A, the incident power $P_{in}$ and the irradiation time $\Delta t$:

$$Q_{ab} = A_c P_{in} \Delta t \qquad \text{where} \qquad \Delta t = L / v$$ (3)

The coefficient $A_c$ is set to 0.31, according to [11] where the amount of absorption at normal incidence, on an opaque surface of stainless steel, was derived at wavelength $\lambda$ = 1.06 µm.

The irradiation time is then given by the ratio between the extension of the irradiated area along the welding direction L and the welding speed v. Considering one generic position of the beam; it acts to melt new material only on a semicircular area whose diameter represents the weld width W, as shown in Fig 7.1(a). As a consequence, L is half the weld width W and the irradiated area is assumed rectangular to simulate the continuous interaction of the CW laser beam with the metal surface.
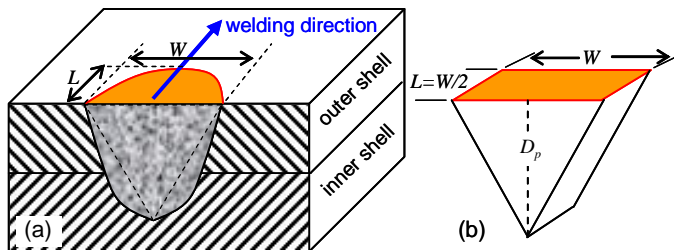


Fig. 7.1 (a) draft of the weld cross section (b) assumed melt volume and related geometrical parameters.

Furthermore, being the beam profile Gaussian, and the heat transfer governed by conduction, the weld cross section geometry is similar to the beam shape. It can be

125

approximated as a triangle for the prediction of the penetration depth. The volume of melted material is then the prism with triangular base illustrated in Fig. 7.1(b). Consequently the density of the material ρ can be expressed as follows:

$$\rho = \frac{m}{D_p (W/2) L} \tag{4}$$

Substituting equations (3) and (4) into equation (1) the penetration depth results to be dependent linearly on $P_{in}$ and inversely on $v$ and $W$.

$$D_p = \frac{2KA_c}{\rho} \left[ \frac{P_{in}}{vW} \right] - \frac{4KQ_{th}}{\rho W^2} \tag{5}$$

The threshold energy $Q_{th}$ can be readily determined putting $D_p = 0$ in eq. (5) and considering that, due to the very reduced initial amount of heat needed to start the melting process, the width of the fused area $W$ is not larger than the spot diameter $\Phi_{spot}$. Approximating $W$ to $\phi_{spot}$, $Q_{th}$ results as follows:

$$Q_{th} = \frac{A_c \cdot ED_{th}}{2} \varphi_{spot}^2 \qquad \text{where} \qquad ED = P_{in} / (v \varphi_{spot}) \tag{6}$$

where $ED_{th}$ (J/mm$^2$) is here intended as the energy density threshold ratio. This value represents the limit condition above which melting occurs. It depends on the laser set-up adopted along with the type of steel to be welded and, as a direct consequence, must be derived experimentally before starting the welding test plan. The procedure for the determination of $ED_{th}$ in the present research will be described in brief during the discussion of the experimental results.

Equation (5) shows that, in a thermal process dominated by conduction, $D_p$ is a function of laser parameters but also of $W$ which is itself related to laser parameters. In the case of laser welding, eq. (5) can be further simplified considering that this technology allows a fast and precise heat transfer to the workpiece. As a result, conduction in directions normal to the beam axis is limited and the width of the weld joint is confined on the restricted range represented by the spot diameter. Therefore in equation (5) $W$ can be substituted with $\Phi_{spot}$ obtaining:

$$D_p = \frac{2K}{\rho} \left[ A_c \cdot ED - \frac{2Q_{th}}{\varphi_{spot}^2} \right] \tag{7}$$

Penetration depth is then linearly linked with energy density which is determined by the three main process parameters: $P_{in}$, $v$ and $\phi_{spot}$. The value of $D_p$ obtainable by using a defined energy density can be easily calculated once the material properties (e.g. ρ, K, A) are defined and the threshold energy $Q_{th}$ is experimentally derived for a given laser set-up. The variation of the maximum temperature above the melting point, generated by a defined range of energy density, is a further process characteristic since it influences the value of K. $T_{max}$ can be directly monitored during the welding process. Alternatively it can be empirically estimated by a metallographic characterization of the weld bead along with the map of microstructural changes of the base metals in comparison with their CCT diagrams.

## 3. EXPERIMENTAL

In order to validate the model developed and justify the adopted hypotheses, a typical ferritic stainless steel, AISI430, which is commonly used in automotive industries to fabricate the fuel injector, are welded in overlap joint configuration. The temperature dependent thermo-physical properties of the selected metal are derived using the empirical relationships developed in [12]. Weld characteristics are shown in Fig. 7.2(a). The inside diameter of outer shell and the outside diameter of inner shell are machined to Ø7.500±0.025 mm and Ø7.458±0.015 mm respectively. Tubular parts thus fabricated are assembled together by a clearance fit and crimped applying a uniform force of 45 kN around the tip of outer shell to ensure close contact (zero clearance) in the interface surfaces during welding. This step is done as a replication of the actual fabrication process.
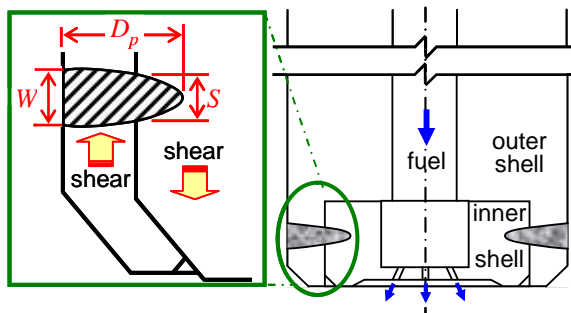


Fig. 7.2: (a) weld characteristics W weld width, $D_P$ penetration depth, S resistance length and (b) tip of the fuel injector.

Specimens are welded circularly in an overlap joint configuration using a 1.1 kW continuous wave Nd:YAG laser (Rofin DY011). Each welding test is replicated three times and the average value of each of the measured weld characteristics is determined and recorded for the analysis. The optical system consisted of 400 μm fibers with the lenses of 200 mm focal and collimated lengths delivered laser at spot diameters of 400 μm. During experimentation, energy density inputs on the focused area are derived from process parameters ($P_{in}$, v and $\Phi_{spot}$) and varied in the range of 16.0-48.9 J/mm$^2$. The laser is focused normally on the specimen surface and argon is supplied as a shielding gas at a constant flow rate of 29 l/min. A standard washing procedure practised in the automotive industries is followed to clean, cool and dry the specimens. To validate the model developed, an additional set of tests is conducted with replications within the same energy density input range. The average weld penetration depth for each set of the replicated tests is calculated and used for model validation.

## 7.4 RESULTS AND DISCUSSION

Firstly, threshold energy density input determining the initiation of local melting has been investigated experimentally. In assessing this threshold limit, a set of experiment is conducted varying the energy density inputs in the range of 0.5-3.0 J/mm$^2$. Energy density is increased step-wise by 0.2 J/mm$^2$ and the samples thus exposed to the laser radiation are inspected using an optical microscope. From the

experimental results, the local meting is found to kick off when the energy density input is set to 2.8 J/mm$^2$.
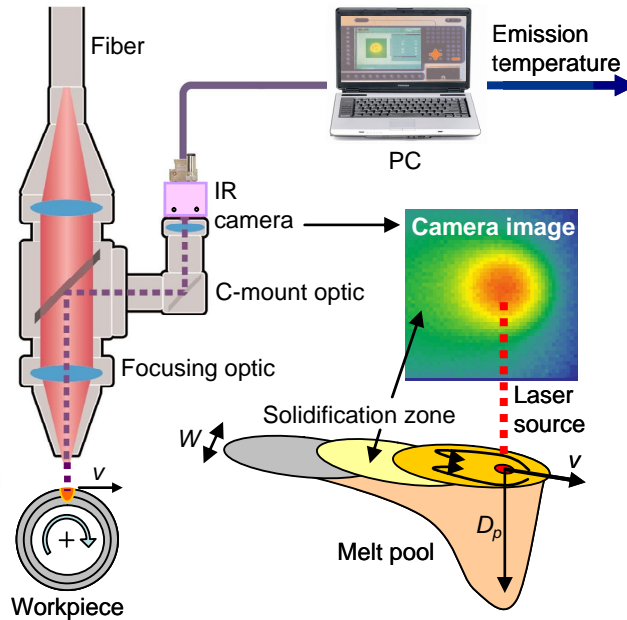


Fig. 7.3: Temperature measurement technique

The temperature measuring technique used in the production line is shown in Fig. 7.3. An infrared camera was used to monitor radiation emitted from the welded surface and the camera image was then processed using Wien-law based software to analyze the temperature distribution over the surface. From the data obtained from these analyses, maximum temperature is found to be around 2500°C (depending on laser parameters) at the surface, which is well below vaporization temperature of the material. This information confirms the correctness of the equation (2) determining the constant K.
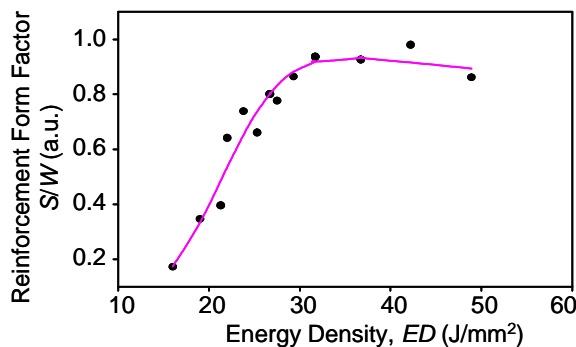


Fig. 7.4: Variation in weld resistance length to weld width ratio with energy density input (R$^2$ = 0.97)

Secondly, to justify the hypotheses taken for the model development, welding tests are performed modulating $P_{in}$ and v. Fig. 7.4 illustrates the change in reinforcement form factor (S/W) with energy density input. From this figure, it is evident that the weld resistance length increases at a faster rate until it becomes almost equal to weld width for a certain energy density input of about 32 J/mm$^2$, though both the weld width and the weld resistance length increase with increasing energy density input. After this limiting value, ratio of weld resistance length to weld width remains the same with further increase in energy density input.
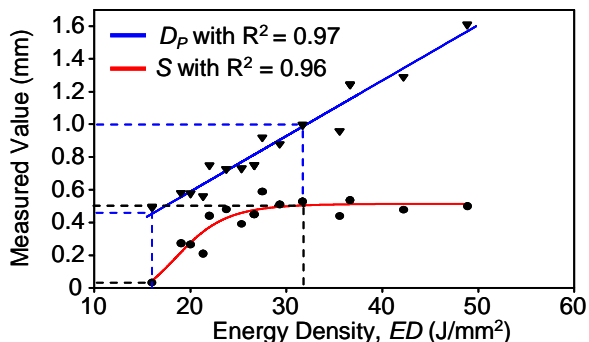


Fig. 7.5: Variation in weld penetration depth and resistance length with energy density input

Fig. 7.5 showing the change in weld penetration depth and weld resistance length depicts that both the weld penetration depth and the weld resistance length vary linearly ($R^2 = 0.97$) and nonlinearly ($R^2 = 0.96$) respectively with the energy density input. This figure also reveals the fact that penetration depth determines the resistance length of the weld in overlap joint configuration. The weld resistance length increases with increasing energy density input until energy input reaches its limiting value of 32 J/mm$^2$. At this limiting value, resistance length becomes almost equal to weld width and is found to be around 0.45 mm, which is close to the spot diameter of the focused beam. These results indicate that laser spot diameter is a good approximation for weld width within the limiting value. Further increase in energy density results in linear increase in weld penetration depth with almost no change in resistance length. Since the weld resistance length is the only characterizing factor that determines the shearing strength, any increase in energy density input after that limiting value would cause only change in weld shape from parabolic to rectangular with almost no contribution to weld mechanical strength. Insufficient weld penetration depth and the resistance length are also evident for the energy density input in the range of 16-20 J/mm$^2$.

Again, Fig. 7.6 shows that penetration size factor (W/D$_P$) changes nonlinearly with energy density input. This is because increase in weld penetration depth with increasing energy density input is higher than that in weld width. Reduction in penetration size factor from 1.0 to 0.6 with increase in energy density input from 22 J/mm$^2$ to 32 J/mm$^2$ is also evident. This result demonstrate the facts that weld profile changes from approximately semicircular to parabolic within the aforestated range of energy density input and the welding is almost conduction limited.
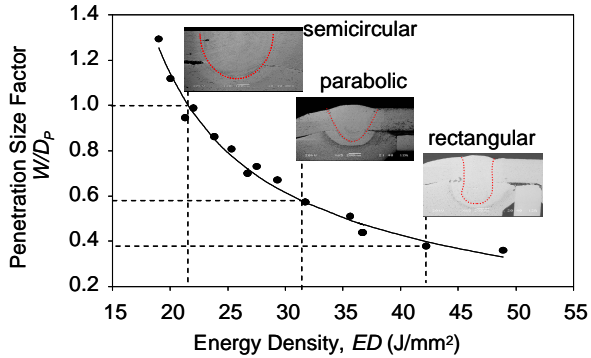
Fig. 7.6: Variation in penetration size factor (W/$D_P$) with energy density input ($R^2$ = 0.97)

Finally, as shown in Fig. 7.7, the predicted and experimental values of the weld penetration depth are plotted for a wide range of energy density input to validate the model. From this figure, it is found that percentage of error in prediction is in an acceptable limit (5%) for the energy density input up to the limiting value of 32 J/mm$^2$. This is because the losses of energy are less for lower energy density input as is shown in [13]. This result also indicates that the developed model is able to predict the weld penetration depth reasonably within this limiting value. However, for a higher energy density input beyond 35 J/mm$^2$, the variations in predicted and experimental results are observed to be higher (around 10%). This is due to the fact that such a high energy density input results in the formation of upper plasma plume, which additionally absorbs a fraction of energy of the laser hindering the beam to transfer the whole $P_{in}$ and hence, to penetrate deeper into the inner shell.
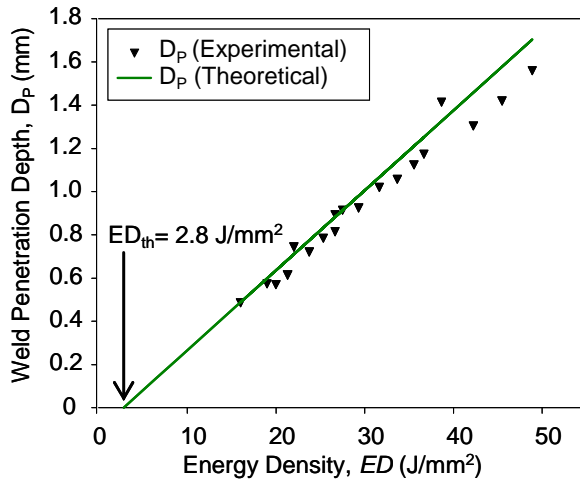


Fig. 7.7: Variation in predicted and experimental weld penetration depth with energy density input

## 7.5. CONCLUSIONS

An easy-to-use model, based on energy density and aimed at predicting the weld penetration and its dependence on laser parameters, is developed and verified by means of experiments. Tests demonstrate that penetration depth determines the weld resistance length in overlap joint configuration within the hypothesis of conduction-limited welding.

Furthermore, experimental results show that weld profile changes from approximately semicircular to parabolic when the energy density input is varied ranging from 22 J/mm$^2$ to 32 J/mm$^2$ and indicate that welding is conduction-limited. At the limiting value of 32 J/mm$^2$, weld resistance becomes almost equal to weld width and is found to be around 0.45 mm, which is close to the spot diameter of the focused beam. Besides, within the aforesaid range, maximum temperature measured on the surface is around 2500 °C, which is well below the vaporization point. As a matter of fact, these results justify the hypotheses made for the model formulation.

Developed model predicts the weld penetration depth accurately (with 5% prediction error) for conduction-limited laser welding. Though error in prediction increases, developed model is also able to reasonably predict the penetration depth (with a prediction error of 10%) beyond conduction limit. However, it also indicates that different heat transfer phenomena and thermal losses restrict the use of this model.

Finally, this energy based model needs only the accurate thermophysical property data for reliable predictions. This model will be able to predict reasonably the penetration depth of weld made of ferritic stainless steels in a wider range provided that (i) reliable values for thermo-physical properties of the intended stainless steels are given (ii) welding is conduction limited (iii) welds are in overlap joint configurations.

## REFERENCES

[1]  Mackwood A.P., Crafer R.C., 2005, Thermal modelling of laser welding and related processes: a literature review, Optics & Laser Technology, 37:99–115.
[2]  Chang W. S., Na S.J., 2002, A study on the prediction of the laser weld shape with varying heat source equations and the thermal distortion of a small structure in micro-joining, Journal of Material Processing Technology, 120:208 – 214.
[3]  Goldak J. A., Chakravarti M. B., 1984, A new finite element model for welding heat source, Metallurgical and Materials Transactions B, 15B:299–305.
[4]  Su W., Haiyan Z., Yu W., Xiaohong Z., 2004, A new heat source model in numerical simulation of high energy beam welding, Transaction China Welding Institute, 25:91–94.
[5]  Kazemi K., Goldak J. A., 2009, Numerical simulation of laser full penetration welding, Computational Materials Science, 44:841–849
[6]  Siva Shanmugam N., Buvanashekaran G., Sankaranarayanasamy K., 2012, Some studies on weld bead geometries for laser spot welding process using finite element analysis, Materials and Design, 34:412–426

[7] Balasubramanian K.R., Siva Shanmugam N., Buvanashekaran G., Sankaranarayanasamy K., 2008, Numerical and experimental investigation of laser beam welding of AISI 304 stainless steel sheet, Advances in Production Engineering and Management, 3(2):93–105

[8] Sabbaghzadeh J., Azizi M., Torkamany M.J., 2008, Numerical and experimental investigation of seam welding with a pulsed laser. Journal of Optics and Laser Technology, 40:289–296

[9] Kruth J.P., Froyen L., Rombouts M., Van Vaerenbergh J., Mercells P., 2003, New Ferro Powder for Selective Laser Sintering of Dense Parts, CIRP Annals - Manufacturing Technology, 52/1: 139–142.

[10] Romoli L., Tantussi G., Dini G., 2007, Layered Laser Vaporization of PMMA Manufacturing 3D Mould Cavities, CIRP Annals -Manufacturing Technology, 56/1: 209-212.

[11] Vollertsen F., Walther R., 2008, Energy balance in laser-based free form heading, CIRP Annals - Manufacturing Technology 57/1: 291–294.

[12] Mills K.C., Su Y., Li Z., Brooks R.F., 2004, Equations for the Calculation of the Thermo-physical Properties of Stainless Steel, ISIJ International, Vol. 44, No. 10, pp. 1661–1668.

[13] Khan M.M.A., Romoli L., Fiaschi M., Sarri F., Dini G., 2010, Experimental investigation on laser beam welding of martensitic stainless steels in a constrained overlap joint configuration, Journal of Materials Processing Technology, Volume 210, Issue 10, pp. 1340-1353.

# CHAPTER 8

## GENERAL CONCLUSIONS AND SCOPE FOR FUTURE WORK

### 8.1 General conclusions

Laser welding of similar martensitic and dissimilar ferritic/austenitic stainless steels have been studied and analyzed. Based on these experimental results and discussions, some general conclusions can be drawn as follows:

#### ⬥ Weld bead characteristics

- Laser welding is a very successful process for joining the similar and dissimilar stainless steels.
- Laser power and welding speed are the most significant laser welding input factors and have opposite effects.
- Focused beam accommodates lower laser power and faster welding speed to obtain a weld with the same geometrical and mechanical features.
- Weld penetration depth and shearing force vary linearly with the energy input and weld resistance length respectively.
- For welding similar stainless steels in overlap joint configuration,
  - ✓ Weld penetration depth determines the weld resistance length and with it, the resisting force to shear across the weld.
  - ✓ Both the weld resistance length and the shearing force are energy-limited.
  - ✓ After the limiting value, additional energy input contributes to the loss of energy and causes problems associated with the excessive energy input.
- For welding dissimilar stainless steels in fillet joint configuration,
  - ✓ Beam incident angle determines the melting ratio of the base metals in the weld volume, which in turn control the thermal properties of the weld and affects the weld bead characteristics significantly.
  - ✓ Formation of keyhole results in rapid change in the weld geometrical and mechanical features within a certain range of energy input.
  - ✓ After the limiting value, upper keyhole plasma plume forms and acts as a point source on the weld plane causing only a 'chaliced shaped' weld bead.

#### ⬥ Weld microstructure and microhardness

- Chemical composition of the base metals and cooling rate control the solidification behaviour and the subsequent solid phase transformation.
- For laser overlap welded martensitic stainless steels,
  - ✓ Solidification microstructures consist of a heterogeneous mixture of martensite and delta ferrite in fusion zone.
  - ✓ Size of the dendrite structure and distribution pattern of the ferrite- and austenite-promoting elements in the fusion zone show a good

agreement with energy input and the associated change in microhardness.
- For laser fillet welded ferritic/austenitic stainless steels,
  - ✓ Various, complex ferrite-austenite microstructures form in the fusion zone.
  - ✓ Carbide precipitates form either intra- or inter-granularly with site based on cooling rate.
  - ✓ Variation in microhardness depends on fraction intermix of each base metal and correlates with the distribution pattern of the segregated alloying elements.

### Laser welding process optimization

- By means of Design of Experiment inspired by full factorial design and response surface methodology, it is possible to achieve the best operating parameter window.
- The models developed can adequately predict the response factors within the design space and can be used to control the welding parameters.
- The graphical optimization techniques are extremely practical for quick technical use in industries to choose the optimal settings of welding

### Energy-based model development

- The model developed is able to replace the cost-consuming monitoring activities currently practised in production line to ensure the required penetration depth.
- This model correlates the heat transfer phenomena with energy density input.
- This model can predict accurately the penetration depth of the weld made of ferritic stainless steels in a wider range provided that
  - ✓ reliable values for thermo-physical properties of the intended stainless steels are given
  - ✓ welding is conduction-limited, and
  - ✓ welds are in overlap joint configurations.

### 8.2 Scope for future work

- These studies could be extended to include more mechanical properties especially the fatigue strength to check the fracture behaviour under dynamic loading condition.
- The microstructure evolution in the fusion zone of the dissimilar stainless steels calls for further research paying a particular attention to the formation of microstructure, distribution pattern of the segregated elements, and change in microhardness with the variation in energy input, beam incident angle and focal position.
- Similar studies could be conducted for more different similar and dissimilar stainless steels which are important for many economic and industrial applications.
- Extensive research could be carried out towards the development of a low-cost real-time monitoring system to detect various defects associated with laser welding of similar and dissimilar jointed stainless steels.